Quantitative Assessment of Tropical Cylcone Simulation Sensitivity in the Community Atmosphere Model

by

Fei He

A dissertation submitted in partial fulfillment
of the requirements for the degree of
Doctor of Philosophy
(Atmospheric, Oceanic and Space Sciences)
in the University of Michigan
2016

Doctoral Committee:

Associate Professor Derek J. Posselt, Chair
Associate Professor Christiane Jablonowski
Professor Vijay Nair
Professor Richard B. Rood

© Fei He 2016

ACKNOWLEDGEMENTS

First of all, I would like to thank my thesis advisor and committee chair, Derek J. Posselt, for his superb mentorship. He has offered help to me since I first arrived at University of Michigan. In 2012, He recruited me as his Phd graduate student and offered me a research assistant (RA) postion at the time when I really needed one. This offer gave me a critical opportunity to grow into an independent researcher. During the RA experience, I have plenty of flexibility to explore my own research ideas. Meanwhile, he is always there for discussion and feedback on research topics, directions, methodology, results, and manuscripts. He also offers assistance in resolving technique problems. He has been very generous to send me to scientific conferences, workshops, and summer schools. He also actively introduced me to scientists from other universities and national laboratories and helped me to establish cooperation with them. He is an extremely responsible and supportive PhD advisor. The four years study and research experience under his mentorship will be profoundly important for my whole career life. I look forward to further collaboration with him and members of his group in my future career path. I also would like to thank the rest of my committee: Christiane Jablonowski, Richard Rood and Vijay Nair. Their advice and support greatly improve the quality of this thesis.

Special thanks to Colin M. Zarzycki and Naveen N. Narisetty. Colin set up the Reed-Jablonowski tropical cyclone (TC) test case in Flux, the high performance computing platform at University of Michigan. He also provided tremendous help for me to learn the RJ TC test case, the NCAR Community Atmosphere Model, the existing studies on tropical cyclones and do preliminary analysis of model simulation data. His help saved tons of time in the beginning stage and allowed me to quickly get into the work. Naveen set up the R code of Expanded Multivariate Adaptive Regression Splines (EMARS) emulator. He also spent a lot of time in explaining the statistical concepts and results. In addition, I would like to thank Kevin A. Reed for providing the TC test case code and detailed explanation on the test case. I also thank Zach Zhanyang

Zhang, Andrew Gentleman, Julio T. Bacmeister, M. Zhao, Sangsu Park, Verronica Berrocal and Erika Roesler for their advice and help.

Thank you Sandra Pytlinski, Margaret Reid, Tonya Thomas, Kristi Hanse, Faye Ogasawara, Bryan K. White and Darren B. Bozzone for your superb administrative and IT support. I also would like to thank Brock Palen and all other Advanced Research Computing staff for their great support. I also would like to thank my group members: David Wright, Greg Tierney, Juan Crespo, Annareli Morales and Sam Tushaus. At last, I would like to thank my parents Longlong He and Fudi Zeng, my husband John Xun Yang and all other family members for their never-ending love and support.

PREFACE

This thesis documented the research work conducted while the author was a member of Dr. Derek J. Posselt's research group. Chapter II was published in *Monthly Weather Review* (He et al., 2015). Kevin Reed provided the FORTRAN codes for the original tropical cyclone test case. Colin Zarzycki set up the model run in Flux, the High Performance Computing Platform of College of Engineering at University of Michigan. Chapter III is in preparation for submission to *Monthly Weather Review*. Naveen N. Narisetty provided the R codes for the statistical calculation of EMARS. The first part of Chapter IV was published in *J. Climate* (He and Posselt, 2015). The remaining part of Chapter IV will be submitted to a yet to be determined journal following the acceptance of this thesis.

TABLE OF CONTENTS

LIST OF FIGURES

LIST OF TABLES

LIST OF APPENDICES

Appendix

ABSTRACT

Quantitative Assessment of Tropical Cylcone Simulation Sensitivity in the Community Atmosphere Model

by

Fei He

Chair: Derek J. Posselt

This work conducted nearly two thousand idealized AGCM simulations to systematically assess the sensitivities of simulated Tropical cyclone (TC) characteristics to changes in model input and evaluate the performance of three surrogate models for approximating the behavior of numerical models. The TC characteristics are intensity, precipitation rate, longwave cloud radiative forcing (LWCF), shortwave cloud radiative forcing (SWCF), cloud liquid water path (LWP) and ice water path (IWP). The National Center for Atmospheric Research (NCAR)/Department of Energy (DOE) Community Atmosphere Model (CAM) version 5.1.1 is adopted. First, the Reed-Jablonowski TC test case was upgraded to a version with background vertical wind shear, in which the well-known shear-induced intensity change and structural asymmetry in tropical cyclones are well captured. Then, a statistical framework, consisting of a combination of Latin Hypercube Sampling (LHS) and surrogate models, is used to investigate the sensitivities of the six simulated TC characteristics to five model initial conditions: initial size and intensity of vortex seed, sea surface temperature, vertical lapse rate and mid-level relative humidity. The surrogate models are shown to successfully reproduce the response of CAM to changes in input conditions, and serve as powerful tools for quantifying numerous model input-output relationships with reduced computational burden. Finally, we examined the impact of parameterized physical processes on TC simulation and quantified the relative importance of 24

physical parameters on the six TC characteristics, respectively. The response function between TC characteristics and the associated most sensitive parameters are characterized. A group of ensemble simulations showed that the interactive effect among physical parameters greatly enlarges the uncertainty of simulated TC precipitation, LWCF, SWCF and IWP. Parameter uncertainty in simulated TC intensity is comparable to uncertainty resulting from changes in model initial conditions and model resolution. The Gaussian Spatial Process Model (GaSP) produced robust fits to CAM model responses in TC intensity, LWCF and SWCF, but experienced some difficulty reproducing TC precipitation rate, LWP and IWP.

CHAPTER 1

Introduction

1.1. Tropical Cyclones

1.1.1. The Importance of Tropical Cyclones

Tropical cyclones, also commonly known as hurricanes (Western Hemisphere) or typhoons (West Pacific), are intense atmospheric vortices that develop over a warm ocean surface with SST generally greater than 26.5 $^{\circ}C$, though it should be noted that Mctaggart-Cowan et al. (2013, 2015) found that the presence of a baroclinic precursor can alter the SST threshold to as low as 24.3 $^{\circ}C$. Tropical cyclones draw energy from the underlying warm water, and transfer and accumulate it to gigantic kinetic energy during their growth. This energy can make them become destructive if landfall was made. A single storm in Bangladesh in 1970 killed nearly half a million people (Emanuel 2003). During the 2004 and 2005 hurricane seasons, United States sufferred a financial loss of over $150 billion (Pielke et al. 2008). About 90 tropical cyclones (TCs) develop each year around the globe (Zhao et al. 2012), and it is currently estimated that this number of TCs causes worldwide annual damage of 19,000 fatalities and $26 billion (Mendelsohn et al., 2012). TCs are one of the most lethal, destructive and expensive natural disasters.

Tropical cyclones also bear profound scientific interest. A tropical cyclone is composed of various interesting processes including: vortical hot towers, individual convective updrafts, cloud microphysics, cloud electrification, precipitation, turbulent mixing, surface momentum transfer, etc. They also play multiple roles in the Earth's climate system. Recent prior studies have suggested that TCs could stabilize the environment in the area along the TC track (Schenkel and Hart 2011) and even across entire ocean basins (Sobel and Camargo 2005). Moreover, TCs have been found to alter the meridional oceanic heat transport (e.g., Emanuel 2001), modulate the atmospheric mid-latitude Rossby wave pattern (Riemer et al. 2008), and greatly reduce the hemispheric zonal available potential energy gradient through the poleward transport of heat and moisture (Cordeira 2010).

1.2.2. The Structure of Tropical Cyclones

A tropical cyclone is a low pressure and rapidly rotating system characterized by strong winds, spiral cloud shields and rain bands (Figure 1.1). At its center is the eye, characterized by descending air that may be cloud free and calm in mature storms. The environment in the eye is warmer than its surroundings during the lifetime of a TC. Thus, tropical cyclones are also referred to as warm core systems. The edge of the eye is called the "eyewall", and is composed of thick and rapidly rotating deep clouds. The eyewall leans outward away from the center of rotation with height, resembling an arena football stadium. Extreme weather conditions occur in the eyewall. Here, the wind speed is greatest, the upward vertical motion of air is largest, clouds reach to their highest altitude, and precipitation is heaviest. The greatest wind damage occurs when the eyewall passes over the land. However, in the developing stage of a tropical cyclone, there may not be a well-defined eye wall, and many TCs do not exhibit a cloud-free eye at any time during their evolution.

Figure 1.1: Hurricane Isabel (2003) as seen from orbit during Expedition 7 of the International Space Station. Credit given to: Mike Trenchard, Earth Sciences & Image Analysis Laboratory, Johnson Space Center

The eye, eyewall, and surrounding rainbands, characteristics of a mature tropical cyclone, are clearly visible in the view from space shown in Figure 1.1. The winds decrease gradually with increasing distance outward from the eyewall, and the outer edge of the eyewall defines the size of a tropical cyclone. Several rain bands circulate around the eyewall, and air rises in those deep clouds with sinking air between the rings of deep clouds. The vertical structure of a tropical cyclone is shown in Figure 1.2.

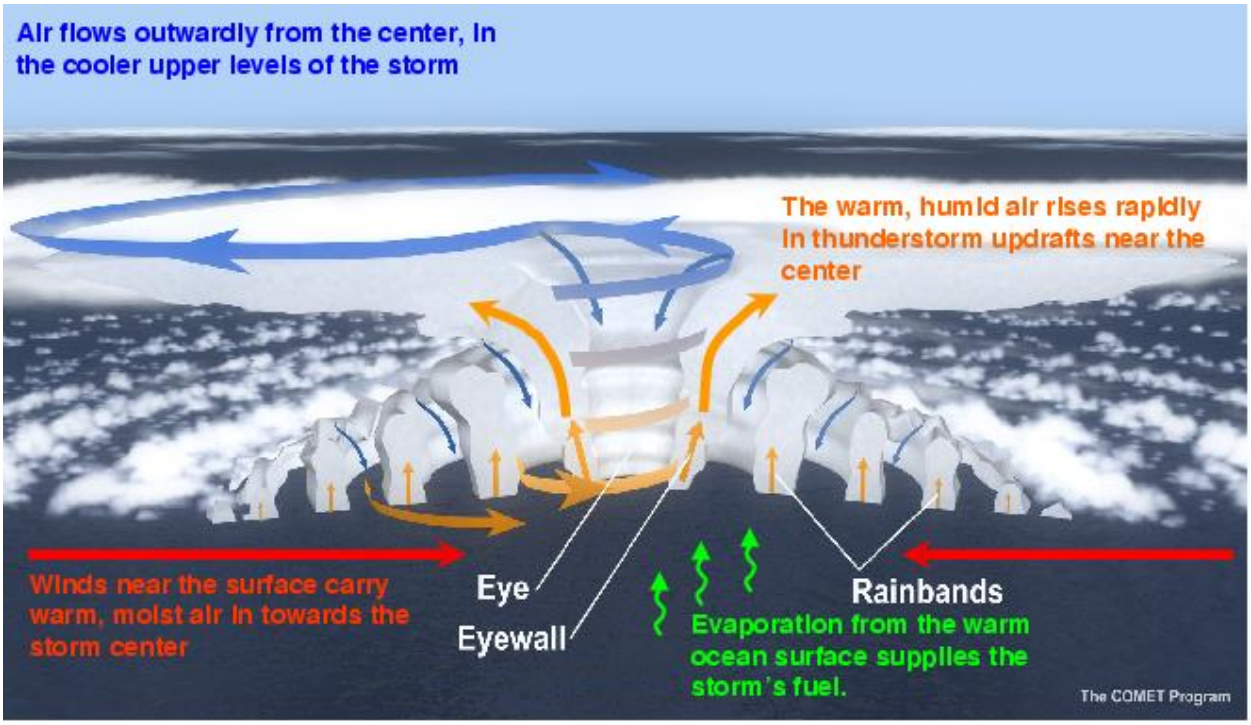

Figure 1.2: Diagram of a northern hemisphere hurricane. Credit given to: the COMET program.

As shown in Figure 1.2, the wind motion can be divided into two parts: primary circulation and a secondary circulation. The primary circulation is the rotational part of the flow. The secondary circulation is the radial-vertical overturning part of the flow. Air rises from the eyewall, spreads outward through the outflow cirrus shield, descends downward and spirals inwards toward the eye near the surface. The primary circulation has the strongest winds and is responsible for the majority of the damage a storm causes, while the secondary circulation is slower but governs the energetics of the storm.

1.2. Numerical Simulations of Tropical Cyclones

Reconnaissance aircraft, meteorological radar and satellites are powerful observation techniques to reveal the essence of a hurricane's structure and inner workings (Emanuel 2003). Mathematical models provide another potential source of information about hurricanes. They can

be effective at filling in details that are difficult to observe. For example, it is very difficult for aircraft to measure the air's vertical motions, upward and downward, in a tropical cyclone. An airplane may be able to sample a few updrafts and downdrafts on its way across a storm, but such measurements are unlikely to reflect the full range of motions in a storm. Computer models have the advantage of being able to simulate enough points to cover the complete vertical movement of air in a tropical cyclone. In addition, numerical models are effective in testing assumptions and hypotheses, conducting short term forecasting, and performing long term future prediction of tropical cyclones.

1.2.1. Limited Area Models (LAMs)

Limited Area Models (LAMs) have been the primary tools used to simulate and forecast TCs over the past half century, because they are able to ultilize small horizontal grid spacings (e.g. 2 km; Gentry and Lackmann 2010) and thus capture very fine structures in TCs such as mesoscale eddies, vortical hot towers, etc. The domain boundaries of LAMs are forced by external sources such as larger domain models, observational data or idealized conditions. One of the most frequently used LAMs is the Weather Research and Forecasting Model (WRF, Skamarock et al. (2008)).

LAMs are often used for short-term, deterministic forecasting such as predicting the intensity of developing tropical cyclones during Atlantic hurricane seasons and investigating the characteristics (e.g. strength, development, track) of individual cyclones. The model is usually initialized with a "bogus" vortex (an idealized balanced circulation; e.g., Kwon and Cheong 2010) and horizontal grid spacing can be as fine as 1-10km. The model results are typically compared to observations to assess realism and skill (Nolan et al. 2009, Wang and Xu 2010, Abarca and

Corbosiero 2011). Idealized simulations are often designed in LAMs to isolate the effect of dynamical features, explore environmental impacts, and test changes in model structure (e.g. physical parameterization, grid resolution and dynamics-physics coupling; Nolan 2007, Nolan et al. 2007, Hill and Lackmann 2009).

Despite these strengths, LAMs have major limitations in simulating TCs due to their inherent model designs. They cannot simulate the impact of large scale variability such as El Nino Southern Oscillation (ENSO) on TC evolution, and cannot represent the two-way interaction between TCs and large scale environmental flows. LAMs are also sensitive to several issues, such as the domain size, location of lateral boundaries, waves reflected from boundaries, etc, all of which will induce additional errors in TC simulation and forecasting. These are not issues with global climate models.

1.2.2. Atmospheric General Circulation Models (AGCMs)

Manabe et al. (1970) was the first to identify a tropical cyclone-like disturbance in an AGCM with model resolution of 417 km. Their simulated TCs were much larger and weaker than observed. Following that work, several more studies (Broccoli and Manabe 1990; Haarsma et al. 1992; Bengtsson et al. 1995) simulated more realistic storm structure with higher resolution AGCMs. Nevertheless, the model resolution was still coarse and the use of AGCMs for TC simulation was questioned by Henderson-Sellers et al. (1998).

As the model resolution become 100 km or higher, AGCMs showed improved representation of tropical cyclone activity in frequency and distribution (Kobayashi and Sugi 2004; Bengtsson et al. 2007a). LaRow et al. (2008) and Zhao et al. (2009) were also able to capture observed interannual variability with correlations of 0.78 and over 0.8, respectively for

North Atlantic hurricanes. Several recent studies suggest that AGCMs with resolutions in the range of 20-100 km are adequate for studying many aspects of tropical cyclone (TC) genesis and frequency distributions (e.g., Bengtsson et al. 2007a,b; Oouchi et al. 2006; LaRow et al. 2008; Zhao et al. 2009; Vitart 2006; Gualdi et al. 2008). The current suite AGCMs are able to achieve fine resolution of 20-km (Oouchi et al. 2006) or even 10 km (Manganello et al. 2012). Some AGCMs even run these fine resolutions for multidecade simulations. Two examples are the Meteorological Research Institute-Japan Meteorological Agency (JMA) GCM (Murakami and Wang 2010), and the European Centre for Medium Range Weather Forecasts (ECMWF) Integrated Forecasting System (IFS) model (Manganello et al. 2012).

In general, using AGCMs to simulate tropical cyclones has for some time been limited by horizontal and vertical resolution and computational demand. Improvements of computer architectures and high-resolution AGCMs over the past decade have eased the restrictions on model resolution. The recent advancement in computational resources and parallel computing has stimulated new interest in simulating TCs in AGCMs, which are now capable of being run with as fine as 12.5 km grid resolution. The increasing interest in TCs global distribution, climatological evolution, and future changes under climate warming scenarios further ensures that simulating TCs with AGCMs is inevitable. While global models are commonly used for TC prediction, there is also a recent growing trend that AGCMs are being tested for short term forecasting and compared with weather prediction models. For example, Zarzycki and Jablonowski (2015) successfully forecast the recurvature of Hurricane Sandy. Xiang et al. (2015) also studied the prediction of Hurricane Sandy and Super Typhoon Haiyan in the Geophysical Fluid Dynamics Laboratory (GFDL) coupled model. As numerical algorithms and computational

resources advance, and considering the advantage of allowing two-way interaction in global climate models, this trend may grow quickly in the next few decades.

1.3. The Current State of Simulating and Predicting Tropical Cyclones in AGCMs

1.3.1. Detecting Tropical Cyclones in AGCMs

An essential first step in any analysis of tropical cyclones in AGCMs is to detect and track the storms in the model output. Considering the complexity of model output and the small size of tropical cyclones relative to the Earth, it is a challenging task and may result in extra uncertainty in tropical cyclone studies using AGCMs. Figure 1.3 shows a simulation of hurricane Katrina (2005) in a global model output from the GFDL global climate model. The hurricane is small in size relative to the global scale circulation, and its detection could easily be affected by the presence of other deep convective systems in the global model. A number of schemes for TC detection have been developed over the years. They share many common characteristics but also have some important differences. They were summarized into five categories in Walsh et al. (2015): (1) structure-based threshold schemes (Walsh et al. 2007); (2) variable threshold schemes (Murakami et al. 2011); (3) schemes in which model output is first interpolated onto a common grid before tracking (Hodges 1995; Bengtsson et al. 2007a; Strachan et al. 2013); (4) model-threshold-dependent schemes (Camargo and Zebiak 2002); and (5) circulation-based schemes (Tory et al. 2013). It is clear that simulated tropical cyclone results should not be dependent on the tracking schemes; however, some studies show dependence (Camargo 2013; Tory et al. 2013b; Murakami et al. 2014). Tracking TCs can become additional source of uncertainty in full model runs.

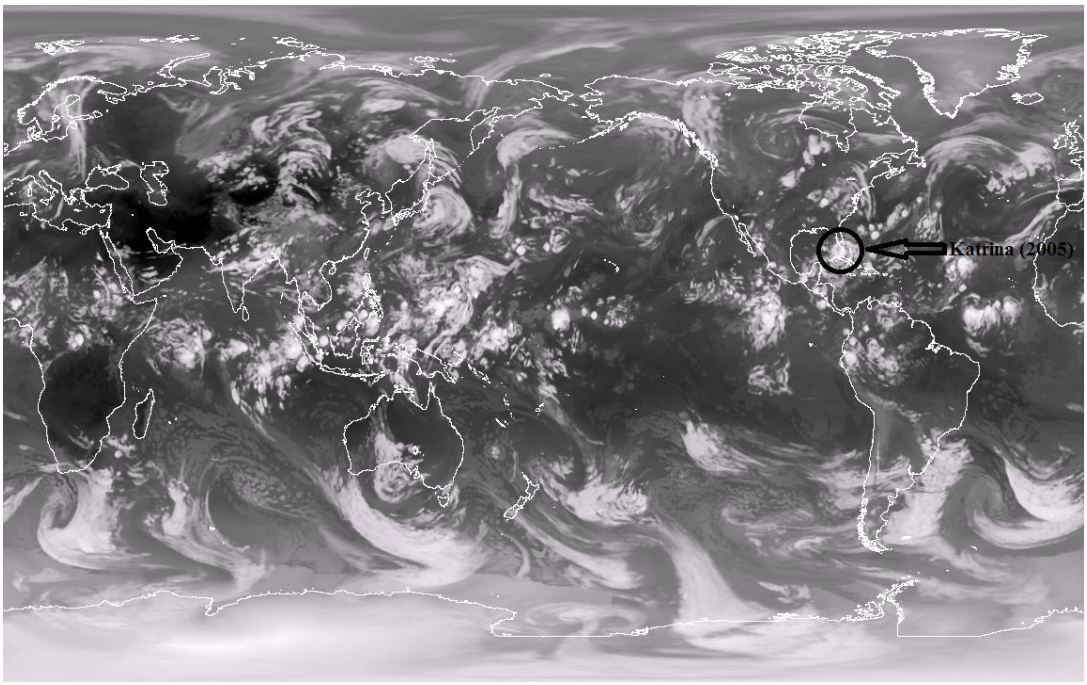

Figure 1.3: Outgoing Longwave Radiation (OLR). Hurricane Katrina (2005) simulated in Geophysical Fluid Dynamics Laboratory global atmospheric cubed-sphere (C360) with 25 km resolution.

1.3.2. Modeling Tropical Cyclones in Present Climate State

Nowadays, AGCMs have been widely used for studies of tropical cyclones. They are used for the tropical cyclone statistics of genesis, track, intensity, frequency, and precipitation in either global or basin wide spatial scale. They are also used for 1-5 day operational hurricane forecasting, seasonal to decadal hurricane prediction, multi-decadal climate variability, and examining changes to hurricanes under climate change. A starting point is the ability of climate models to simulate the climatology of TCs in current-climate simulations. Studies show that the simulated global TC numbers range from small values to numbers similar to those observed (Shaevitz et al. 2014). Better results can be obtained from higher-resolution versions CAM5 (finer than 50-km horizontal resolution as shown by Wehner et al. 2014). Their simulation was capable of generating intense tropical cyclones. The annual cycle of formation is reasonably well

simulated in many regions, although there is a tendency for the amplitude of the simulated annual cycle to be less than observed. The performance at simulating Atlantic tropical cyclone formation is poorer than for other basins. Studies show that use of higher resolution AGCMs could improve the performance (Mei et al. 2014). Strachan et al. (2013) found that the observed interhemispheric asymmetry in tropical cyclone formation between Northern Hemisphere and Southern Hemisphere was not well captured by a high resolution AGCM. The fact that increasing resolution solves some problems, while not addressing others, indicates increasing resolution alone is not sufficient to produce a realistic cyclone climatology.

1.3.3. Future Changes of Tropical Cyclones Under Climate Warming and Their Uncertainty

One important contribution of AGCMs is that they could be used to predict future changes of tropical cyclones under various climate change scenarios. There are substantial studies on this topic. Oouchi et al. (2006) found that tropical cyclone frequency in a warmer climate experiment was globally reduced by about 30%. Bengtsson et al. (2007b) found considerable reduction in the number of TCs by approximately 20% in the 21st century, while the number of storms with maximum wind speeds greater than 50 $m \cdot s^{-1}$ increased by a third. Bender (2010) found that the frequency of intense storms (category 4 and 5) may double by the end of the 21st century; however, the overall frequency of tropical cyclones may decrease. Other phenomena associated with hurricanes are also found to change in response to climate change. For example, Chauvin et al. (2006) found that mean hurricane dynamical characteristics are slightly changed by the warming but precipitation core and latent heat flux are enhanced.

Projections of the potential impacts of global warming on regional tropical cyclone (TC) activity vary considerably, especially at the ocean-basin scale. Quantifying its possible range is important for estimations of potential future social and economic loss. Studies found a number of factors that could lead to such inconsistencies: (1) assumed spatial patterns of future changes in sea surface temperature (SST; Sugi et al. 2009; Zhao et al. 2009); (2) model physical parameterizations (Walsh et al. 2010); (3) the chosen global warming scenario (Stowasser et al. 2007); and (4) the methods used to detect TCs (Walsh et al. 2007). Some studies have addressed uncertainties due to variations in assumed future changes in SST (Emanuel 2008; Sugi et al. 2009; Zhao et al. 2009), some other studies have addressed the uncertainties that arise from differences in model physics (e.g., Yokoi et al. 2009; Yokoi and Takayabu 2009; Walsh et al. 2010). Murakami et al. (2012) conducted multi-physics and multi-SST ensemble experiments using the 60-km-mesh MRI-AGCM to assess the uncertainties of the future changes in tropical cyclone activity and found that all ensemble experiments consistently project significant reductions in global and hemispheric TC genesis numbers.

1.4. Progress in Improving the Performance of AGCMs to Simulate Tropical Cyclones

While much progress has been made over the last two decades in the modeling of tropical cyclones in AGCMs, there are still large deficiencies. Numerous efforts have taken various pathways to improve the representation of tropical cyclones in AGCMs. The efforts can be summarized in two categories: one is to improve the computing architecture and numerical algorithms, and the other is to design test cases for better model evaluation. The former includes the application of parallel computing, supercomputers, high-resolution, variable resolution, non-hydrostatic dynamical cores, scalable quasi-uniform meshes, and scale-aware physical parameterizations. The latter includes building simpler and more idealized tropical cyclones for

model testing to better understand the impact of model construction on tropical cyclone simulations and thus to instruct the analysis of full GCMs.

1.4.1. Numerical Enhancement

As the method that holds perhaps the most promise for future simulation of tropical cyclones in AGCMs, the majority of efforts to improve TC representation have been placed on improving the computing architecture and numerical algorithms. In this paradigm, parallel computing and supercomputers are implemented so as to run AGCMs with fine resolution. As model resolution refines to 10 km or finer, AGCMs need to utilize the non-hydrostatic equations, as the hydrostatic approximation is no longer valid. Non-hydrostatic dynamical cores have been developed (Simarro et al. 2013; Ullrich and Jablonowski 2012) for AGCMs to better represent tropical cyclone processes. Scalable quasi-uniform meshes that replace the typical latitude-longitude mesh based on icosahedral (Williamson, 1968) or cubed-sphere grids (Sadourny 1972) represent another solution that enables very fine resolution in AGCMs. These methods were originally designed to eliminate the computational inefficiency due to small physical grid spacing in the pole regions. The Non-hydrostatic Icosahedral Atmospheric Model (NICAM) model that utilizes a geodesic mesh has shown the ability to simulate tropical cyclones (Tomita and Satoh 2004). The GFDL finite-volume cubed-sphere model (Putman and Lin 2007, 2009) has been used to conduct tropical cyclone climate change experiments (Zhao et al., 2009). In addition to advances in computational resources, non-hydrostatic dynamical cores and quasi-uniform meshes, progress has also been made in the area of mesh refinement within AGCMs. Mesh refinement techniques allow for finer resolution in limited area of the global domain and offer an attractive approach to simulating tropical cyclones in AGCMs. They allow for implementation of very fine resolution in active hurricane regions and at the mean time reduce

the computational burden, as other areas are covered with coarse resolution. This enables to the simulation of fine scale structures of hurricanes in AGCMs. The mesh refinement could be either static or adaptive. Recently, mesh refinement techniques have shown great success in simulating and forecasting tropical cyclones (Zarzycki et al. 2014a,b; Zarzycki and Jablonowski 2014, 2015). As the model resolution and dynamical cores advance in AGCMs to better represent tropical cyclones, development of scale-aware physical parameterization is another important direction, as many key processes in tropical cyclones reply on physical parameterization. The development of scale-aware parameterizations is a new and developing research field, and only a small amount of work has been performed (Chen et al., 2011).

1.4.2. Idealized Tropical Cyclone Simulation for Model Evaluation

While computing architecture and numerical algorithms are advancing, another necessary research part is to ensure the model construction can represent tropical cyclones in a manner that is consistent with fundamental scientific understanding. Reed and Jablonowski have designed a tropical cyclone test case and evaluated the physical and dynamical components of CAM to assess their reliability for tropical cyclone studies during a series of experiments (Reed and Jablonowski 2011a, b, c; 2012). They first developed an idealized tropical cyclone test case for high-resolution GCMs and implemented it in aqua-planet mode with constant sea surface temperatures (Reed and Jablonowski 2011a). Their initial conditions are based on an analytic initial vortex seed in gradient-wind and hydrostatic balance, which intensifies over a 10-day period. Second, they assessed the influence of changes in the model parameterization package on the development of the tropical cyclones (Reed and Jablonowski 2011b). They found that the choice of the CAM physics suite has a significant impact on the evolution of the idealized vortex into a tropical cyclone. Third, they also explored the impact of initial-data, parameter and

structural model uncertainty on the simulation of a tropical cyclone like vortex in the CAM (Reed and Jablonowski 2011c). In addition, a test case of intermediate complexity was introduced. The impact of the four CAM dynamical cores (the resolved fluid flow component) on the tropical cyclone intensity and size was evaluated (Reed and Jablonowski 2012). Reed and Jablonowski (2011a, 2011b, 2011c and 2012) have successfully used this test case to reveal the impact of grid resolution, dynamical cores and physical parameterization packages on the development of tropical cyclones. Building on this foundation, we extend the evaluation to a more systematic assessment using uncertainty quantification techniques.

1.5. Uncertainty Quantification and Sensitivity Analysis

The uncertainty quantification (UQ) framework has come to refer to a set of techniques now widely used to examine uncertainties in numerical models associated with initial conditions, model physics parameters, and construction (Stensrud et al. 2000; Murphy et al., 2004; van den Heever and Cotton 2004; Posselt and Vukicevic 2010; Collins et al., 2011; Berner et al. 2011; Posselt and Bishop 2012; Posselt 2016; Posselt et al. 2016). Calculations with numerical models are often referred to as numerical experiments, by analogy to classical laboratory experiments. Usually, many numerical experiments are carried out to determine the response of a numerical model to variations of internal or external parameters over some range of interest. If individual experiments are computationally inexpensive, and if the number of independent parameters is small, it may be possible to search the entire parameter space of the model. This is difficult, however, if the dimension of parameters space is even moderately large or the codes are expensive to run. Numerous methods are developed for the design and analysis of numerical experiments that are especially useful and efficient in multidimensional parameter spaces. This

includes space filling design methods (e.g. Latin Hypercube Sampling method) and surrogate models, which fit a statistical model to the output of the numerical model.

1.5.1. Latin Hypercube Sampling and Other Techniques for Uncertainty and Sensitivity Analysis

The assessment and presentation of the effects of uncertainty are now widely recognized as important parts of analyses for complex systems. The Latin Hypercube Sampling (LHS) method is a component in the UQ process that generates a space-filling ensemble of samples (McKay, et al. 1979; Iman and Shortencarier 1984; and Helton and Davis 2000). The use of LHS constitutes part of what is often called a Monte Carlo procedure for the propagation of uncertainty. It seeks to accurately extract as much trend data from a parameter space as possible using a limited number of sample points. While the input parameter range is divided into equi-probable non-overlapping intervals, LHS requires that every row and column in the hypercube of partitions has exactly one sample, which ensures full coverage of the range of the input variables.

In addition to LHS, there exist a number of other procedures that are also used for the propagation of uncertainty, including differential analysis, response surface methodology (RSM), the Fourier amplitude sensitivity test (FAST) and the closely related Sobol's variance decomposition, and fast probability integration (FPI). All techniques have positive and negative features, and no single technique is optimum for all situations. Monte Carlo techniques (Ma and Ackerman 1993; Ma et al. 1993; Gwo et al. 1996) are based on the use of a probabilistic procedure to select model input and result in a mapping between analysis inputs and outcome. The major drawback is computational cost. This is especially the case if long-running models are under consideration or probabilities very close to zero or one must be estimated. Differential

analysis (Eberhard and Bischof 1999; Griewank 2000) is based on developing a Taylor series approximation to the model under consideration. But it is inherently local and can be difficult to implement sometimes and require large amounts of human or computational time. Response surface methodology (RSM) (Draper and Pukeisheim 1996) is based on using an experimental design to select model input and then developing a response surface replacement for the original model. The FAST approach (Cukier et al. 1973; 1978) and Sobol' variance decomposition (Sobol' IM 1993) are based on a direct decomposition of variance into the parts contributed by individual variables. Fast probability integration (FPI) (Wu Y-T. 1987; Haskin et al. 1996) is based on the use of analytic procedures to evaluate distribution functions.

1.5.2. Multiple Predictor Smoothing Methods for Sensitivity Analysis

Latin hypercube sampling is widely used in Monte Carlo (i.e., sampling-based) approaches, analyses of this type, especially when computationally intensive models are involved. Meanwhile, sensitivity analysis also requires the use of regression-based techniques that are based on multiple predictor smoothing methods. Detailed descriptions of these techniques can be found in Storlie and Helton (2008). These techniques include the traditional parametric regression model, nonparametric approaches based on local data smoothing, and stepwise implementation for regression.

Parametric regression models establish a continuous mathematical function between predictor $\vec{x}$ ($\vec{x} = (x_1, x_2, ..., x_n)$) and targeted variables $\vec{y}$. The basic mathematical functions that form such regression models can be linear, logarithmic, square root, quadratic, and nonlinear. For example, $y = \beta_0 + \beta_1 x + \beta_2 \exp(\beta_3 x) + \varepsilon$, where the relationships between y and the only predictor x are nonlinear. Once the candidate form for the parametric regression model has been

determined, the β_j' s can be estimated with techniques based on least squares, which is the maximum likelihood estimate when the ε' s are normally distributed.

Nonparametric regression can be more effective at representing nonlinear relationships. It is often called smoothing and is a form of surface approximation that is based on assumed relationships of the form $y = f(\vec{x}) + \varepsilon, \vec{x} = [x_1, x_2, ...]$, where $E(\varepsilon) = 0$. Usually, very few restrictions or assumptions are made about the properties of f . In particular, f is not assumed to take a particular parametric form, such as a multivariate polynomial function. Sometimes f is assumed to be "smooth" in the sense that certain continuity restrictions are imposed on f and possibly its derivatives. Running means, locally weighted means (kernel smoothers), locally weighted regression, smoothing splines, generalized additive models, and recursive partitioning regression are typical methods to build the nonparametric regression models. Sometimes, the nonparametric regression models are built in a stepwise way instead of continuously.

These different techniques lead to different statistical surrogate models such as Gaussian spatial process model (GaSP; Sacks et al., 1989; Craig et al., 2001), Multivariate Adaptive Regression Splines (MARS; Friedman et al., 1995), Multiple Additive Regression Trees (MART; Friedman, 1999; Friedman and Meulman, 2003) and so on.

1.6. Thesis Overview

The goal of this thesis is to systematically assess the sensitivity of simulated tropical cyclone characteristics to varying model configurations in the NCAR/DOE Community Atmosphere Model using UQ techniques. UQ techniques have been widely applied to the CAM model to optimize global climate sensitivity (Covey et al. 2013), reduce model error and improve

climate prediction (Jackson et al. 2008), improve the influence of convection on the global circulation (Yang et al. 2013), and examine other global features of CAM like radiation flux at the top of the atmosphere. Our study uses UQ to assess the performance of CAM for simulations of an individual/local dynamical system: a tropical cyclone. We start with the Reed-Jablonowski tropical cyclone test case, a specially designed idealized simulation, to overcome the challenge brought by the extremely complicated architecture of an AGCM, which makes identifying the causes of sensitivity difficult and computationally intractable. The idealized simulation only contains one single tropical cyclone in its initial condition, and we refer it as a TC test case. It mimics the process of developing a preexisting vortex seed into a storm-like vortex in an AGCM over 10 days by retaining the complete construction of the AGCM. It can efficiently reflect the impact of model construction and quickly identify the causes of TC variation.

After the modeling tool is chosen, the second challenge lies in designing a statistical framework. Grid searching methods account for all possible combinations of the parameters in full space, but are extremely computationally expensive. 10 parameters require a minimum of 2^{10} simulations. Our single simulation at horizontal resolution of 25 km takes 24 hours to complete using 50 CPUs. To tackle these constraints, we proposed a framework that consists of a combination of Latin Hypercube Sampling (LHS) and a statistical surrogate model. GaSP, MARS and EMARS are evaluated. LHS has been shown to simulate uncertainty as accurately as a Monte Carlo sampling method while using far fewer samples. EMARS improves on conventional emulators by allowing quadratic or higher order components in the model building process, which in turn allows for higher accuracy.

In summary, a robust uncertainty quantification framework applied a set of specially designed idealized simulations enables us to systematically assess the sensitivities of AGCM-

simulated TCs to various model components, quantify the response functions and explore the nonlinear interactive effects among model components. Sensitivity analysis, in general, refers to measurement of how model output responds to the changes of model input. The goal of sensitivity analysis could be interpreted as figuring out the relationships between model output $y_j (j = 1, 2, 3, ..., m)$ and model input $x_i (i = 1, 2, 3, ..., n)$. The sensitivity analysis for a tropical cyclone in the CAM within our work can be summarized by Figure 1.4.

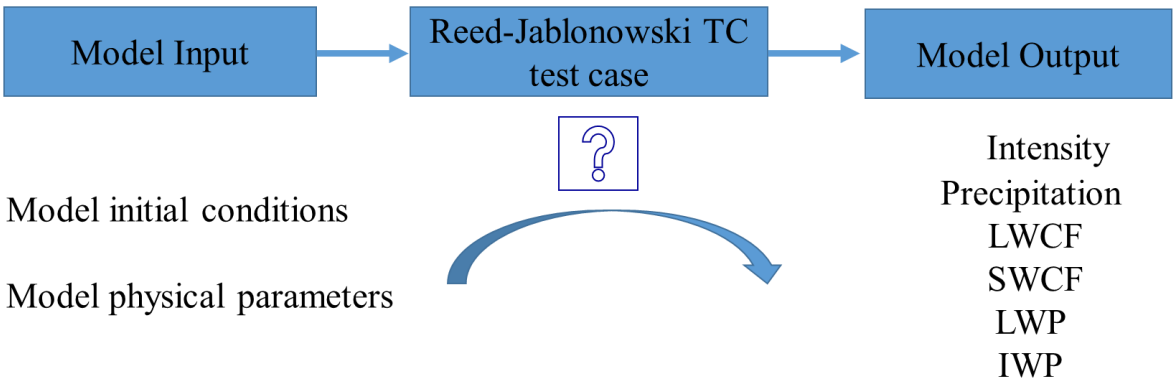

Figure 1.4: Schematic diagram of the sensitivity analysis in this thesis.

We are mainly interested in model output of six TC characteristics: intensity, total (convective + grid scale) precipitation rate (PRECT), longwave cloud radiative forcing (LWCF), shortwave cloud radiative forcing (SWCF), cloud liquid water path (LWP) and cloud ice water path (IWP). In addition to the fact that these six characteristics govern important properties of a TC during its evolution, the last five variables are rarely studied in TC simulations from AGCMs. Moreover, the last five characteristics present a challenge for statistical surrogate models. Surrogate models are designed to approximate the behavior of a numerical model and to replace it in sensitivity analysis to lessen the computational burden of running the full numerical model. They have been shown to have great success in fitting model input-output relationships in many

other fields. However, it is unclear to what extent or complexity level the surrogate models can mimic the performance of numerical models of complex atmospheric systems. The TC precipitation, LWCF, SWCF, LWP and IWP result from very complicated dynamical and physical processes in AGCMs, and as such provide an opportunity to evaluate the performance of surrogate models.

The thesis is organized as follows. Chapter II describes an upgraded version of the Reed-Jablonowski TC test case with environmental vertical wind shear so that the simulation is more realistic and relevant to TC development. Chapter III demonstrates the utility of uncertainty quantification framework in assessing the sensitivity of simulated TC characteristics to multiple parameters. The specific case verifies the ability of AGCMs to capture the essential dynamical mechanisms and sensitivity of tropical cyclones to factors long believed to be important of TC development, such as sea surface temperature, vertical lapse rate, mid-level relative humidity, initial vortex size and strength. The results show that the evolution and development of simulated TCs in CAM can respond to the change in these factors in a way consistent with previous literature. Chapter IV explores the impact of numerous parameterized physical process on simulated tropical cyclones characteristics and quantify the relative importance of 24 physical processes. Chapter V gives the summary of the results and discusses the possible future work. Though Chapter II has developed a version of RJ TC test case with vertical wind shear, we need to note here that the RJ TC test case used in Chapter III and IV are still the original TC test case without vertical wind shear and with full physical parameterization package in CAM.

CHAPTER 2

A Balanced Tropical Cyclone Test Case for AGCMs with Background Vertical Wind Shear

2.1. Introduction

Improving the ability of Atmospheric General Circulation Models (AGCMs) to model various weather systems is crucial as they are increasingly used to understand the current climate state and predict its future change. The use of observations to evaluate AGCM components (e.g., physical parameterizations) and model intercomparisons are important steps in this direction, but are not straightforward due to the inherent complexity of AGCMs. A series of test cases (e.g. Jablonowski and Williamson 2006a; Reed and Jablonowski 2011a, 2012) have been designed for the purpose of testing new model components and configurations in a reduced complexity system. They are analytic in form and based on four principles: deterministic, easy-to-use, relevant to typical atmospheric phenomena, and applicable to a wide variety of model formulations and grids (Jablonowski and Williamson 2006a).

Modeling tropical cyclones in a global climate model is a challenging task. Whether GCMs with current resolutions are appropriate tools to investigate tropical cyclone activity, and to what extent they are capable of simulating aspects of observed TC activity, is still debated even though they have demonstrated a continuously improving skill in generating realistic TC characteristics (Walsh et al. 2015). A horizontal grid spacing of 2 km or less has been suggested

to explicitly resolve the important physical processes within TCs, and hence better represent the storm intensity (Gentry and Lackmann 2010). Rotunno et al. (2009) also show that simulations with grid spacing less than 100 m capture more realistic turbulent eddies consistent with observational results (Bell and Montgomery 2008). Use of 2 km grid spacing or finer is not computationally feasible for current GCMs. Though model development focuses on grid spacing of 0.25 degrees or approximately 28 km (Bacmeister et al., 2014), production runs typically use horizontal grid lengths of 50 km or larger (Stocker et al. 2013). Simulations run at relatively coarse resolution generally underestimate storm intensity (Randall et al. 2007; Strachan et al. 2013) and cannot accurately reproduce the track density (Zarzycki and Jablonowski 2014).

A GCM-based tropical cyclone (TC) test case was designed by Reed and Jablonowski (2011a; hereafter RJ2011), aiming to improve the representation and simulation of TCs in AGCMs. It consists of a single balanced warm-core vortex seed embedded in a quiescent tropical environment on an aqua-planet. After 10 simulated days, the initial vortex seed grows into a mature tropical cyclone-like vortex. By replacing the model initial condition with an idealized setup and retaining the full three dimensional model configuration (e.g. model resolution, physical parameterizations, dynamical core), the analytic TC test case has been demonstrated to successfully reveal the influences of model design on TC structure and evolution (Reed and Jablonowski 2011a, 2011b, 2011c) and aid in understanding differences in simulated TCs among different climate models. For example, Reed and Jablonowski (2011b) found that inclusion of a new dilute entraining plume assumption in Convective Available Potential Energy (CAPE) calculation is responsible for stronger and larger TCs in the Community Atmosphere Model (CAM) version 4 compared to CAM version 3.

Despite these successes, an important limitation of RJ2011's test case is that the initial vortex seed is placed into an environment completely free of background vertical wind shear (VWS). VWS, commonly expressed as the difference of the horizontal wind between 200 hPa and 850 hPa, is known to be a key environmental variable that affects the genesis and intensification of TCs (Gray 1968; DeMaria 1996; Frank and Ritchie 1999, 2001; Riemer et al. 2013; Rogers et al. 2013). It also provides a possible dynamical connection between Atlantic major hurricane activity and remote atmospheric patterns such as the El Niño Southern Oscillation (Goldenberg and Shapiro 1996). Furthermore, Zhang and Tao (2013) showed the vertical wind shear affects the predictability of tropical cyclones, and larger shear magnitude leads to larger uncertainty of prediction. Moreover, very few observed TCs develop in a zero wind shear environment; therefore, incorporating VWS can provide more realistic and relevant TC simulations and enable tests of how the large scale environmental flow affects the development of TC structure in climate models. The goal of this study is to present a technique for adding background vertical wind shear to the TC test case that successfully simulates wind shear effects on TC development.

Vertical Wind Shear and Tropical Cyclones

The effect of VWS on TC genesis and development is dependent on its magnitude and direction. Large wind shear (e.g., 15 $\mathrm{m\,s^{-1}}$) inhibits tropical cyclone genesis (e.g., Goldenberg et al. 2001; Emanuel and Nolan 2004) and is detrimental to the intensification of developed TCs (e.g. Gray 1968, 1975; Zehr 1992; DeMaria et al. 2001; Zehr 2003). Small or moderate shear is believed to either have little impact, or perhaps even be beneficial to TC intensification (Gray 1975; Tuleya and Kurihara 1981; Wong and Chan 2004; Paterson et al. 2005; Nolan and McGauley 2012), although other studies have shown contradictory results (e.g., Zeng et al. 2010; Ge et al. 2013). Westerly shear tends to reduce TC intensity more than easterly shear does for a given shear

magnitude (Tuleya and Kurihara 1981; Bender 1997; Black et al. 2002; Ritchie and Frank 2007, hereafter RF2007; Zeng et al. 2010). RF2007 proposed a beta shear theory to explain this difference. Their study showed that a northwestward beta shear will be induced with variable Coriolis parameter (f), which can either partially offset the environmental easterly shear or reinforce the westerly shear.

The impact of VWS on TC genesis and intensification is commonly explained by the venting theory (Simpson and Riehl 1958; Gray 1968; Jones 1995; Smith et al. 2000; Frank and Ritchie 2001; Schecter et al. 2002; Reasor et al. 2004; Tang and Emanuel 2010). Simpson and Riehl (1958) and Gray (1968) hypothesized that storm development is inhibited by the shear-induced loss of heat and moisture in the upper-level warm core. Frank and Ritchie (2001) showed that ventilation at the upper levels of the eye reduced the storm pressure anomaly in 3-dimensional numerical simulations. The ventilation theory first addresses the kinetics of the interaction between vortex and environmental VWS, specifically the vertical resilience of storms in shear. It mainly involves two explanations, namely the tilt of the potential vorticity column by differential vertical background flow (Jones 1995; Smith et al. 2000), and the generation of low-wavenumber asymmetries (Schecter et al. 2002; Reasor et al. 2004). The theory then explains how ambient air of low entropy interferes the energetics of tropical cyclones and thus weakens the storms from a thermodynamic perspective. Tang and Emanuel (2010) identified two possible pathways for it: inward dry air through the radial inflow and midlevel intrusion of low entropy air into the eyewall.

In addition to the ventilation theory, DeMaria (1996) hypothesized a midlevel warming theory. A third explanation suggests that shear-induced persistent asymmetries in the TC core weaken the mean secondary radial circulation through eddy momentum fluxes (Wu and Braun

2004). In recent years, Riemer and coauthors (Riemer et al. 2010, 2011, 2013) developed a new framework and showed that the inflow layer of the storm is persistently intruded upon by shear induced downdrafts, which are composed of relatively cool and dry air.

Independent of the mechanism, the aforementioned studies suggest that incorporating vertical wind shear is important if idealized TC simulations are to be used in GCM diagnosis and development. The objective of this chapter is to present an extension of the approach of RJ2011 that includes the effects of background vertical wind shear. Note that the intent of such a test case is primarily for a more accurate model evaluation and intercomparison rather than the development of tropical cyclone theory. Our work is organized as follows. Section 2.2 describes the prescribed wind profile, the analytic technique used to add background wind shear, the National Center for Atmospheric Research (NCAR)/Department of Energy (DOE) CAM and the simulation design. Section 2.3 presents the results of idealized TC simulations with different shear profiles. Section 2.4 draws conclusions and discusses the implications.

2.2. Model and methodology

2.2.1. Prescribed wind profile

The wind profile is constructed to be similar to that shown in Fig. 4 of Frank and Ritchie (1999), and its mathematical formula is:

$$u(\varphi,\eta) = u_0 \cos\varphi (1+\tanh\eta_v) + u_1 \cos\varphi \qquad (2.1)$$
$$v(\varphi,\eta) = 0$$

v is the meridional wind, and is set to zero. $u(\varphi,\eta)$ is the zonal wind, a function of the latitude φ and vertical location η with $\eta = p / p_s$. η_v is defined as $\eta_v = 6(1-\eta) - 3.0$, p is pressure and the

surface pressure p_s is initially set to the reference pressure $p_0 = 1000$ hPa. An additional factor of $\cos\varphi$ is introduced in Eq. (2.1) to taper the background zonal wind to zero at the poles. The wind speeds u_0 and u_1 both are tunable constants. u_0 controls the amplitude and direction of the vertical wind shear. When u_0 is positive, it represents westerly shear; when u_0 is negative, it represents easterly shear. A larger magnitude of u_0 leads to larger vertical shear. u_1 controls the magnitude and direction of the mean background flow: positive u_1 denotes westerly mean flow and negative u_1 denotes easterly mean flow. The term $u_1 \cos\varphi$ does not vary with height and thus does not produce vertical shear itself. It affects the shear by changing the shape of the wind profile $u(\varphi, \eta)$. When u_1 is zero or has the same sign as u_0, the direction of the zonal wind is the same across all vertical levels. The shear produced by such a wind profile is called *Unidirectional Shear* in this chapter. When u_1 is non-zero and has the opposite sign of u_0, the direction of the zonal wind changes with height; either from low level westerly to upper level easterly, or from low level easterly to upper level westerly, depending on the sign of u_0. The shear produced by such a wind profile is called *Non-unidirectional Shear,* also referred to as *counter-aligned* orientation of surface mean wind and shear in Rappin and Nolan (2012). For example, let $u_1 = -u_0 (u_0 > 0)$, and $u = u_0 \cos\varphi \tanh\eta_v$. The result is a wind profile with low level easterly and upper level westerly flow, which we refer to as *Non-unidirectional Westerly Shear*. The zonal wind is zero at 500 hPa in this case. With predetermined u_0, one can control the vertical position of the zero point in the zonal wind profile by controlling the value of u_1 via the relationship $u_0 \cos\varphi(1+\tanh\eta_v) + u_1 \cos\varphi = 0$. The position at which the zonal wind goes to zero is referred to the *vertical inflection point* in this chapter. The magnitude of the vertical wind

shear is typically measured as the difference of the zonal wind at 850 hPa and 200 hPa averaged at a given radius (e.g. 500 km radius) from the TC center or in an annular region around the vortex center (Emanuel 2000; Zehr 2003; Zeng et al. 2008, Nolan and Rappin 2008). Here, we follow the procedure used by Zeng et al. (2008), and define the shear as an annular average within 5° latitude around the TC center, which is defined by the location of surface minimum pressure.

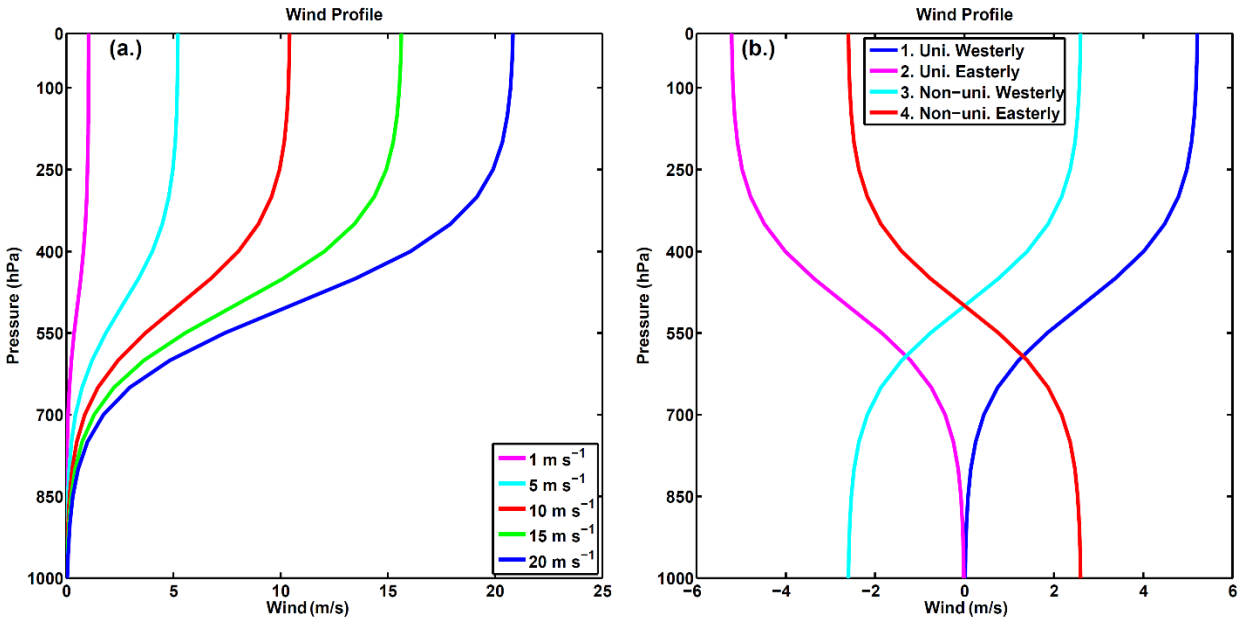

Figure 2.1: (a) Wind profile of unidirectional westerly shear with various magnitudes: $1\ \mathrm{m\,s^{-1}}$, $5\ \mathrm{m\,s^{-1}}$, $10\ \mathrm{m\,s^{-1}}$, $15\ \mathrm{m\,s^{-1}}$ and $20\ \mathrm{m\,s^{-1}}$. (b) Example wind profiles for four different shear cases but same magnitude of $5\ \mathrm{m\,s^{-1}}$. Case 1: Unidirectional (Uni.) westerly shear; Case 2: Unidirectional (Uni.) easterly shear; Case 3: Non-unidirectional (Non-uni.) westerly shear; and Case 4: Non-unidirectional (Non-uni.) easterly shear. Note, unidirectional and non-unidirectional actually describe whether the wind profile that produces the shear changes direction with height or not.

Figure 2.1a shows wind profiles for unidirectional westerly shear with various magnitudes: $1\ \mathrm{m\,s^{-1}}$, $5\ \mathrm{m\,s^{-1}}$, $10\ \mathrm{m\,s^{-1}}$, $15\ \mathrm{m\,s^{-1}}$ and $20\ \mathrm{m\,s^{-1}}$, Here, $1\ \mathrm{m\,s^{-1}}$ denotes weak wind shear,

$5\ \mathrm{m\,s^{-1}}$ corresponds to moderate wind shear and $10\ \mathrm{m\,s^{-1}}$, $15\ \mathrm{m\,s^{-1}}$ and $20\ \mathrm{m\,s^{-1}}$ can be considered as large wind shear. Figure 2.1b shows four different wind profiles, each of which has a bulk shear of $5\ \mathrm{m\,s^{-1}}$. They are numbered as: (1) Unidirectional Westerly (2) Unidirectional Easterly (3) Non-unidirectional Westerly (4) Non-unidirectional Easterly. The additional zonal mean flow in cases (3) and (4) can act as a translational flow that influences the movement of the vortex. The parameters for these examples are listed in Table 2.1.

Shear Direction	Shear Magnitude ($\mathrm{m\,s^{-1}}$)	u_0 ($\mathrm{m\,s^{-1}}$)	u_1 ($\mathrm{m\,s^{-1}}$)	Γ ($\mathrm{K\,km^{-1}}$)
Control Run	0.0	0.0	0.0	7.0
Assessment of unidirectional westerly shear				
Unidirectional Westerly	1.0	0.5303	0.0	7.0013
Unidirectional Westerly	5.0	2.6515	0.0	7.0275
Unidirectional Westerly	10.0	5.3030	0.0	7.0630
Unidirectional Westerly	15.0	7.9545	0.0	7.1012
Unidirectional Westerly	20.0	10.606	0.0	7.1430
Assessment of unidirectional easterly shear				
Unidirectional Easterly	5.0	-2.6515	0.0	6.96493
Unidirectional Easterly	15.0	-7.9545	0.0	6.9116
Assessment of non-unidirectional westerly shear				
Non-unidirectional Westerly	5.0	2.6515	-2.6515	7.0273
Non-unidirectional Westerly	15.0	7.9545	-7.9545	7.0992

Assessment of non-unidirectional easterly shear				
Non-unidirectional Easterly	5.0	-2.6515	2.6515	6.9649
Non-unidirectional Easterly	15.0	-7.9545	7.9545	6.9104

Table 2.1: Summary of the numerical experiments and the values of u_0, u_1 and Γ (background basic vertical lapse rate) for each simulation. u_0 controls the direction and magnitude of wind shear. u_1 represents the direction and magnitude of vertically-constant mean flow, and thereby controls the vertical inflection point of the wind profile. Γ is tuned to adjust the environmental lapse rate at the center of the initial vortex seed (10°N,180°E) to be consistent with control run. Several decimal numbers are retained for the sake of accuracy.

2.2.2. Idealized initial conditions with background vertical wind shear

With the exception of the inclusion of vertical wind shear and its effect (via thermal wind balance) on the meridional temperature gradient, the methodology used to construct the TC initial conditions is identical to that described by RJ2011. Modifications to the RJ 2011 method which are required by the introduction of VWS are presented here. Given a pre-specified wind shear profile (Eq. (2.1)), the goal is to derive an analytic, balanced set of initial conditions that satisfies the steady-state hydrostatic primitive equations (the full derivation is presented in Appendix A). The total virtual temperature field *T* is represented as:

$$T(\lambda,\varphi,\eta) = T_0 - \Gamma z(\eta) + T^*(\lambda,\varphi,\eta), \quad (2.2)$$

where λ is the longitude, T_0 is the sea surface temperature (set equal to 302.15 K in our simulations) and Γ is the user-adjustable virtual temperature lapse rate with units of $\mathrm{K\,m^{-1}}$. The height $z(\eta)$ is derived from the hydrostatic relationship and is represented as $z(\eta) = T_0(1-\eta^{R_d\Gamma/g})/\Gamma$, where $R_d = 287.04$ $\mathrm{J\,kg^{-1}\,K^{-1}}$ is the gas constant for dry air, and g is the gravity with a value of 9.80616 $\mathrm{m\,s^{-2}}$. Recall that $\eta = p/p_s$ with $p_s = p_0$ initially. Given a

specified shear profile, the thermal gradient wind balance requirements lead to the virtual temperature perturbation T^*:

$$T^*(\lambda,\varphi,\eta)=\frac{12\eta}{R_d}u_0\left(\frac{1}{4}\cos 2\varphi-\frac{1}{12}\right)(1-\tanh^2\eta_v)(a\Omega+u_0(\tanh\eta_v+1.0)+u_1), \quad (2.3)$$

where a is the radius of the earth with a value of 6.37122×10^6 m and $\Omega = 7.292115\times10^{-5}$ s^{-1} is the rotational speed of the Earth.

The surface geopotential in balance with the virtual temperature distribution in Eq. (2.2) is given by:

$$\Phi_s(\lambda,\varphi)=\left(\frac{1}{4}\cos(2\varphi)-\frac{1}{12}\right)(2u_0(\tanh(-3.0)+1.0)a\Omega+2u_1a\Omega+(u_0(\tanh(-3.0)+1.0)+u_1)^2) \quad (2.4)$$

Appendix A explains the details of the derivation. The methodology was first used in the derivation of a baroclinic test case (Jablonowski and Williamson, 2006b).

Figure 2.2 shows the wind and temperature fields from the extended test case using the unidirectional westerly $10\ \mathrm{m\,s^{-1}}$ shear case. Figure 2.2a is the longitude-height cross section of the zonal wind at 10°N (the latitudinal center of the vortex seed). Figure 2.2b shows the latitude-height cross section of the zonal wind at 180°E (the longitudinal center of the vortex). The asymmetric structure, especially at high levels, reflects the effects of the superposition of the environmental flow onto the vortex seed. Figure 2.2c shows the longitude-height cross section of wind speed at 10°N. The radius measures the longitudinal distance to the storm center. It represents the overall vortex structure overlaid with sheared environmental flow. Figure 2.2d shows the temperature at 500 hPa. The horizontal environmental temperature gradient can be clearly seen, as well as the TC warm core. Figure 2.2e depicts the surface geopotential. Its

horizontal gradient is in balance with the environmental wind. To compare with the initial condition without wind shear, Figure 2.2f shows the longitudinal-height cross section of the initial vortex seed without a background flow so that the impact of the background flow (Fig. 2.2c) is highlighted. For descriptions of other initial conditions with zero wind shear, we refer the readers to RJ2011.

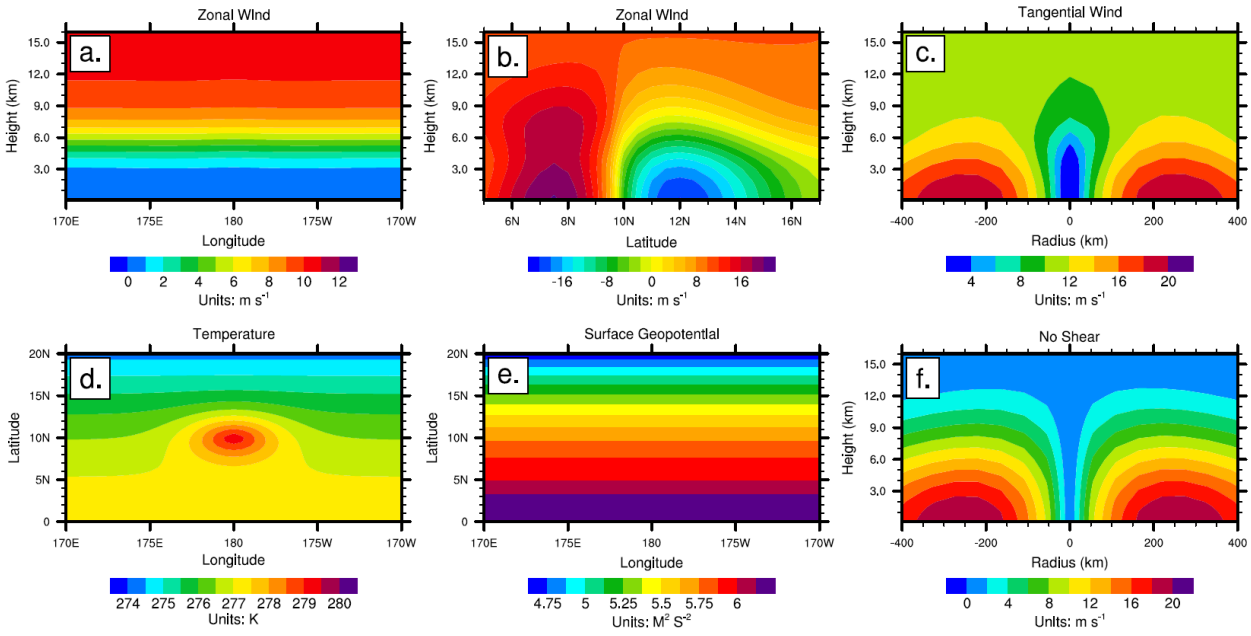

Figure 2.2: Initial conditions for the tropical cyclone test case with $10\ \mathrm{m\,s^{-1}}$ unidirectional westerly shear: (a) Longitude-height cross section of the zonal wind through the center latitude of the vortex at $10^{\circ}\mathrm{N}$, (b) Latitude-height cross section of the zonal wind through the center longitude of the vortex at $180^{\circ}\mathrm{E}$, (c) Longitude-height cross section of the tangential wind centered at $(10^{\circ}\mathrm{N}, 180^{\circ}\mathrm{E})$ (radius denotes the distance to the center), (d) horizontal cross section of the $500\ \mathrm{hPa}$ temperature, (e) horizontal cross section of surface geopotential, and (f) the same as (c) but for no shear case.

2.2.3. Description of the CAM 5.1.1 in Aqua-Planet Mode

The model chosen for our test experiment is the National Center for Atmospheric Research (NCAR)/Department of Energy (DOE) CAM version 5.1.1 (Neale et al. 2010). All simulations

use the Finite Volume (FV) dynamical core and default CAM 5.1.1 physical parameterizations: the Zhang and McFarlane (1995) deep convective scheme, University of Washington (UW) shallow convection scheme (Park and Bretherton 2009), and Bretherton and Park (2009) moist boundary layer turbulence scheme. Each simulation is run for 10 days with identical longitudinal and latitudinal grid spacing of $\Delta\lambda = \Delta\varphi = 0.5^{\circ}$. This horizontal grid spacing is equivalent to approximately 55 km in the equatorial region. It has been used to simulate tropical cyclones in a similar version of CAM5 without VWS (Reed and Jablonowski 2011c), and is equal to, or finer than, the resolution of the models used in the recent Intergovernmental Panel on Climate Change 5th assessment report (IPCC, 2013). It should be noted that there is in theory no limit to the horizontal resolution in our initial conditions.

The model is run with 30 vertical levels, with the model top located at approximately 2 hPa. The time step for the dynamical core is 90 s and 900 s (15 minutes) for physical parameterizations. The initial background surface pressure p_s is set to 1000 hPa and the specific humidity at the surface q_0 is adjusted to 21.3 $\mathrm{g\,kg^{-1}}$ to ensure that the surface relative humidity is consistent with the control run proposed in RJ2011. With the exception of the background temperature, wind and surface geopotential field, the model and vortex seed parameters are identical to the simulation described in RJ2011. The model is run on an aqua-planet with constant sea surface temperature of 302.15 K. The equinox solar constant is set equal to 1365 $\mathrm{W\,m^{-2}}$. Atmospheric constituents (e.g., ozone, carbon dioxide, methane, etc.) are prescribed and distributed symmetrically about the equator. The geophysical constants (e.g., Earth's rotation rate) are prescribed in the aqua-planet experiment and set to default values. These settings are described in the Appendix of Blackburn and Hoskins (2013).

2.2.4. Simulation design

The effects of changes in shear magnitude, direction and inflection point on TC development are examined using simulations initialized from 12 different wind profiles (Table 1). Six simulations are run with unidirectional westerly shear with magnitude of 0 $\mathrm{m\,s^{-1}}$, 1 $\mathrm{m\,s^{-1}}$, 5 $\mathrm{m\,s^{-1}}$, 10 $\mathrm{m\,s^{-1}}$, 15 $\mathrm{m\,s^{-1}}$ and 20 $\mathrm{m\,s^{-1}}$; two are run with unidirectional easterly shear with magnitude of 5 $\mathrm{m\,s^{-1}}$ and 15 $\mathrm{m\,s^{-1}}$; two are run with non-unidirectional westerly shear with magnitude of 5 $\mathrm{m\,s^{-1}}$ and 15 $\mathrm{m\,s^{-1}}$; and two are run with non-unidirectional easterly shear with magnitude of 5 $\mathrm{m\,s^{-1}}$ and 15 $\mathrm{m\,s^{-1}}$. Recall that *Unidirectional shear* refers to cases in which the horizontal direction of the wind does not change throughout the depth of the atmosphere, and the shear is caused only by the change of wind magnitude. *Non-unidirectional shear* means that the horizontal direction of the wind changes from low to high levels in the troposphere, and the shear is caused by changes in both wind magnitude and direction.

Note that the introduction of shear leads to a meridional temperature gradient via the thermal wind balance, and as such the virtual temperature lapse rate varies with latitude. For consistency and to facilitate comparison of the results, all simulations are standardized by adjusting the constant background vertical lapse rate (Γ) so that the total lapse rate is identical at the center of the initial vortex seed, which is at ($10^{\circ}\mathrm{N}$, $180^{\circ}\mathrm{E}$). This leads to a slight change of Γ for different shear cases. The $T^{*}(\lambda,\varphi,\eta)$ in Eq. (2.2) is retained and computed using Eq. (2.3). Table 1 gives the values of u_0, u_1 and Γ for all simulations. Except for wind shear and changes mentioned above ($p_s = 1000$ hPa and $q_0 = 21.3$ g kg^{-1}), all other parameters that define the vortex seed are the same as those used in the control run in RJ2011.

Each of the 12 simulations in Table 2.1 is supplemented with 8 additional perturbation runs (96 total perturbation runs), making the total number of simulations in this study 108. Use of nine-member ensembles gives insight into the robustness of the model simulations for each profile. Each perturbed simulation is created by imposing a small initial perturbation on the position of the vortex seed ($10^{\circ}\mathrm{N}, 180^{\circ}\mathrm{E}$) using the method described by Zarzycki et al. (2014). Specifically, for the perturbation runs, the center of the vortex seed is placed at ($9.5^{\circ}\mathrm{N}, 179.5^{\circ}\mathrm{E}$), ($9.5^{\circ}\mathrm{N}, 180.0^{\circ}\mathrm{E}$), ($9.5^{\circ}\mathrm{N}, 180.5^{\circ}\mathrm{E}$), ($10^{\circ}\mathrm{N}, 179.5^{\circ}\mathrm{E}$), ($10^{\circ}\mathrm{N}, 180.5^{\circ}\mathrm{E}$), ($10.5^{\circ}\mathrm{N}, 179.5^{\circ}\mathrm{E}$), ($10.5^{\circ}\mathrm{N}, 180.0^{\circ}\mathrm{E}$), and ($10.5^{\circ}\mathrm{N}, 180.5^{\circ}\mathrm{E}$), respectively. Note that the intensity, track, vertical structure, precipitation rate and vertical velocity fields in later section are all ensemble means.

2.3. Results

2.3.1. Unidirectional westerly shear

The model is first run with unidirectional westerly shear of various magnitudes to examine its impact on simulated TC intensity, track, vertical structure, precipitation distribution and convective activity.

The simulated intensity evolution (left) and the vortex track (right) over 10 days are shown in Figure 2.3. The intensity is calculated as the maximum wind speed at 100 m above the surface and the vortex center is defined to be the location of the minimum surface pressure. The intensity calculation is consistent with the method used by RJ2011. From Fig. 2.3a, weak ($1\ \mathrm{m\ s^{-1}}$) wind shear stimulates earlier intensification and produces comparable intensity at days 8 -10 compared to a simulation run without shear. Moderate ($5\ \mathrm{m\ s^{-1}}$) shear also stimulates earlier intensification but produces weaker mature tropical storm (days 7 - 10) compared to the no shear case. Strong

shear of 10 $\mathrm{m\,s^{-1}}$ inhibits the storm development and greatly reduces the simulated intensity. Very strong wind shear of 15 $\mathrm{m\,s^{-1}}$ and 20 $\mathrm{m\,s^{-1}}$ completely prevents the vortex seed from intensifying. The intensity in these two cases, which should not be interpreted as storm intensity, is calculated as the maximum wind speed in a square region enclosing the remnants of the vortex. The changes of TC development under various shear magnitudes are consistent with both previous simulation and observational studies (Gray 1975; Wong and Chan 2004; Paterson et al. 2005; Nolan and McGauley 2012), which found that weak and moderate wind shear does not have a strong detrimental effect on tropical cyclone genesis and intensification, while strong shear greatly inhibits TC development.

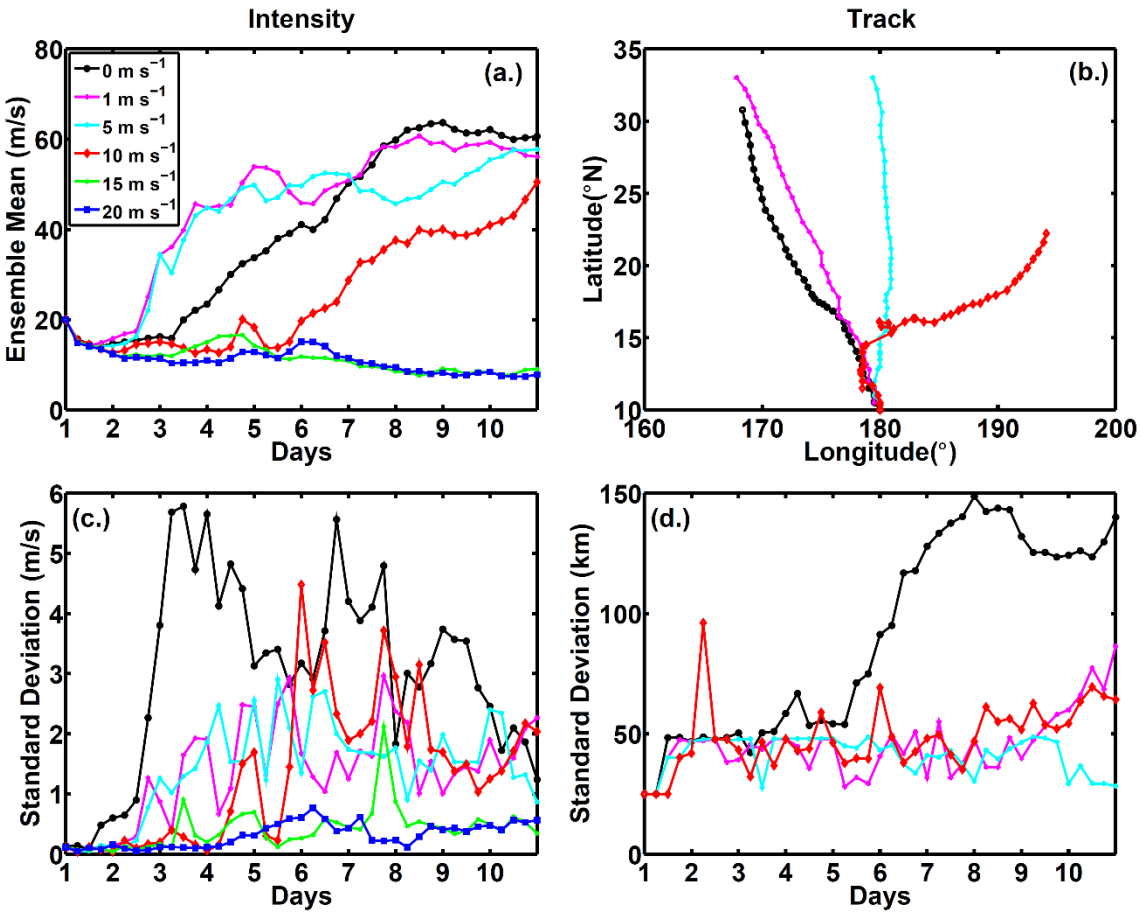

Figure 2.3: Time evolution of the intensity (maximum wind speed at 100 m above the surface) and track (position of the minimum surface pressure) for tropical cyclone-like vortex under various magnitudes of unidirectional westerly shear. (a) Ensemble mean of intensity, (b) Ensemble mean of track, (c) Standard deviation of intensity, and (d) Standard deviation of displacement distance of the storm center.

The track of the simulated tropical cyclone-like vortex (Fig. 2.3b) is also modulated by wind shear. The westerly background wind advects the vortex seed eastward. Without shear and the associated background steering flow, the beta effect (Holland 1983) will move the vortex northwestward in the Northern Hemisphere. In the presence of westerly wind shear, the eastward movement caused by vortex advection in the background zonal wind, tends to offset the westward movement due to the beta effect. As shear reaches $5\ \mathrm{m\,s^{-1}}$, advection and beta drift cancel, and the cyclone moves directly north (Fig. 2.3b). In the high shear cases, the beta drift is completely overwhelmed because the vortex is too weak to have any appreciable beta drift; therefore, the vortex center is advected along with the background flow (towards the east) in these cases. Note, no track is shown for wind shear of $15\ \mathrm{m\,s^{-1}}$ and $20\ \mathrm{m\,s^{-1}}$ as the vortex seed breaks in response to the strong shear. The translational speed of the vortex changes as the track changes. Vertical wind shear and translation speed are widely believed to be key factors affecting tropical cyclone intensity (Chen et al. 2006; Zeng et al. 2008); however, these are commonly treated separately when discussing their impact. Our work suggests that vertical wind shear works in concert with the translation speed. It is difficult to decouple the effect of the two when shear is present.

Figure 2.3c shows that the standard deviation of the vortex intensity ensemble for each shear case is within $5\,\mathrm{m\,s^{-1}}$. This validates that the results are robust to small changes in the numerical integration. Of the cases with non-zero shear, strong shear of $10\ \mathrm{m\,s^{-1}}$ is generally associated

with larger ensemble spread (as represented in the standard deviation; Figs. 2.3c and Fig. 2.3d) than weaker shear at days 6 -10. This is especially true for TC intensity. Also in Fig. 2.3c, the ensemble spread of the $1\ \mathrm{m\,s^{-1}}$ and $5\ \mathrm{m\,s^{-1}}$ shear is relatively large in early stage. Together with early intensification of those two shear cases seen in Fig. 2.3a, it implies that weak or moderate shears can have more impacts on early TC development. Interestingly, the simulations without shear tend to have relatively larger spread than sheared cases in both intensity and track.

Noticeable shear impact on TC development can be further confirmed in the mean vertical structure (Fig. 2.4) averaged over the mature stage (days 9-10), among vortices that develop in a sheared environment. Compared to the no shear case (Fig. 2.4a), the vertical extent (indicated by the $20\ \mathrm{m\,s^{-1}}$ isotach) is comparable for shear cases $1\ \mathrm{m\,s^{-1}}$, $5\ \mathrm{m\,s^{-1}}$ and $10\ \mathrm{m\,s^{-1}}$. In contrast, the vertical extent of the inner core is suppressed in sheared cases. This can be seen by the shrinking of the regions encompassed by the $40\ \mathrm{m\,s^{-1}}$ and $60\ \mathrm{m\,s^{-1}}$ isotachs. For very strong shear of $15\ \mathrm{m\,s^{-1}}$ and $20\ \mathrm{m\,s^{-1}}$, the vortex seed is broken apart and no storm develops. Thus, we only see the sheared environmental flow in Fig. 2.4e and Fig. 2.4f. The structural change here is consistent with the intensity change in Fig. 2.3. The reasonably realistic vertical characteristics of the sheared cases demonstrate that the shear technique is congruent with the original TC test case throughout the model integration. The storm develops in a similar manner with changes consistent with the expected influence of vertical wind shear.

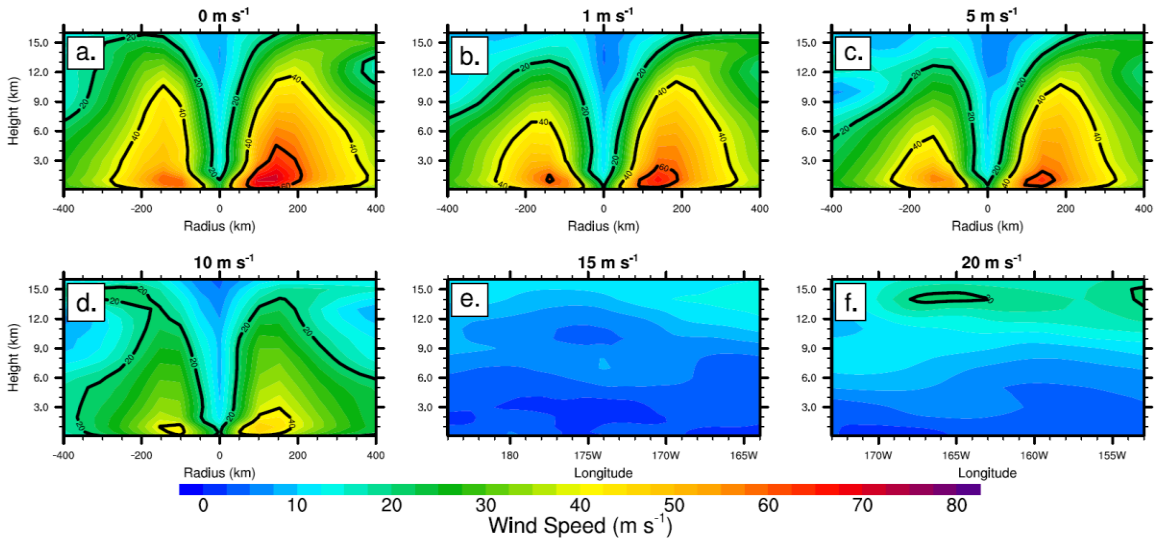

Figure 2.4: Longitude-height cross sections of the tropical cyclone-like vortex averaged over days 9-10 for unidirectional westerly shear: (a). 0 $\mathrm{m\,s^{-1}}$, (b). 1 $\mathrm{m\,s^{-1}}$, (c). 5 $\mathrm{m\,s^{-1}}$, (d). 10 $\mathrm{m\,s^{-1}}$, (e). 15 $\mathrm{m\,s^{-1}}$, and (f). 20 $\mathrm{m\,s^{-1}}$. The radius denotes the distance to the center of the vortex. Each cross section shown is the mean value of the nine ensemble runs. The solid black line marks the contour of wind speed with value of 20 $\mathrm{m\,s^{-1}}$, 40 $\mathrm{m\,s^{-1}}$, and 60 $\mathrm{m\,s^{-1}}$.

In addition to the cyclone track and intensity, we also examine the effect of shear on the precipitation distribution and convective activity during the mature stage. The shear induced asymmetric precipitation distribution is well captured (Fig. 2.5). In the no-shear case, the maximum rainfall occurs in the right side relative to the direction of movement (black arrow). The maximum rainfall occurs in the down-shear left (DSL) quadrant in 1 $\mathrm{m\,s^{-1}}$ (Fig. 2.5b), 5 $\mathrm{m\,s^{-1}}$ (Fig. 2.5c) and 10 $\mathrm{m\,s^{-1}}$ (Fig. 2.5d) cases. The maximum in the 10 $\mathrm{m\,s^{-1}}$ shear case (Fig. 2.5d) is not as clearly evident; however, close inspection reveals more rainfall to be concentrated in the DSL quadrant. These results are consistent with observational studies, which show that the maximum rainfall rate varies with storms and often occurs in the down-shear left quadrant (Cline 1926; Marks 1985; Burpee and Black 1989; Chen et al. 2006). Ueno (2007) also shows that the shear-induced rainfall asymmetry is related to the vortex strength in both observational analysis

and numerical modeling studies. The total precipitation is calculated as accumulated rainfall (where the precipitation rate exceeds 2 $\mathrm{mm\,hr^{-1}}$) over the last 48 hours integrated over the tropical cyclone-like vortex region as circled by the black solid line in each plot. It is tabulated in the lower left corner of each plot in Fig. 2.5. In general, the total rainfall is correlated to TC strength. The three storms with no/weak/moderate shear exhibit substantially higher precipitation than the 10 $\mathrm{m\,s^{-1}}$ case. The 15 $\mathrm{m\,s^{-1}}$ and 20 $\mathrm{m\,s^{-1}}$ cases exhibit little precipitation as the initial vortex seed does not develop. For this reason, the precipitation distribution for the 20 $\mathrm{m\,s^{-1}}$ case is not shown.

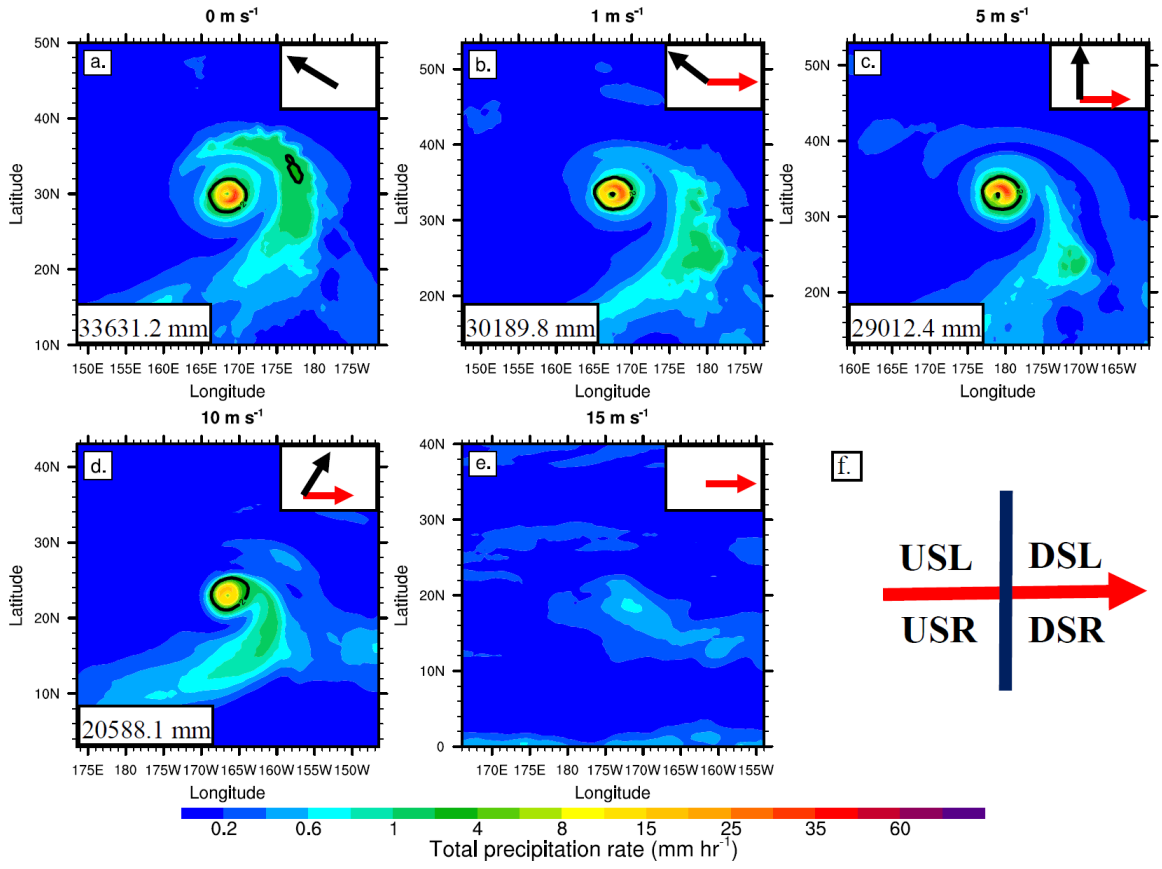

Figure 2.5: Total precipitation rate (convective precipitation rate + large scale precipitation rate) of the tropical cyclone averaged over days 9-10 for unidirectional westerly shear: (a). 0 $\mathrm{m\,s^{-1}}$, (b). 1 $\mathrm{m\,s^{-1}}$, (c). 5 $\mathrm{m\,s^{-1}}$, (d). 10 $\mathrm{m\,s^{-1}}$, and (e). 15 $\mathrm{m\,s^{-1}}$. (f) shows the four quadrants relative to shear direction. USL: up-shear left, USR: up-shear right, DSL: down-shear left, DSR: down-

shear right. Shear direction is indicated by the red arrow and black arrow denotes the storm moving direction. Each plot is the mean of the nine ensemble members. The left bottom corner shows the area-weighted last 48-hours accumulated precipitation accounting for precipitation rate greater than 2 $mm\ hr^{-1}$, circled by the black solid line.

Figure 2.6 shows the longitude-height cross section of vertical velocity along the direction of shear through the vortex center averaged over days 9-10. Compared to the 0 $m\ s^{-1}$ case (Fig. 2.6a), convective activity is increased along the shear direction in the 1 $m\ s^{-1}$ (Fig. 2.6b) and 5 $m\ s^{-1}$ (Fig. 2.6c) cases, and reduced in the upshear portion, as indicated by the -1.0 $Pa\ s^{-1}$ isotach. It has also been shown that wind shear induces asymmetric structure changes with respect to the eye center (Frank and Ritchie 1999). Shear tends to initiate stronger convection activity along the shear direction and suppresses the convection in the upshear direction (Reasor et al. 2013) as seen here. For strong shear (10 $m\ s^{-1}$), the convection in both upshear and downshear directions is greatly inhibited, which is consistent with the changes in intensity, vertical structure and precipitation distribution noted earlier.

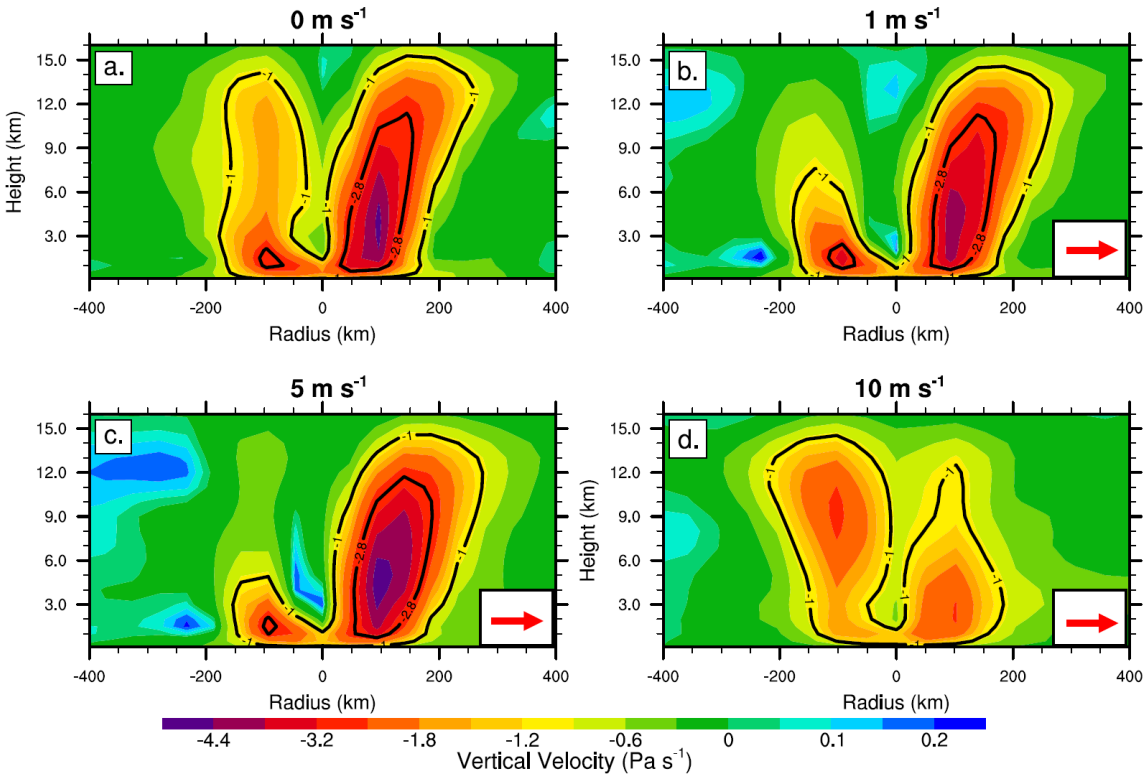

Figure 2.6: Longitude-height cross sections of vertical velocity (ensemble mean) averaged over days 9-10 for unidirectional westerly shear: (a). 0 $\mathrm{m\,s^{-1}}$, (b). 1 $\mathrm{m\,s^{-1}}$, (c). 5 $\mathrm{m\,s^{-1}}$, and (d). 10 $\mathrm{m\,s^{-1}}$. The radius denotes the distance to the vortex center. The solid black line marks the velocity of -1.0 $\mathrm{Pa\,s^{-1}}$, and -2.8 $\mathrm{Pa\,s^{-1}}$. Red arrow indicates shear direction.

2.3.2. Unidirectional easterly shear and non-unidirectional shear

The results presented in the previous section show that the effect of unidirectional westerly shear on tropical cyclones can be reasonably represented in our idealized simulations. We now examine the effect of differing shear direction and vertical inflection point of the wind profile. Specifically, we compare four types of shear cases: (1) unidirectional westerly shear; (2) unidirectional easterly shear; (3) non-unidirectional westerly shear (equivalent to unidirectional westerly shear plus background easterly mean flow); and (4) non-unidirectional easterly shear

(equivalent to unidirectional easterly shear plus background westerly mean flow). Recall that the wind profiles of these four shear cases are presented in Fig. 2.1b.

It has been shown that westerly shear has a different effect on TC development than easterly shear with the same magnitude (RF2007; Zeng et al. 2010), with the former being more frequently seen in observation (Zeng et al. 2010). A few studies have also examined non-unidirectional shear (e.g. low level easterly to high level westerly; Riehl and Shafter 1994; Aiyyer and Thorncroft 2006). Previous studies suggest that in considering vertical shear effects on TC intensity change, it is important not only to examine the shear between two standard pressure levels, but also the vertical profile of the shear (Zeng et al. 2010; Wingo and Cecil 2010, hereafter WC2010). Following these studies, this section compares the impact of unidirectional shear and non-unidirectional shear in two opposite directions (westerly shear and easterly shear) on simulated intensity, track, vertical structure, precipitation distribution and convective activity. The goal of our analysis is to show that the technique is robust to changes in shear direction and profile, and users may flexibly specify any realistic vertical wind profile. To the authors' knowledge, there are no comprehensive statistical observational analyses regarding which ocean basin typically exhibits a given type of wind shear. However, based on Hadley cell theory, we may surmise that westerly shear (both unidirectional and non-unidirectional) should be more commonly observed in all basins, while easterly shear (both unidirectional and non-unidirectional) occurs primarily during the Monsoon season over the Pacific and Indian Oceans.

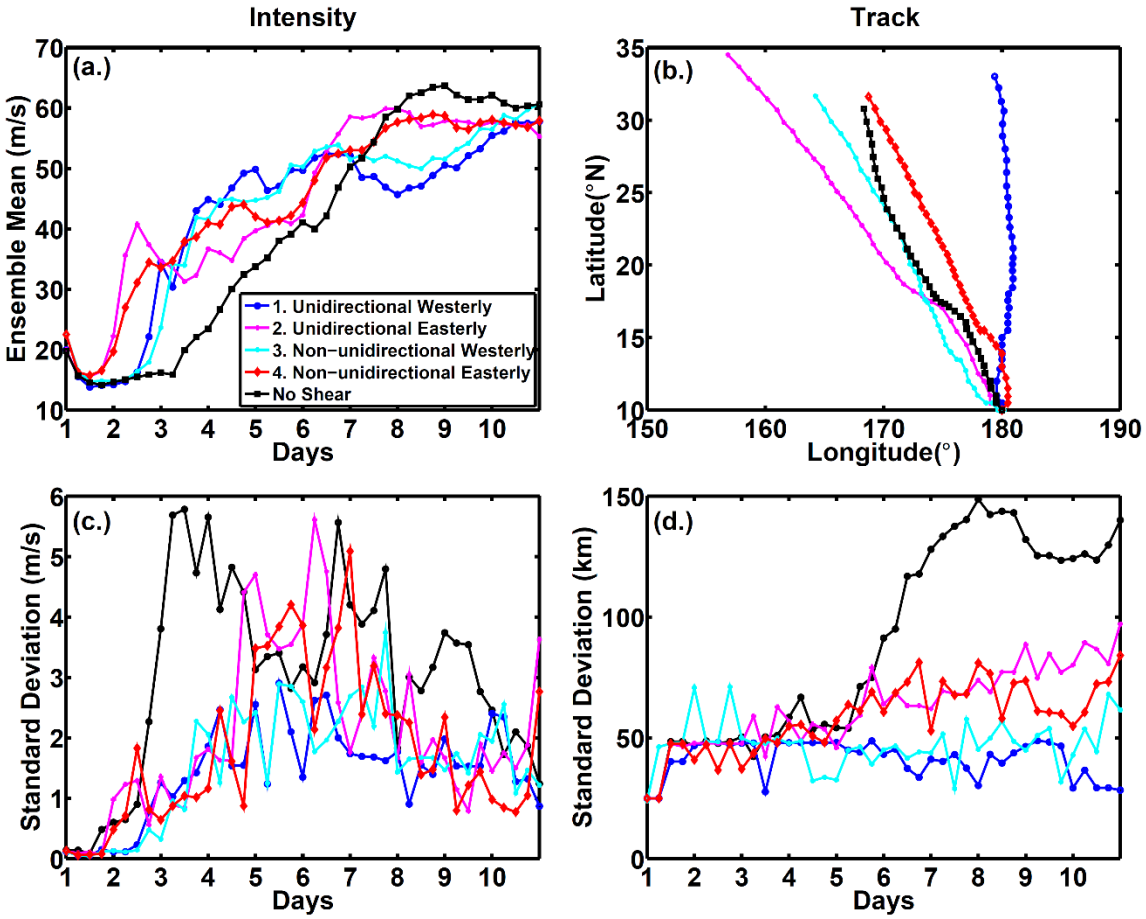

Figure 2.7: Time evolution of the intensity (maximum wind speed at 100 m above the surface) and track (position of the minimum surface pressure) for tropical cyclone-like vortex for four shear cases with shear magnitude of 5 $\mathrm{m\,s^{-1}}$, compared to control run. (a) Ensemble mean of intensity, (b) Ensemble mean of track, (c) Standard deviation of intensity, and (d) Standard deviation of displacement distance of the storm center.

Figure 2.7 shows the corresponding ensemble mean intensity evolution and track for the four profiles with moderate shear of 5 m s^{-1}. In all cases, the application of shear stimulates earlier TC intensification. Storms with easterly shear intensify more rapidly than westerly shear case following initialization (days 1-3, Fig. 2.7a). At the mature stage (days 6-9), easterly shear (case 2 and 4 in Fig. 2.7a) of 5 $\mathrm{m\,s^{-1}}$ is less detrimental for TC intensification than westerly shear

(case 1 and 3 in Fig. 2.7a). This is consistent with previous studies (Tuleya and Kurihara 1981; Bender 1997; Black et al. 2002; RF2007; Zeng et al. 2010). This is well explained by the beta-shear theory (RF2007), which predicts that easterly shear should have a weaker effect than westerly shear when the tropical cyclone moves in the northwestward direction because the induced southeastward beta shear will partially cancel the easterly shear and partially strengthen the westerly shear. In our later results, we will show that strong easterly shear ($15\ \mathrm{m\,s^{-1}}$) is less detrimental than strong westerly shear, as strong shear inhibits TC development.

A weak extra mean flow has minor impact on TC intensity (comparing case 1 with case 3, and comparing case 2 with case 4 in Fig. 2.7a). In contrast, the track changes significantly with wind shear and extra mean flow. Easterly mean flow shifts the vortex westward, while westerly mean flow shifts it eastward. Westerly (easterly) shear somewhat compensates the effect of easterly (westerly) mean flow on the change in track. A different wind profile with the same magnitude of shear also leads to different ensemble spread of intensity and track (Figs. 2.7c and 2.7d). Easterly shear results in larger spread in intensity during the intensification stage phase (days 6-7). It also causes larger spread than westerly shear does on track (days 3-10, Fig. 2.7d). Nevertheless, all the spread is small. Intensity spread is within $5\ \mathrm{m\,s^{-1}}$ and track spread is within 1° distance (about 110 km). This provides additional evidence of the numerical robustness of the shear introduction technique.

Figure 2.8 shows the vertical extent of tangential wind for the four shear cases with $5\ \mathrm{m\,s^{-1}}$ averaged over days 9-10. Compared to the no shear case (Fig. 2.4a), the extent of the outflow is similar (indicated by the $20\ \mathrm{m\,s^{-1}}$ isotach), but the inner core is weakened as shown by the reduced extent of the $60\ \mathrm{m\,s^{-1}}$ isotach. This result is consistent with the intensity change shown

in Fig. 2.7a. All four moderate shear cases produce a slightly weaker storm at the mature stage, the vertical structure is generally preserved and the horizontal wind distribution is retained. This again confirms that the technique of adding shear works appropriately throughout the model integration when combined with the original TC test case.

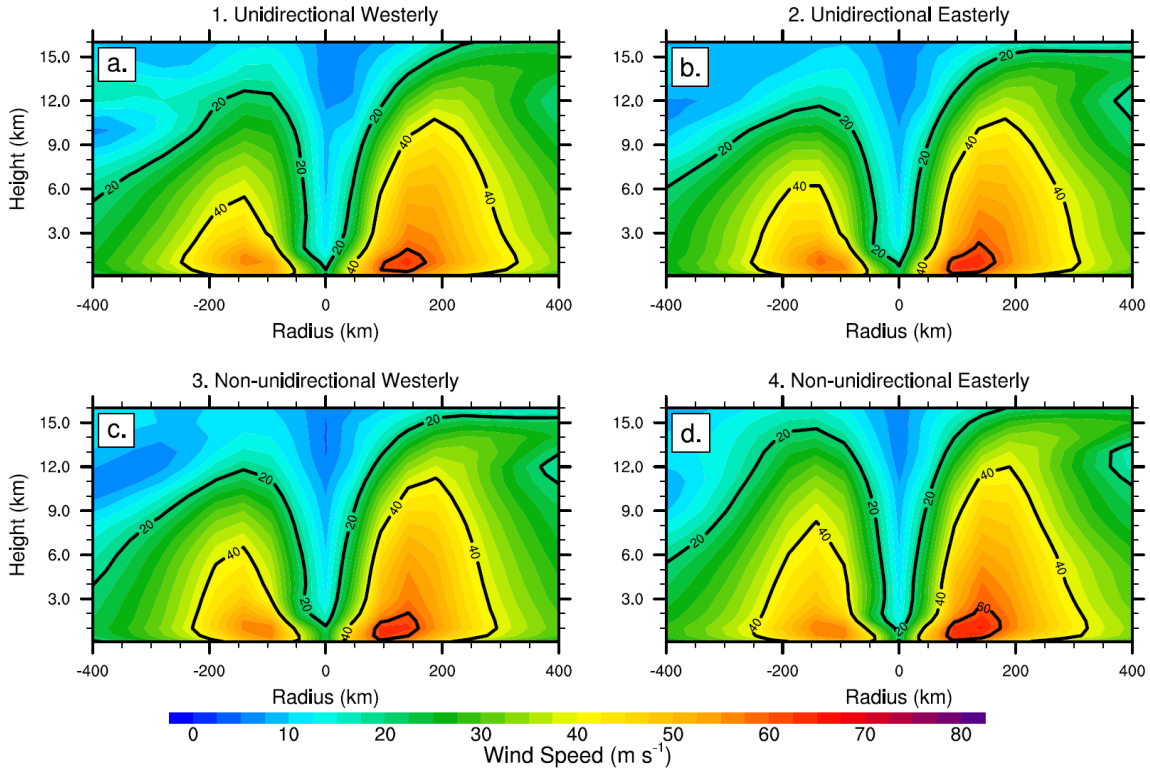

Figure 2.8: As Figure 2.4 but for four shear cases with magnitude of $5\ \mathrm{m\ s^{-1}}$.

Figure 2.9 shows the precipitation distribution for the four shear cases. Again, the maximum rainfall rate and greatest areal rainfall extent lie in the down-shear left quadrant for both unidirectional westerly shear (Fig. 2.9a) and non-unidirectional westerly shear (Fig. 2.9c). Using satellite data, WC2010 showed that westerly shear formed slightly more asymmetric patterns than easterly shear. This can be seen in the slight differences in rainfall distribution between Figs. 2.9c and 2.9d. Easterly shear has a different impact on the rainfall distribution than westerly

shear. The maximum rainfall in the easterly shear case (Fig. 2.9b) occurs in the right front quadrant (relative to the direction of movement) rather than in the down-shear left quadrant. This result seems to stand in contrast to previous studies which found that the rainfall maximum tends to occur in the down-shear left quadrant (e.g., Franklin et al. 1993; Bender 1997). However, WC2010 also found two easterly shear samples that tended to have more precipitation occurring in the up-shear side, which is the case here. We suggest the following explanation for our easterly shear cases. It has been shown that the translational speed and vertical wind shear both affect the precipitation asymmetry. According to Chen et al. (2006), when shear is $< 5\ \mathrm{m\,s^{-1}}$, TC translation speed is more dominant than shear in determining the position of maximum precipitation. Even though the prescribed shear here is $5\ \mathrm{m\,s^{-1}}$, the overall shear might be smaller than $5\ \mathrm{m\,s^{-1}}$ when the beta shear effect is included. The position of the maximum rainfall with respect to the storm direction for westerly shear (Fig. 2.9a) and easterly shear (Fig. 2.9b) is consistent with the results of Bender (1997; Fig.15), who found that the vertical profile of the asymmetric wind is one of the key factors in determining the structure of quasi-steady asymmetries in the interior region of tropical cyclones. The integrated precipitation over regions where the rain rate exceeds $2\ \mathrm{mm\,hr^{-1}}$ (as circled by the black solid line) for the last 48-hours is depicted in the lower left corner of Figs. 2.9a – 2.9d. Interestingly, while TC intensity under easterly shear is slightly stronger than that of westerly shear, the total precipitation in unidirectional easterly shear is significantly smaller than that of westerly shear (comparing Fig. 2.9b to Fig. 2.9a). This may arise from the reduction of convective activity inside the storm in the easterly shear cases, which will be shown later. The total precipitation is reduced in the non-unidirectional westerly shear case (Fig. 2.9c) compared to unidirectional westerly shear (Fig. 2.9a) due to an extra easterly mean flow. In contrast, for unidirectional easterly shear (Fig. 2.9b),

an extra westerly flow increases the total precipitation (Fig. 2.9d). This suggests that the background mean flow has significant influence on TC precipitation changes even though it has a relatively minor effect on intensity (Fig. 2.7a).

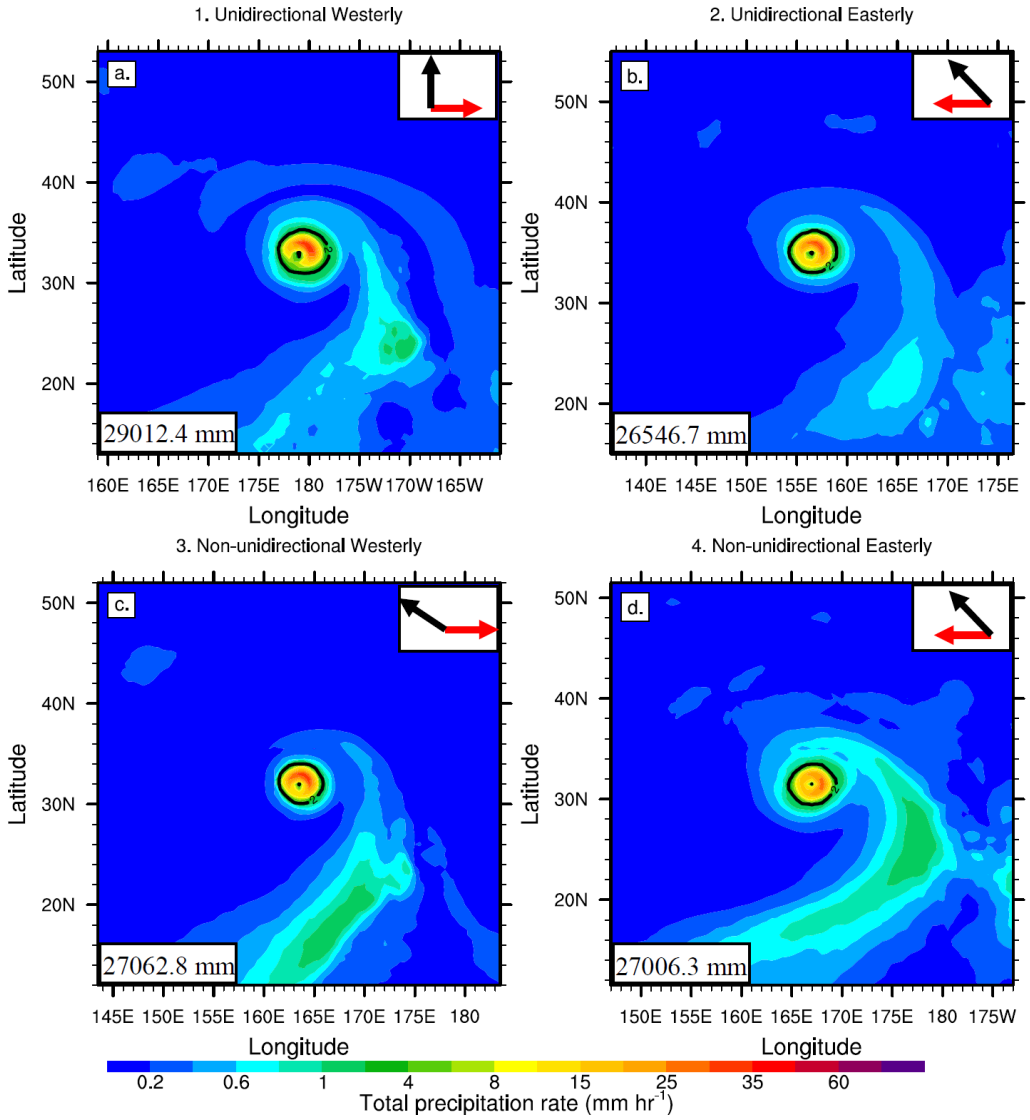

Figure 2.9: Total precipitation rates (convective precipitation rate + large scale precipitation rate) averaged over days 9-10 for (a) unidirectional westerly shear, (b) unidirectional easterly shear, (c) non-unidirectional westerly shear, and (d) non-unidirectional easterly shear. The wind shear is 5 $\mathrm{m\,s^{-1}}$ for all four cases. Each plot shows the ensemble mean. Shear direction is indicated by red arrow and black arrow denotes the storm moving direction. The left bottom corner shows the area-weighted last 48-hours accumulated precipitation for precipitation rate greater than 2 $\mathrm{mm\,hr^{-1}}$ as circled by the black solid line. Note, unidirectional and non-unidirectional actually describe whether the wind profile that produces the shear changes direction with height or not.

Figure 2.10 shows the longitude-height cross section of convective activity (vertical velocity) inside the storm for the four shear cases. We have compared the unidirectional westerly shear (Fig. 2.10a) to no shear cases in the earlier section. For both easterly shear cases (Fig. 2.10b and Fig. 2.10d), the convection along the shear direction (the left convection branch with respect to vortex center) is increased (as indicated by the -2.0 $\mathrm{Pa\ s^{-1}}$) and shear induces weaker upward motion in the upshear direction (indicated by the -2.0 $\mathrm{Pa\ s^{-1}}$ and -3.4 $\mathrm{Pa\ s^{-1}}$), compared to no shear case (Fig. 2.10 e). The shear induced asymmetric convective activity is not significant in the non-unidirectional westerly shear case (Fig. 2.10c). Generally, the shear induced asymmetry in convection is consistent with previous studies. This plot also explains the precipitation difference seen in Fig. 2.9. The two westerly shear cases tend to have more precipitation than the two easterly shear cases (Fig. 2.9) because convection in the former situation is generally stronger than that in the latter cases. This is due to the shear-induced asymmetric convection. Also, non-unidirectional westerly shear has slightly weaker convection than that of unidirectional westerly shear. This is why the rainfall is slightly smaller in the former case. The same explanation holds for the rainfall difference between unidirectional easterly shear case and non-unidirectional easterly shear case.

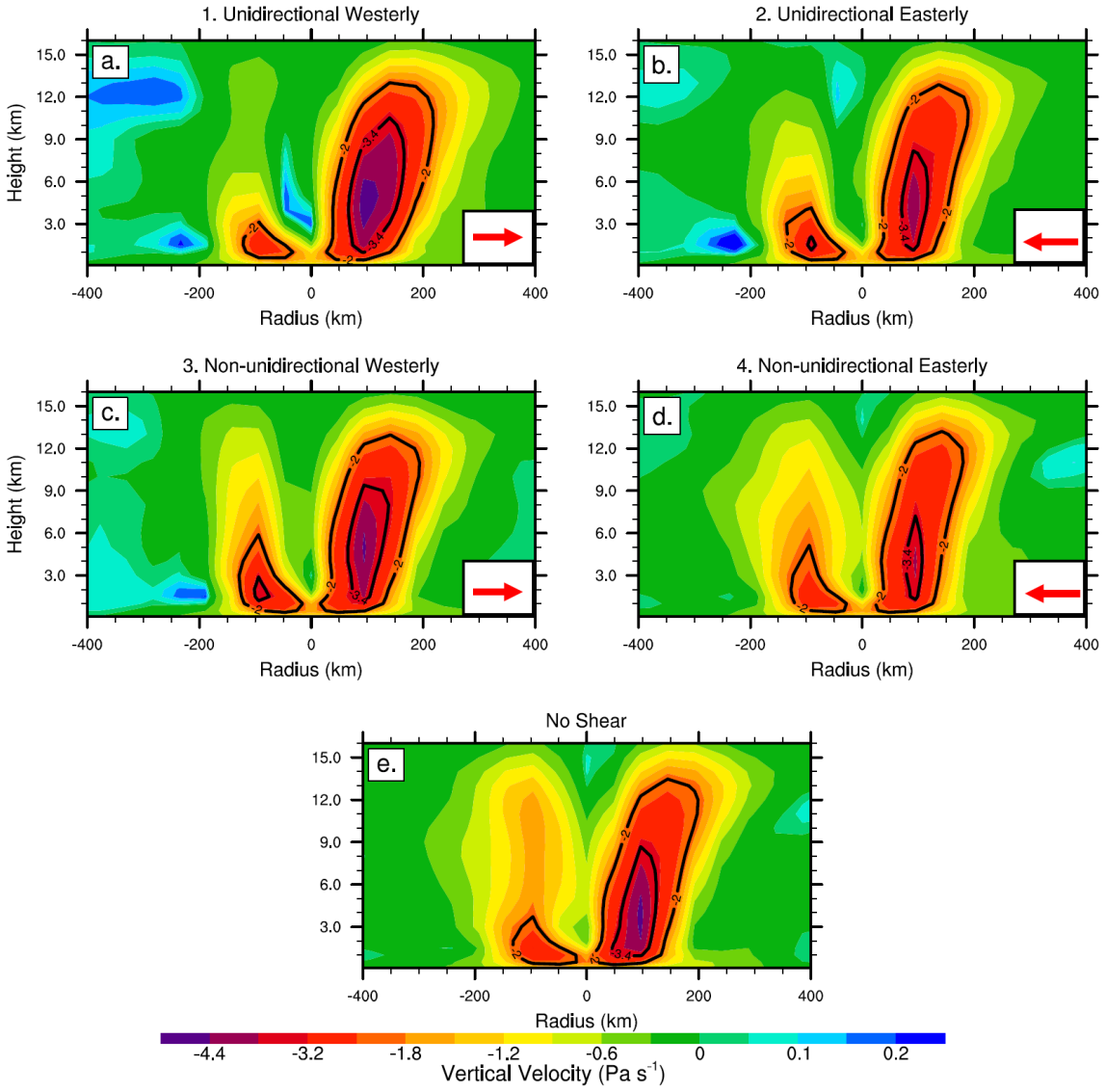

Figure 2.10: The same as Figure 2.6 but for the four shear cases with magnitude of $5\ \mathrm{m\,s^{-1}}$. (a). unidirectional westerly, (b). unidirectional easterly, (c). non-unidirectional westerly, (d). non-unidirectional easterly, and (e). no shear. Red arrow indicates shear direction. Note, unidirectional and non-unidirectional actually describe whether the wind profile that produces the shear changes direction with height or not.

Figure 2.11 depicts intensity and track ensemble mean and standard deviation for the strong shear cases ($15\ \mathrm{m\,s^{-1}}$). Easterly shear (case 2, 4 in Fig. 2.10a) has a considerably weaker effect on inhibiting TC development than westerly shear (case 1, 3 in Fig. 2.10b). This finding is

consistent with previous idealized numerical modelling studies (Tuleya and Kurihara 1981; RF2007). An extra westerly mean flow (comparing case 4 with case 2 in Fig. 2.10a) reduces the TC intensity slightly. This is consistent with results obtained by Tuleya and Kurihara (1981), who found that under uniform westerly environmental flow, the initial perturbation developed more. Wind shear and mean flow both modulate the track. The vortex moves further to the south (north) under the influence of weak easterly (westerly) vertical shear than it does with no shear (Fig. 2.3 and Fig. 2.7), which is to the left side of the track observed in the presence of vertical shear. Wu and Emanuel (1993) and Flatau et al. (1994) also present results that demonstrate cyclone motion to the left of the vertical shear. Combined with Fig. 2.7, we see that easterly shear has a weaker effect than the westerly shear, and larger mean flow is more detrimental to TC intensification. The numerical spread for two easterly shear cases is within $5\ \mathrm{m\,s^{-1}}$ for intensity and 1° distance for track, which is reasonable.

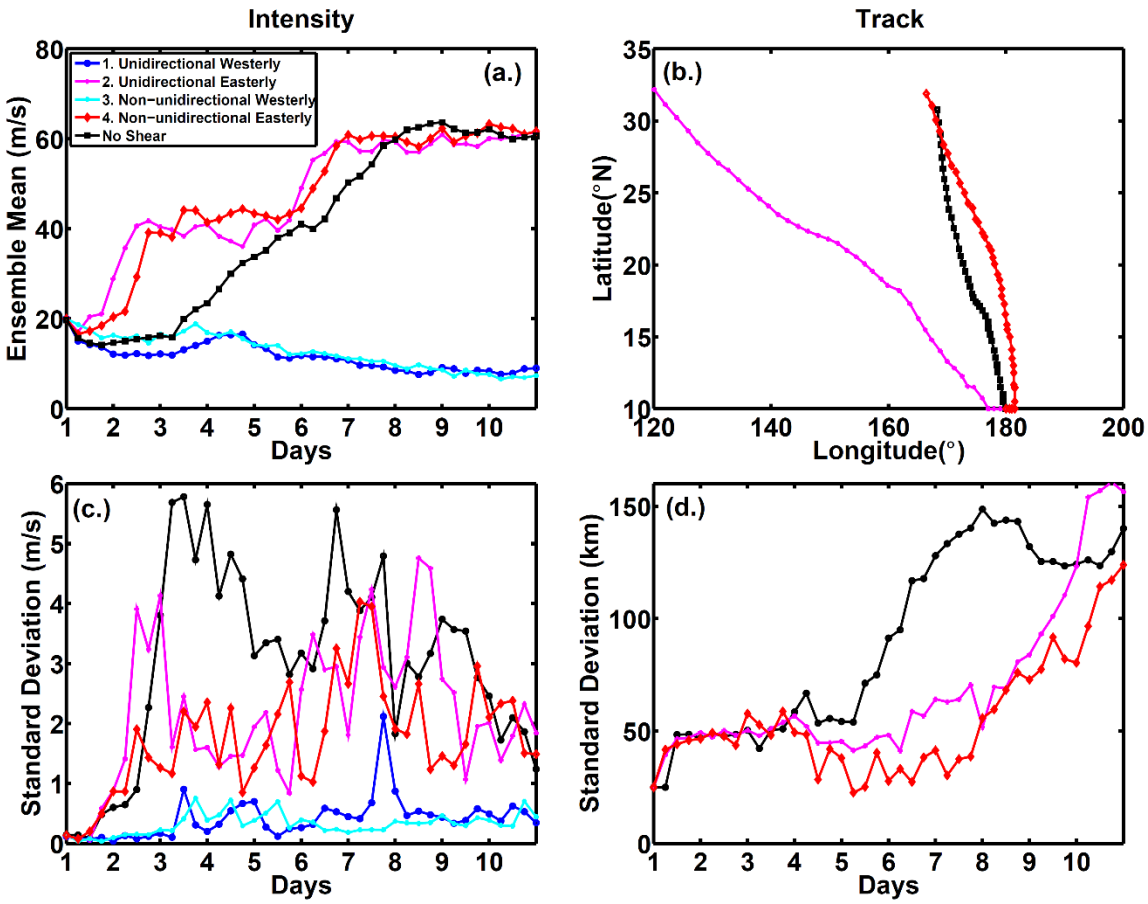

Figure 2.11: The same as Figure 2.7, however for wind shear of 15 $\mathrm{m\,s^{-1}}$. Case 3 and 4 are not shown in (b) (d) as no tropical cyclone is developed in these two cases.

2.4. Summary

Vertical wind shear (VWS) is a key factor in Tropical Cyclone (TC) genesis and intensification. Furthermore, it provides a possible dynamical connection between Atlantic major hurricane activity and three remote atmospheric patterns: the El Niño Southern Oscillation, eastern Pacific sea surface temperature, and West African precipitation (Goldenberg and Shapiro 1996). Moreover, very few observed TCs develop in a zero shear environment and previous studies suggest that incorporation of VWS is very important in numerical TC simulations. In this study, we extend a pre-existing analytical TC test case to include vertical wind shear in idealized

AGCM TC simulations, and apply it to the NCAR/DOE CAM model. While we use this particular model, the framework developed here is extendable to other AGCMs as well.

We evaluate the effect of idealized shear on simulated TC intensity, track, vertical structure, precipitation and storm convective activity. The results are reasonable and self-coherent. Realistic characteristics of vertical structure, precipitation and storm convective activity in sheared cases further confirm that the added background shear works acts appropriately on the original test case during the 10 day numerical integration. The small ensemble spread of intensity and track also validates that the simulations with shear are robust to numerical perturbations. Additionally, the shear-induced intensity change and structural asymmetry is reasonably well captured in this idealized framework.

Consistent with findings from observations and high resolution process studies, weak and moderate unidirectional westerly shear stimulates earlier intensification and produces TCs with comparable intensity to those that develop in the no shear case. Strong shear of 10 $\mathrm{m\,s^{-1}}$ greatly inhibits the development of simulated TCs, while very strong shear of 15 $\mathrm{m\,s^{-1}}$ and 20 $\mathrm{m\,s^{-1}}$ completely prevents TC formation. Easterly shear has considerably weaker detrimental effects than westerly shear in modulating TC intensity. Beyond that, the asymmetric features of the TC precipitation distribution and convection induced by vertical wind shear are captured in our idealized framework. The TC track is strongly influenced by background vertical wind shear in a way that depends on which direction the shear is oriented. With non-unidirectional shear, the additional vertically-constant mean flow across all the vertical levels has a slightly detrimental effect on intensity and more significant impact on precipitation change.

A detailed diagnosis of the shear effects on precipitation and cyclone structure is beyond the scope of this chapter. Our results agree well with the diagnosis from observations and idealized simulations; however, due to the coarse horizontal resolution, idealized set up of the vortex seed, and the fact that all physical processes are parameterized in the global climate models, the details of our results are not expected to be identical to previous findings, especially with respect to intensity change, vertical structure and precipitation distribution. The results suggest that the extended technique realistically represents the wind shear effect on TC simulation, provides a robust tool for simulating the interaction between TC intensification and VWS in AGCMs, and thus provides a more realistic and relevant model development tool. It is an extension to the current TC test case of RJ2011, which can be used to evaluate the effect of numerical algorithms, physical parameterizations, and model resolution on the representation of TC development in AGCMs (Reed and Jablonowski 2012). It can also be used as a tool for intercomparison among different AGCMs by imposing identical initial conditions to evaluate their performance on simulating TCs.

CHAPTER 3

Uncertainty Quantification Framework for Multivariate Sensitivity Analysis of Atmospheric Dynamical Systems: Evaluating the Sensitivities of AGCM-Simulated Tropical Cyclones to Model Initial Conditions

3.1. Introduction

Atmospheric dynamical systems such as tropical cyclones, extratropical cyclones, frontal systems, etc. can cause significant economic loss and human mortality. The growth and decay of these systems are strongly influenced by the atmospheric dynamic and thermodynamic conditions, such as pre-existing atmospheric disturbances, sea surface temperature, atmospheric stability, relative humidity, etc. It has long been of interest to study how various atmospheric conditions affect the evolution of dynamical systems, and how the characteristics (e.g. intensity, convection, precipitation, scale) of the dynamic systems interact with each other. For example, Hill and Lackmann (2009) studied the influence of environmental humidity on tropical cyclone size. Jiang (2012) examined the relationship between tropical cyclone intensity change and precipitation.

Numerical models with different levels of complexity are the primary tools used to understand the influence of environmental factors on weather systems, and the relationships among different characteristics. Sensitivity analysis is essentially a process of characterizing two types of relationships: (1) model input – output relationships, and (2) model output – output

relationships. Here, we propose to use an uncertainty quantification framework (UQF) to examine the sensitivity of model output to input for multivariate input parameters that allows the interactive effect among different input parameters. With a large number of ensemble runs, it allows us to examine the model output – output relationships in a robust way. Specifically, our UQF refers to a Latin Hypercube Sampling (LHS) method and a surrogate model, which produces statistically robust results when quantifying relationships. LHS has been shown to simulate uncertainty as accurately as a Monte Carlo sampling method while using far fewer samples (McKay et al., 1979; Iman and Conover, 1980; Loh 1996), and has been widely used for model uncertainty assessment in environmental, biostatistical and space sciences (Isukapalli and Georgopoulos 1999; Hossain, Anagnostou and Bagtzoglou 2005). The surrogate model mimics the behavior the simulation model as closely as possible, and is much more computationally efficient than the unapproximated simulation model. Typical surrogate models include Multivariate Adaptive Regression Splines (MARS; Friedman et al., 1995), Multiple Additive Regression Trees (MART; Friedman, 1999; Friedman and Meulman, 2003), and Gaussian Spatial Process models (GaSP; Sacks et al, 1989; Craig et al., 2001).

We illustrate the idea with a case study focused on evaluating the sensitivities of Atmospheric General Circulation Model (AGCM)-simulated tropical cyclones to atmospheric environmental factors, including: size and strength of the initial perturbation, sea surface temperature (SST), atmospheric instability, and mid-level relative humidity. These are widely believed to exert the primary influence on the dynamical evolution of TCs (Gray 1968, 1979; MaCaul 1991; Emanuel et al. 2004; Emanuel 2007; Zeng et al. 2007, 2008; Davis et al. 2012). Nowadays, extensive attention has been paid to simulating TCs and predicting their future changes using AGCMs (Manganello et al. 2012; Murakami 2012; Camargo 2013; Emanuel 2013;

Knutson et al. 2013; Tory et al. 2013). Characterizing sensitivities of AGCM-simulated tropical cyclones to atmospheric environmental factors reveal the skill with which an AGCM configuration can simulate and represent TCs.

An idealized TC test case designed specifically for the purpose of model evaluation (Reed and Jablonowski 2011a) is utilized in our study. It provides a single initial weak warm-core vortex seed to the AGCM in an aqua-planet configuration with constant sea surface temperature. It retains the complete construction of the AGCM, and can realistically represent the process of TC development. Such design yields a TC test case with highly reduced computational cost, freely tunable initial conditions and easy-to-extract TC features. This test case has been shown to successfully reveal the impact of physical parameterizations on TC simulations (Reed and Jablonowski 2011b) and in assessing modelled TC uncertainty (Reed and Jablonowski 2011c).

Overall, this chapter proposes an UQF for the study of dynamical systems that is capable of retrieving relationships of traditional interest. We validate the idea with a case study that assesses the sensitivities of simulated TC-relevant characteristics to initial vortex properties and atmospheric conditions. The TC-relevant characteristics are TC intensity, precipitation rate (PRECT), shortwave cloud radiative forcing (SWCF), longwave cloud radiative (LWCF), cloud ice water path (IWP) and cloud liquid water path (LWP). The initial vortex characteristics mainly refer to the radius of maximum wind speed (RMW), and the maximum wind speed (MWS) of the initial vortex seed. The atmospheric conditions include the temperature lapse rate (GAMMA), sea surface temperature (SST) and 500-hPa relative humidity (500-hPa RH). Vertical wind shear is an important factor to tropical cyclone development; however, we do not include it as a perturbation factor because it is coupled with temperature lapse rate (through thermal wind balance) and as such cannot be freely tuned. Consequently, no vertical wind shear

is present in the numerical simulations for this chapter. The work starts with the marginal and joint relationships between TC intensity and the five initial factors (RMW, MWS, SST, GAMMA, and 500-hPa RH). It then examines the interrelationships between TC relevant characteristics, for example, the intensity-precipitation relationship.

The remainder of this chapter is organized as follows. Section 3.2 introduces a schematic summary of the proposed idea. Section 3.3 describes the hurricane simulation using CAM, the algorithm used to extract physical fields from each tropical cyclone, the Latin Hypercube Sampling approach, the input parameters and their ranges, and the Expanded Multivariate Adaptive Regression Splines (EMARS) emulator approach. Section 3.4 analyzes the sensitivities of the final simulated characteristics of TCs to initial conditions, and assesses the interrelationship among the simulated TC characteristics. Section 3.5 compares the sensitivity of simulated TC intensity to the five initial factors in three typically used model resolutions. Section 3.6 gives discussion and limitation. Section 3.7 summarizes the main conclusions.

3.2. Schematic Summary

Essentially, the uncertainty quantification framework can be treated as a design for conducting numerical experiments so as to retrieve detailed information of interest to the community. For a given dynamical system, the user first selects a numerical model that can be used to realistically simulate the particular system. Then, the user chooses the atmospheric factors of interest as model inputs, and the targeted characteristics of the dynamical system as model output, and identifies the range of input factors. Figure 3.1 provides a schematic summary of how the methodology works. The first step is to apply the Latin hypercube sampling method to model input and obtain N number of samples. Typically, N should be larger than $50 \cdot m$, where m is

the number of model inputs. The numerical model is then run N times with the N sets of model inputs. In this way, we will obtain N model output vectors.

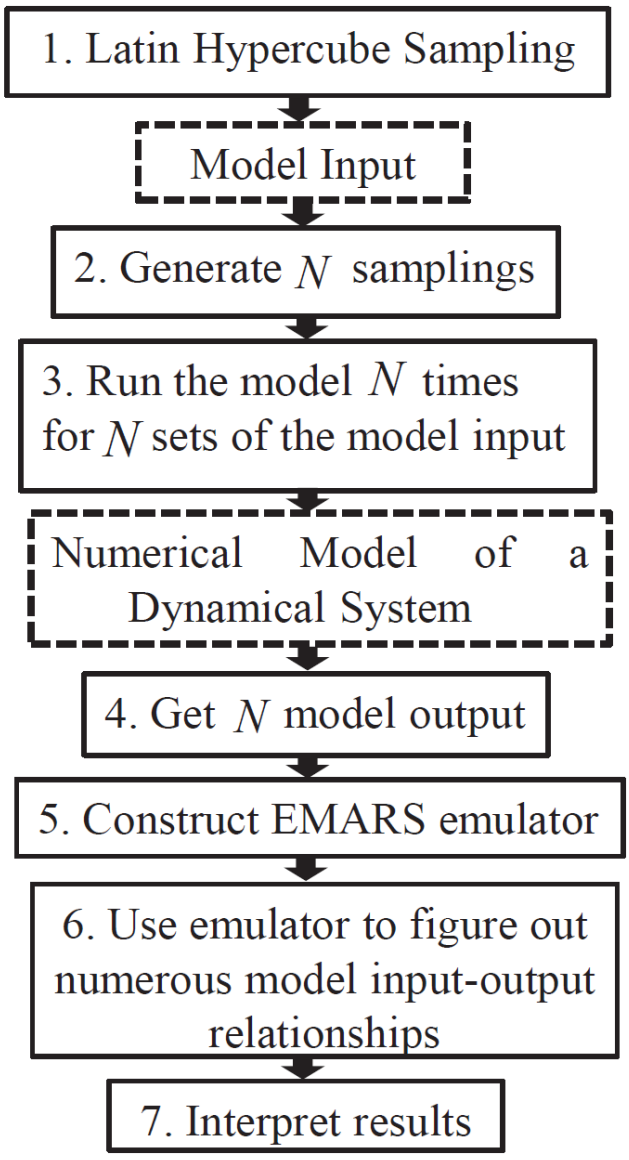

Figure 3.1: The schematic flow chart of implementing the proposed UQF on dynamical system in a step-by-step way.

Let $\vec{x} = (x_1, x_2, ..., x_m)$ denote the m model inputs. These could be sea surface temperature, relative humidity, wind speed, translational speed, atmospheric stability, etc, anything of interest to the targeted dynamical system. Then, let $\vec{y} = (y_1, y_2, ..., y_n)$ denote the characteristics of the dynamical system as model output. These could be size, intensity, precipitation, location and so on. Implementing these steps in practice requires us to first identify the range of $\vec{x}$, then use LHS to generate N samples of $\vec{x}$, which means $\vec{x}$ becomes $\begin{pmatrix} x_{11} & x_{21} & x_{31} & \cdots & x_{m1} \\ x_{12} & x_{22} & x_{32} & \cdots & x_{m2} \\ x_{13} & x_{23} & x_{33} & \cdots & x_{m3} \\ \cdots & \cdots & \cdots & \cdots & \cdots \\ x_{1N} & x_{2N} & x_{3N} & \cdots & x_{mN} \end{pmatrix}$. If we set the model input to the vector $(x_{11}, x_{21}, x_{31}, ..., x_{m1})$, and run the model, we will obtain the corresponding model output vector $\vec{y}_1 = (y_{11}, y_{21}, ..., y_{n1})$. Each row of the matrix $\vec{x}$ is a set of model inputs used to run the model, and will produce the corresponding vector of model output. N rows of matrix $\vec{x}$ correspond to N runs of the numerical model run, yielding N vectors of model output $\vec{y}$. That is to say, $\vec{y}$ also becomes a matrix $\begin{pmatrix} y_{11} & y_{21} & y_{31} & \cdots & y_{n1} \\ y_{12} & y_{22} & y_{32} & \cdots & y_{n2} \\ y_{13} & y_{23} & y_{33} & \cdots & y_{n3} \\ \cdots & \cdots & \cdots & \cdots & \cdots \\ y_{1N} & y_{2N} & y_{3N} & \cdots & y_{nN} \end{pmatrix}$.

The next step is to construct a statistical emulator from the matrices $\vec{x}$ and $\vec{y}$. The statistical emulator is also referred to as a surrogate model, among which are Multivariate Adaptive Regression Splines (MARS; Friedman et al., 1995), Multiple Additive Regression Trees (MART; Friedman, 1999; Friedman and Meulman, 2003), and Gaussian Spatial Process models (GaSP; Sacks et al, 1989; Craig et al., 2001). They are designed to fill the void between model output and input via curve fitting with splines (e.g., MARS and MART), or by interpolation (e.g.,

GaSP). The statistical emulator is used to establish a functional relationship between $\vec{y}$ and $\vec{x}$. This is, we use the samples in matrices $\vec{x}$ and $\vec{y}$ to construct: $y_1 = f_1(x_1, x_2, ..., x_m)$, $y_2 = f_2(x_1, x_2, ..., x_m), \ldots, y_n = f_n(x_1, x_2, ..., x_m)$.

Having defined a functional relationship that emulates the model input-output response, one can input other values of $(x_1^{new}, x_2^{new}, ..., x^{new}_m)$ to the emulator and obtain corresponding model output variables $(y^{new}_1, y^{new}_2, ..., y^{new}_n)$. As the statistical emulator is much more efficient than the numerical models, it allows us to compute numerous input-output pairs in a computationally affordable fashion. The following section provides documentation of how to apply the framework, and describes its utility for model evaluation.

3.3. Data and Methodology

3.3.1. Idealized tropical cyclone simulation

3.3.1.1 Model configuration

The idealized tropical cyclone test case was originally produced using the National Center for Atmospheric Research (NCAR)/Department of Energy (DOE) Community Atmosphere Model (CAM). Here, all our simulations are conducted using a newer version of the same model with horizontal resolution of $1.0^\circ \times 1.0^\circ$, $0.5^\circ \times 0.5^\circ$, and $0.25^\circ \times 0.25^\circ$. A 1.0°, 0.5°, and 0.25° latitudinal and longitudinal horizontal grid corresponds to a grid spacing of approximately 110 km, 55 km and 28 km in the equatorial region. The set of resolutions is chosen so as to match the typically used horizontal resolutions in the Coupled Model Intercomparison Project Phase 5 (CMIP5; Taylor et al., 2012) archive.

The CAM model is composed of two fundamental parts: the dynamical core and the physical parameterization packages. The finite volume dynamical core is the default in CAM 5.1.1, and

has been extensively evaluated alongside the CAM version 5.1.1 physical packages. We are aware that the spectral element (SE) is the new default dynamical core in the recently released CAM 5.3; however, unlike the FV option, the SE dynamical core has yet to be comprehensively scientifically validated with the CAM 5 physics packages. Figure 3.2 shows the flowchart of the tropical cyclone simulation. The model is fed with an idealized initial condition, which consists of a 3-dimensional (3D) weak vortex seed overlaid on horizontally homogeneous large-scale tropical environmental conditions. The background wind is set equal to zero. Based on predetermined pressure and specific humidity, the temperature and wind field of the initial vortex seed are derived from hydrostatic and gradient wind balance. The model surface is covered with a global ocean, and SST is set constant everywhere; this set up is commonly referred to as an aqua-planet. After the model integrates the initial data for 10 days, it produces a TC that ranges from a weak circulation to a well-developed storm (Reed and Jablonowski 2011a, b; 2012). For a detailed description of the idealized tropical cyclone simulation in CAM, the reader is referred to Reed and Jablonowski 2011a. In essence, this model configuration is constructed deliberately to favor TC development. All of the necessary ingredients are in place: organized vortex seed, high SST, no shear and favorable lapse rate. As we will show, this leads to the production of, on average, stronger TCs than are typically observed in the real world; however, the idealized environment is useful in that it allows a detailed examination of TC development that is unclouded by the influence of external sources of variability.

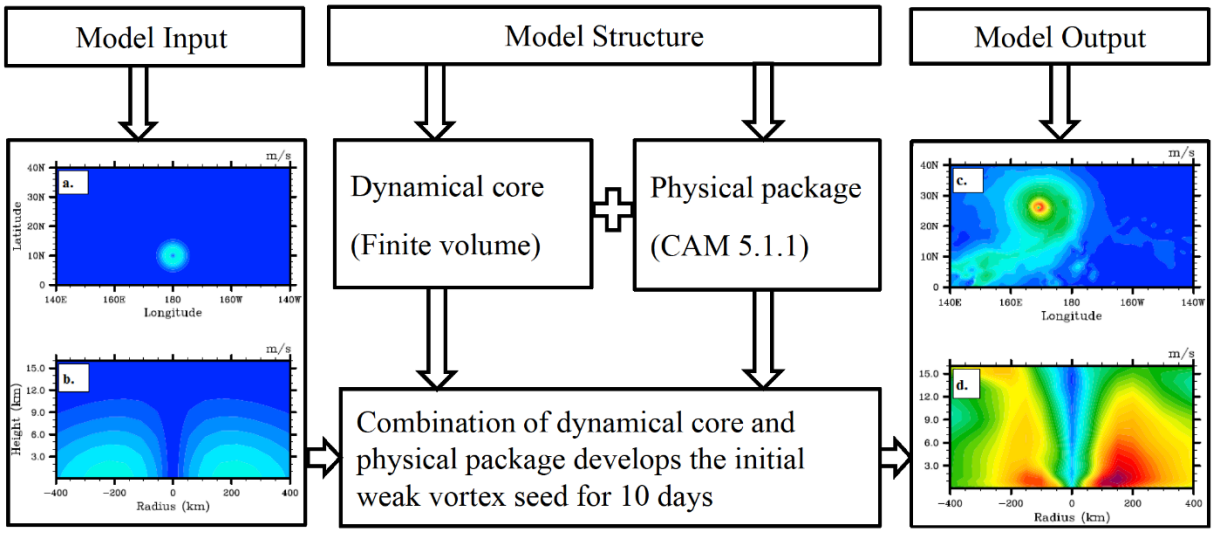

Figure 3.2: The flowchart of idealized tropical cyclone simulation in NCAR Community Atmospheric Model. (a) –(d): snapshots shows the evolution of tropical cyclone like vortex at days (a. b) 0, and (c. d) 10 at the resolution0.5°, L30. (a) and (c): Horizontal cross section of the wind speed at a height of 100 m. (b) and (d) Longitude-height cross section of the wind speed through the center of the vortex. (For details, the reader is referred to Figure 7, Reed and Jablonowski 2011a).

3.3.1.2. Algorithm used to extract physical fields from simulated tropical cyclones

The sensitivities of six TC-relevant output variables to the initial conditions are investigated. They are shown in Table 3.1: maximum wind speed (MWS; intensity; Vmax), total precipitation rate (PRECT), shortwave cloud radiative forcing (SWCF), longwave cloud radiative forcing (LWCF), cloud ice water path (IWP) and cloud liquid water path (LWP). The five physical variables are averaged over the tropical cyclone in the following manner: (1) Find the minimum surface pressure, which is defined to be the storm center; (2) search the tropical cyclone in a latitude/longitude region within plus and minus 20 degrees of the storm center; and (3) select the points that satisfy each of the following criteria: (a) wind speed at 100-m height above surface greater than 6 $m \cdot s^{-1}$, and (b) outgoing longwave radiation (OLR) less than 230 $W \cdot m^{-2}$. Figure 3.3 shows an example of the shortwave cloud radiative forcing before and after applying the TC

identification algorithm. The purpose of the algorithm is to filter out small grid-scale convection that is irrelevant to the tropical cyclone structure and development while preserving the TC-relevant fields. The first two thresholds locate the TC and its surrounding region, circumscribed in a square subdomain. The third threshold refines the specific shape of the TC, and ensures that the resulting fields accurately represent the TC. The threshold value used for wind speed and OLR is not absolute and other slightly higher or lower values could also be used to isolate the TC. We have tested a range of values and have determined that the conclusions derived from the analysis do not change. After selecting those points that span the TC, area-weighting for each variable calculation is conducted.

Variables	Description	Units
Intensity (MWS/Vmax)	Maximum wind speed of 100-m height above surface	$m \cdot s^{-1}$
PRECT	Total precipitation rate (large scale precipitation rate + convective precipitation rate)	$mm \cdot hr^{-1}$
SWCF	Shortwave cloud radiative forcing	$W \cdot m^{-2}$
LWCF	Longwave cloud radiative forcing	$W \cdot m^{-2}$
LWP	Cloud liquid water path	$g \cdot m^{-2}$
IWP	Cloud ice water path	$g \cdot m^{-2}$

Table 3.1: List of names for the TC-relevant output variables used in this paper (Vortex center is defined by the minimum surface pressure).

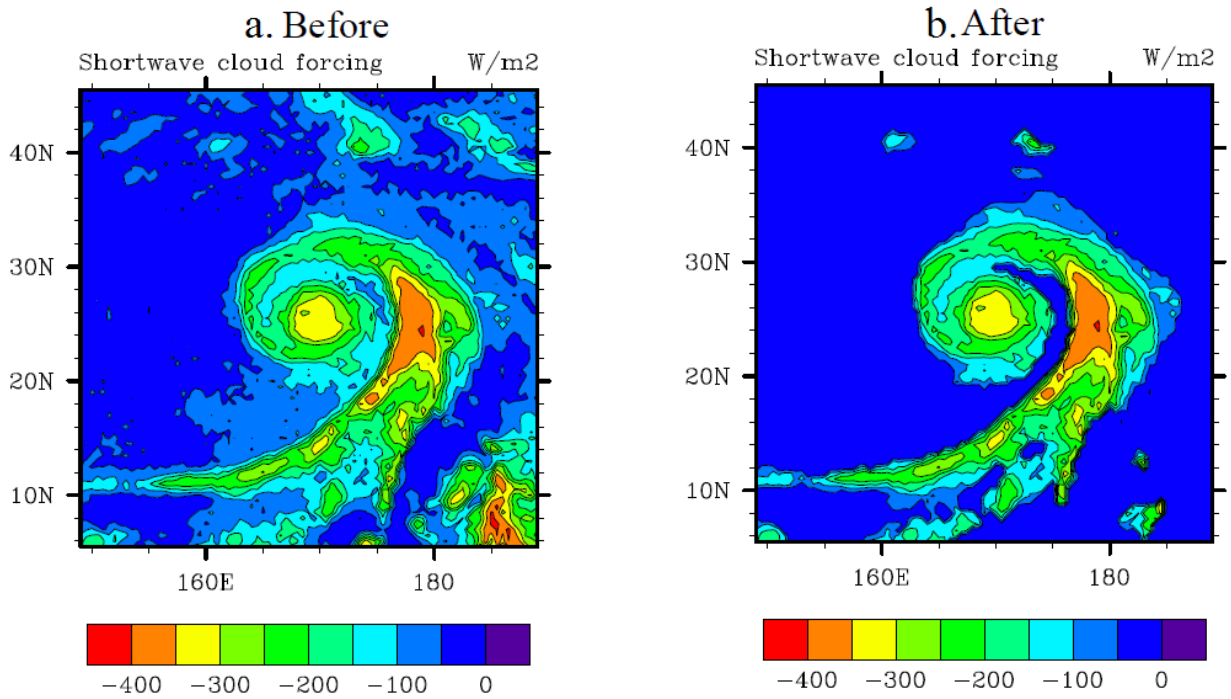

Figure 3.3: Example of the shortwave cloud radiative forcing (left) before applying the TC identification algorithm, and (right) after.

3.3.2. Uncertainty quantification framework

The term uncertainty quantification (UQ) has come to refer to a set of techniques now widely used to examine uncertainties in numerical models associated with initial conditions, model physics parameters, and construction (Stensrud et al. 2000; Murphy et al., 2004; van den Heever and Cotton 2004; Posselt and Vukicevic 2010; Collins et al., 2011; Berner et al. 2011; Posselt and Bishop 2012). In this chapter, it specifically indicates a combination of Latin Hypercube Sampling (LHS) with a surface response emulator. LHS is used to sample the points for the initial parameters, and the surface response emulator used in this chapter is the Expanded Multivariate Adaptive Regression Splines (EMARS).

3.3.2.1 Latin Hypercube Sampling

The Latin Hypercube Sampling (LHS) method is a component in the UQ process that generates a space-filling ensemble of samples. It is typically followed by the use of a response surface

emulator, e.g., MARS, MART, GaSP, polynomial chaos, etc, and works together with EMARS in our study. The LHS method seeks to accurately extract as much trend data from a parameter space as possible using a limited number of sample points. While the input parameter range is divided into equi-probable non-overlapping intervals, LHS requires that every row and column in the hypercube of partitions has exactly one sample, which provides improved coverage of the range of input variables, relative to traditional Monte Carlo sampling. For more information on the method, one is referred to the work of McKay, et al. (1979), Iman and Shortencarier (1984), and Helton and Davis (2000). We choose five input parameters for study and divide their range into 300 segments (Table 3.2). Note that while we perturb the 500 hPa relative humidity, the surface relative humidity is set to the same constant 83.6% for each individual simulation.

Parameter	Minimum	Maximum	Description (Units)
RMW	175	300	Radius of Maximum wind speed (km)
MWS	12.5	25	Maximum wind speed (m/s)
Gamma	5.5	7.5	Environmental temperature lapse rate (K/km)
SST	22.5	34.0	Sea surface temperature ($^{\circ}C$)
500-hPa RH	0.4	0.7	500-hPa Relative Humidity (unitless)

Table 3.2: Short Names, Minimum and Maximum Values, and Descriptions of the Five input parameters in the ensemble simulation with $0.5^{\circ} \times 0.5^{\circ}$ grid spacing.

3.3.2.2 Surrogate models: GaSP, MARS, EMARS

In the Gaussian spatial process (GaSP) surrogate model, the output is treated as a realiziation of a Gaussian stochastic process with mean functions and covariance matrix (Sacks et al 1989). Several unknowns are to be solved including the weight and parameterization of covariance matrix. The unknowns can be solved with the maximum likelihood estimate (MLE), where iterative algorithms are often used to solve MLE. In addition, the Bayesian version of GaSP is often used in surrogate model. In the Bayesian method, a group of prior parameters are set for the mean functions and covariance matrix. The Markov Chain Monte Carlro (MCMC) method can be used to estimate posterior parameters.

Multivariate adaptive regression splines (MARS) is a nonparametric regression method introduced by Friedman (1991). Unlike parametric linear regression methods, the MARS model can emulate non-linear regression surfaces by combining products of spline basis functions. However, the flexibility of the MARS model is limited as it does not allow quadratic or higher order components in the model building process. Expanded MARS (EMARS) is a flexible extension of the MARS method which allows higher order terms as required. The algorithm for Expanded MARS (EMARS) is:

1. For a multi-dimensional problem with n predictors ($x_1,...,x_n$), expand the predictor space from n to $L \times n$ by augmenting the original predictors with $\tilde{x} = (x_1,...,x_n; x_1^2,.....,x_n^2;...;x_1^L...x_n^L)$.

2. Fit the ordinary MARS model based on the expanded predictor space $\tilde{x}$. The ordinary MARS builds a model of the following form using n predictors ($x_1,...,x_n$):

$$\hat{f}(x_1,...x_n) = \alpha_0 + \sum_j \alpha_j B_j(x_1,...x_n)$$

Each B_j is either a hinge function $[x_i - u]_+$ or $[u - x_i]_+$, or the product of hinge functions such as $[x_i - u]_+[x_j - v]_+[x_k - w]_+$. The coefficients α are estimated using a least square criterion. The knots (the position of the hinge function: u, v, w) are determined with a greedy search algorithm using a least-squares update technique. In other words, EMARS uses the same building algorithms as MARS but with extended $L \times n$ predictors $(x_1,...,x_n; x_1^2,.....,x_n^2;...;x_1^L...x_n^L)$ while MARS utilizes only with n predictors ($x_1,...,x_n$). The validation of EMARS for this paper is illustrated in Appendix B.

3.4. Results from $0.5^\circ \times 0.5^\circ$ ensemble runs

3.4.1 Performance of three surrogate models

Variables	GaSP	MARS	EMARS
Intensity	0.05	0.04	0.04
PRECT	0.11	0.10	0.08
LWCF	0.03	0.02	0.03
SWCF	0.04	0.04	0.04
LWP	0.17	0.19	0.24
IWP	0.09	0.09	0.10

Table 3.3: NRMSE calculated from the three surrogate model (GaSP, MARS, EMARS) for (a). Intensity, (b). Total precipitation rate, (c).LWCF, (d). SWCF, (e) LWP and (f) IWP. For 300 samplings, a subset of the first 280 points are used to build the surrogate model and the last 20 points is used for training. The NRMSE is calculated from the 20 predicted points with their associated simulated points. GaSP: Gaussian Process Model, MARS: Multivariate Adaptive Regression Splines (MARS) , EMARS: Expanded Multivaraite Adaptive Regression Splines.

Table 3.3 compares how well the three surrogate models fit these six characteristics. GaSP, MARS and EMARS fit TC intensity, LWCF and SWCF well. The three surrogate models could fit TC PRECT and IWP, but have poor performance in fitting LWP. One reason might be that the surrogate model is a global fit, but if there are interactions that are small scale or very local they may not be fit well.

3.4.2 Input-output relationships

The sensitivity index is defined as the proportion of the increase in the residual sum of squares if the variable is fixed. Let $S1 = \sum_i (y_i - \hat{y}_i')^2$, $S2 = \sum_i (y_i - \hat{y}_i)^2$, then the sensitivity index SI is: $SI = (S1 - S2)/S2$, where, y is the sampled output simulated from numerical models, $\hat{y}'$ is the surrogate model fitted output when one selected input variable is fixed to constant, and $\hat{y}$ is the surrogate model fitted output with the original input variables from LHS. Sensitivity index is

used to quantify the relative importance of the five initial parameters to the six TC characteristics. The larger the sensitivity index, the more important the parameter is to the relevant TC characteristic. From each subplot, it is easy to distinguish the dominant factors (Figure 3.4). Fig. 3.4a shows that simulated TC intensity is most sensitive to the lapse rate and secondary to SST. The initial size and intensity of the vortex seed and RH 500 have only a minor influence on TC intensity. Precipitation rate is most sensitive to SST while LWCF is mainly affected by lapse rate and SST. The three dominant factors for SWCF are SST, MWS and lapse rate. LWP is most sensitive to lapse rate and IWP is most sensitive to SST.

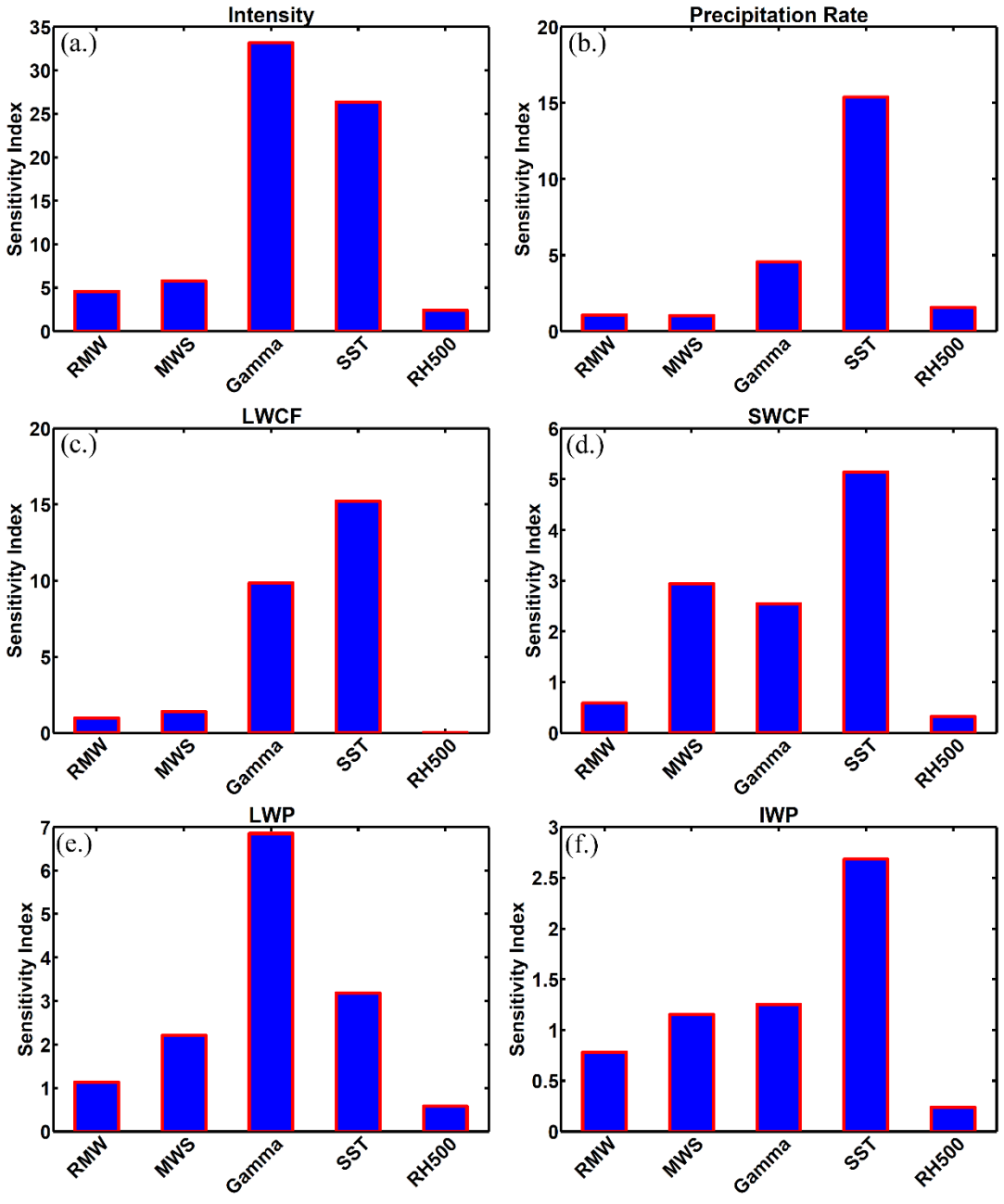

Figure 3.4: The sensitivity index (unitless) of the six final simulated output variables to the five initial parameters: (a). Intensity ($m \cdot s^{-1}$), (b). Precipitation rate ($mm \cdot hr^{-1}$), (c). LWCF ($W \cdot m^{-2}$), (d). SWCF ($W \cdot m^{-2}$), (e). LWP ($g \cdot m^{-2}$) and (f). IWP ($g \cdot m^{-2}$). Sensitivity index is the proportion of the increase in the residual sum of squares if the variable is fixed. It is a measure of importance of the variable. Higher values imply higher sensitivity of the variable.

3.4.2.1 Intensity

The effect of atmospheric conditions on tropical cyclone intensity change has been extensively studied using observational data and high resolution regional models. Even so, few studies have attempted to quantify the effect of an isolated factor on TC intensity with statistical robustness. It is difficult to isolate a single factor from observational analysis as our atmosphere changes its various conditions simultaneously. In addition, high resolution regional models are limited by computational constraints. With 300 simulations sampled by a statistical method such as LHS and the help of statistical emulator, we are able to statistically assess the relationship between TC intensity and a single factor, quantify its associated uncertainty and assess the changed TC intensity due to two simultaneously changing factors. Figure 3.5 illustrates this point using TC intensity. Fig. 3.5a assesses the relationship when TC intensity is affected only by the atmospheric lapse rate (Gamma), which means other four perturbed parameters (RMW, MWS, SST, 500-hPa RH) are fixed to median values. Fig. 3.5b is the same as Fig. 3.5a, but for the relationship between TC intensity and sea surface temperature. While it is well known that high atmospheric lapse rates (more unstable atmosphere) and high sea surface temperatures produce larger TC intensity, the specific relationship has not been quantified. Our results show that the TC intensity is linearly affected by atmospheric instability and sea surface temperature. Fig. 3.5c further shows that if these two factors vary simultaneously, they still have a linear influence on TC intensity change. Those results match the theory of Emanuel (1986) and high resolution simulations from Shen et al. (2000).

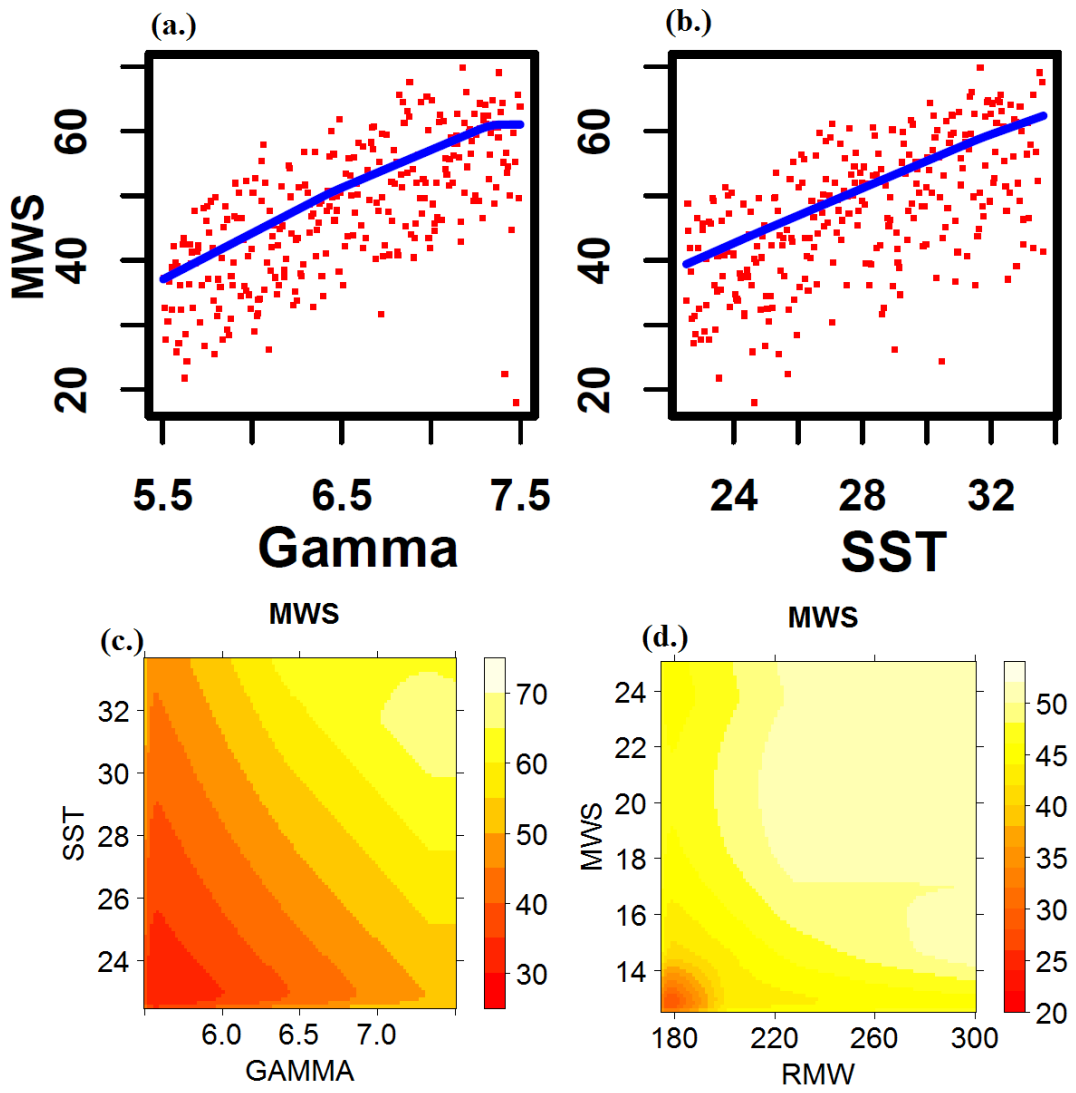

Figure 3.5:The relationship between final simulated TC intensity ($m \cdot s^{-1}$) and (a) the initial atmospheric lapse rate (Gamma; $K \cdot km^{-1}$), (b) the initial sea surface temperature (SST; $^{\circ}C$). Note, the blue solid line shows the relationship fitted by EMARS emulator. Other four perturbed parameters are fixed to median value when the relationship is quantified. The red points show the simulated TC intensity from the 300 samples. To interpret the red dot points, one may need to bear in mind that other four parameters are also changed. The relationship describes the final simulated TC intensity change to (c) simultaneous change of Gamma and SST, (d) simultaneous change of RMW and MWS.

It is worthwhile to note that the mid-level RH shows no effect on TC intensity change due to lack of vertical wind shear (Ge et al. 2013) and the aqua-planet set up (results not shown). The size and intensity of initial vortex seed (RMW and MWS) cause weak changes in TC intensity

throughout their pre-determined ranges. The TC intensity uncertainty is 5 $m \cdot s^{-1}$ when RMW changes from 175 km to 300 km. It is 8 $m \cdot s^{-1}$ when MWS changes from 12.5 $m \cdot s^{-1}$ to 25.0 $m \cdot s^{-1}$. Those results are not shown. While the isolating effect of RMW and MWS causes small changes in TC intensity, the interaction between RMW and MWS causes a much larger response. The latter is shown in Fig. 3.5d, in which it may be seen that the TC intensity changes from 20 $m \cdot s^{-1}$ to 55 $m \cdot s^{-1}$. The uncertainty range is 35 $m \cdot s^{-1}$, which is much larger than the 5 $m \cdot s^{-1}$ and 8 $m \cdot s^{-1}$ seen in individual perturbation experiments. This suggests that the combined effect of initial RMW and MWS is a very important "factor" for TC development and may lead to destructive TCs, even though the individual effect of changes to one or the other of them is small. This is not a result that has been well documented in the current literature. It is widely assumed that factors favoring TC genesis can be considered separately and are additive or multiplicative (Nolan and Rappin 2008). This assumption is fundamental to the genesis parameters of Gray (1968), DeMaria et al. (2001), and Emanuel and Nolan (2004), as well as statistical hurricane intensity forecast models such as SHIPS (DeMaria and Kaplan 1999). Genesis parameters and statistical predictions do not include the initial vortex characteristics. However, our results show that the combined effect is not negligible.

3.4.2.2 Shortwave cloud radiative forcing

Figure 3.6 quantifies the same types of relationship as Figure 3.5, however, for SWCF. Only the factors that have significant effect on TC-relevant SWCF are shown. As shown in Fig. 3.6a, 3.6b and 3.6c, the magnitude of SWCF is linearly affected by three factors: intensity of initial vortex seed (MWS), atmospheric lapse rate (Gamma) and sea surface temperature (SST). Larger magnitudes of SWCF (absolute value of SWCF) are associated with smaller initial MWS, a more stable atmosphere and larger SST. Compared to MWS and Gamma, SWCF tends to be more

sensitive to SST. The uncertainties of TC SWCF caused by the isolating the effect of three factors is 20 ~ 30 $W \cdot m^{-2}$ for MWS, Gamma and SST. This uncertainty is boosted by the combined effect of Gamma and SST as shown in Fig. 3.6d. The range is from -90 $W \cdot m^{-2}$ to 145 $W \cdot m^{-2}$ and the uncertainty is 55 $W \cdot m^{-2}$. It is worthwhile to note that changes in Gamma and SST on SWCF have the opposite effect on the SWCF change. This indicates that they can modulate the TC radiation effect, even when they produce the same TC intensity.

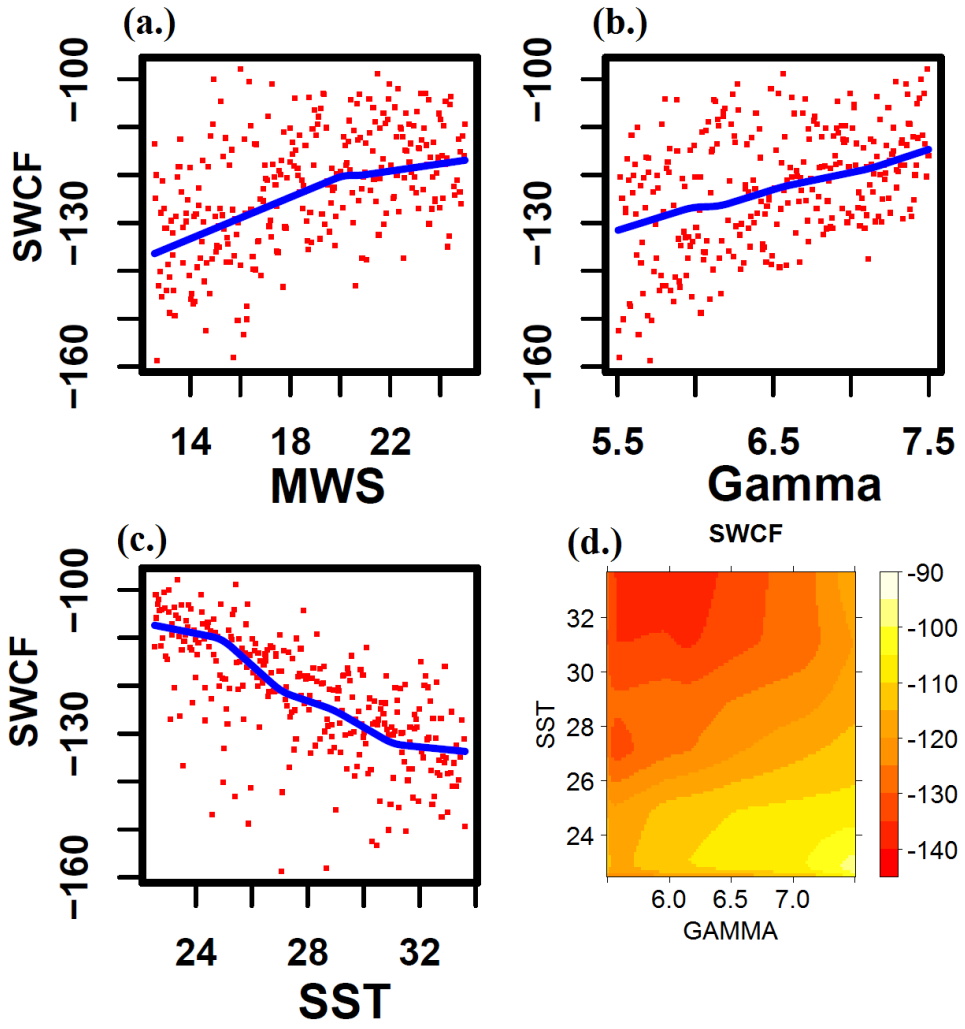

Figure 3.6: The relationship between final simulated TC SWCF ($W \cdot m^{-2}$) and (a) the intensity of initial vortex seed (MWS; $m \cdot s^{-1}$), (b) the initial atmospheric lapse rate (Gamma; $K \cdot km^{-1}$), (c) the initial sea surface temperature (SST; $^{\circ}C$). Note, the blue solid line shows the relationship fitted by EMARS emulator. Other four perturbed parameters are fixed to median value when this relationship is quantified. The red points show the simulated TC intensity from the 300 samples.

To interpret the red dot points, one may need to bear in mind that other four parameters are also changed. (d) the relationship describes the final simulated TC SWCF change to simultaneous changes of Gamma and SST.

3.4.2.3 Longwave cloud radiative forcing

In contrast to SWCF, the TC LWCF is mainly dependent on SST (Fig. 3.7b). The dependence is linear and can be quantified as ~2 $W \cdot m^{-2} \cdot K^{-1}$. Higher SST produces stronger storms and also larger vapor content in the atmosphere, both of which could increase high cloud and thus lead to higher LWCF. LWCF is weakly dependent on Gamma (Fig. 3.7a) and not sensitive to RMW, MWS and 500-hPa RH (not shown). The changes in LWCF caused by isolating the effect of Gamma and SST is 8 $W \cdot m^{-2}$ and 25 $W \cdot m^{-2}$, respectively. This response is also boosted to 40 $W \cdot m^{-2}$ by the combined effect of Gamma and SST as shown in Fig. 3.7c. The change of LWCF is from 65 $W \cdot m^{-2}$ to 105 $W \cdot m^{-2}$ while Gamma and SST simultaneously change throughout their predetermined ranges.

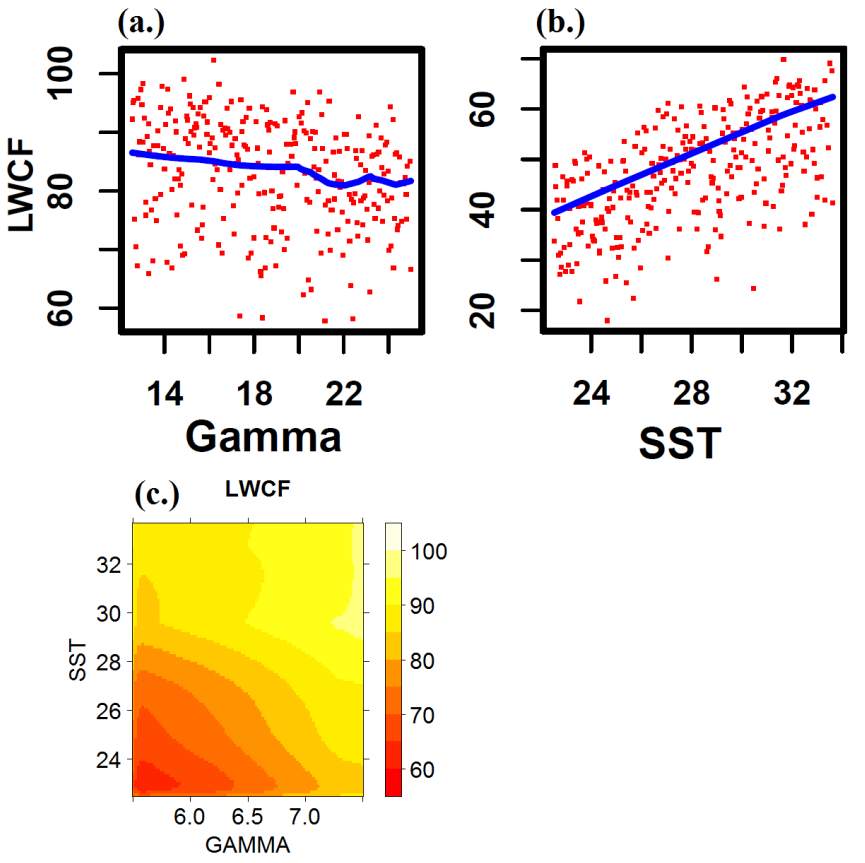

Figure 3.7: The same as Figure 3.5, however, for final simulated LWCF ($W \cdot m^{-2}$).

3.4.2.4 Cloud ice water path

The cloud ice water path is sensitive to the initial vortex characteristics and atmospheric thermodynamic conditions. IWP decreases linearly with increasing size (Fig. 3.8a) and intensity (Fig. 3.8b) of the initial vortex seed. It increases with increasing atmospheric lapse rate (Fig. 3.8c) and sea surface temperature (Fig. 3.8d). IWP is the only TC-relevant variable that shows strong sensitive to four initial parameters (RMW, MWS, Gamma, and SST). The uncertainties of IWP caused by RMW and MWS are both ~ 10 $g \cdot m^{-2}$. This is in contrast to the ~ 25 $g \cdot m^{-2}$ produced by the combined effect of changes to both of these two factors (Fig. 3.8e). The uncertainty

caused by Gamma is ~ 10 $g \cdot m^{-2}$ and ~ 20 $g \cdot m^{-2}$ by SST. The combined effect of Gamma and SST causes uncertainty of ~ 35 $g \cdot m^{-2}$ for IWP (Fig. 3.8f).

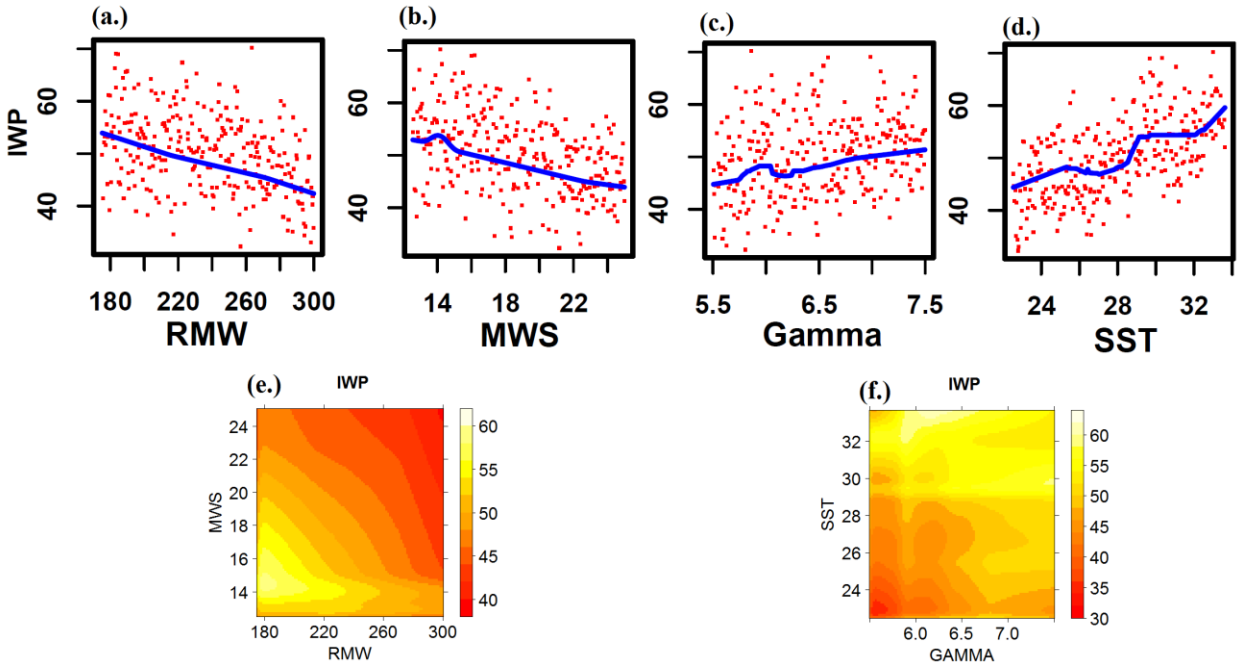

Figure 3.8: The relationship between final simulated TC IWP ($g \cdot m^{-2}$) and (a) the size of initial vortex seed (RMW; km), (b) the size of initial vortex seed (MWS; $m \cdot s^{-1}$), (c) the initial atmospheric lapse rate (Gamma; $K \cdot km^{-1}$), (d) the initial sea surface temperature (SST; $^{\circ}C$). Note, the blue solid line shows the relationship fitted by EMARS emulator. Other four perturbed parameters are fixed to median value when this relationship is quantified. The red points show the simulated TC intensity from the 300 samples. To interpret the red dot points, one may need to bear in mind that other four parameters are also changed. (e) the relationship describes the final simulated TC IWP change to simultaneous changes of RMW and MWS. (f) the relationship describes the final simulated TC IWP change to simultaneous changes of Gamma and SST.

3.*4.2.5 Cloud liquid water path*

LWP bears an inverse relationship with atmospheric lapse rate (Fig. 3.9a). LWP decreases if Gamma increases. In contrast, LWP increases with increasing SST (Fig. 3.9b). LWP is more sensitive to atmospheric lapse rate than SST. The corresponding uncertainty caused by Gamma is ~ 60 $g \cdot m^{-2}$ while it is ~ 30 $g \cdot m^{-2}$ for SST. This uncertainty is also augmented by the combined

effect of these two (Fig. 3.9c). It is ~ 85 $g \cdot m^{-2}$ when the Gamma and SST change simultaneously.

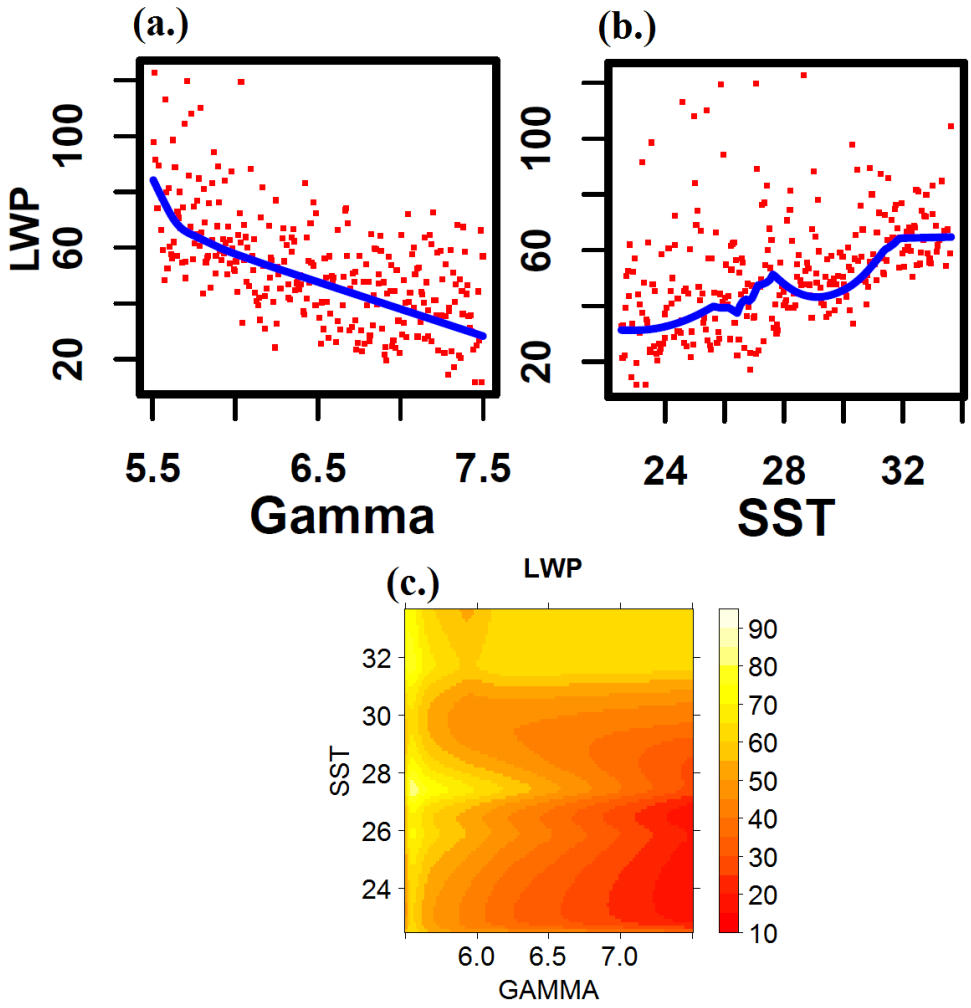

Figure 3.9: The same as Figure 3.5, however, for final simulated LWP ($g \cdot m^{-2}$).

3.4.2.6 Total precipitation rate

The relationships between TC total precipitation rate and the isolated effect of Gamma and SST is complicated. For Gamma in the range between 5.5 $K \cdot km^{-1}$ and 6.5 $K \cdot km^{-1}$, the total precipitation rate decreases with increasing Gamma (Fig. 3.10a). After the atmosphere reaches approximate moist instability (6.5 $K \cdot km^{-1}$), the cyclone mean precipitation does not change.

The precipitation rate is more sensitive to SST than Gamma (Fig. 3.10b). Precipitation dependence on SST can be divided into three phases: for SST smaller than $25^{\circ}C$, rain rate quickly rises with increasing SST; at SST values between $25^{\circ}C$ and $32^{\circ}C$, precipitation rate slowly increases with SST; and after the SST reaches $32^{\circ}C$, precipitation increases strongly with SST once again. Because of the contrary effect of Gamma and SST on total precipitation rate, there are two regions with the highest precipitation rate: moderate SST with low lapse rate, and highest SST with highest lapse rate (Fig. 3.10c).

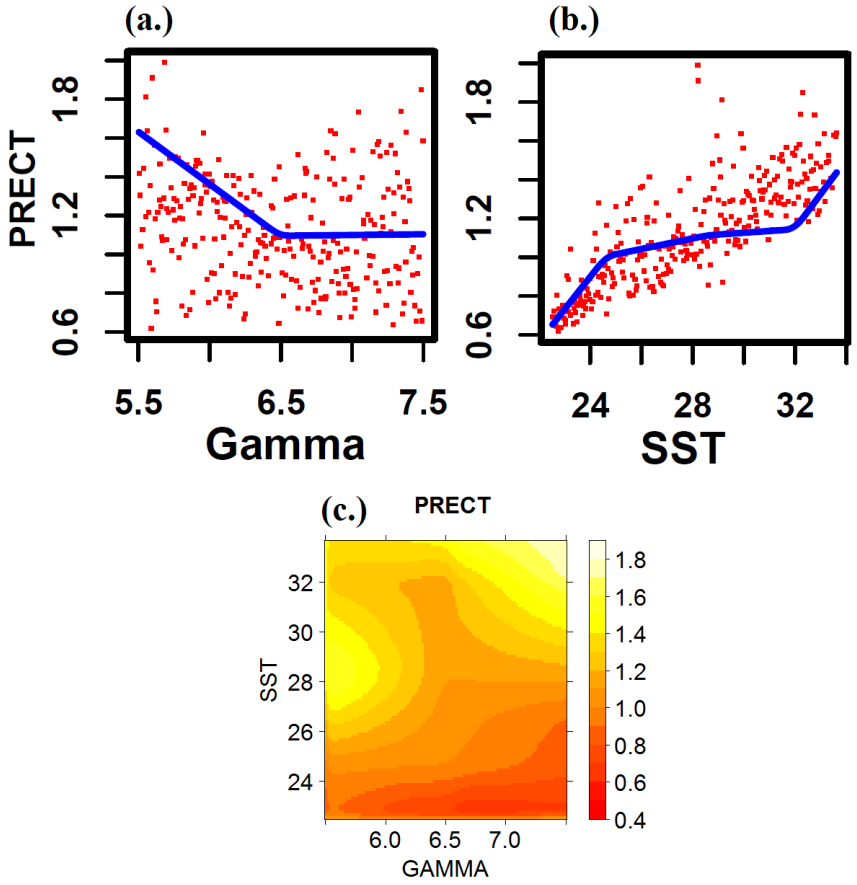

Figure 3.10: The same as Figure 3.5, however, for final simulated PRECT ($mm \cdot hr^{-1}$).

3.4.3 Output-output relationship: among the TC-relevant characteristics

3.4.3.1 Relationship between intensity and other five TC-relevant characteristics

TC cloud IWP and LWP are independent of TC intensity (not shown), while LWCF exhibits a linear relationship with TC intensity (Fig. 3.11a). Larger TC intensity tends to follow larger TC LWCF. In contrast, TC SWCF is independent with TC intensity (Fig. 3.11b). When TC intensity increases, the TC SWCF shows little change. It is well known that LWCF causes a warming effect while SWCF causes a cooling effect at the Earth's surface. The TC SWCF tends to dominate the TC LWCF and causes net negative cloud radiative forcing as shown in Fig. 3.11a and Fig. 3.11b, which suggest that more intense TCs tend to reduce the cooling effect (more warming effect contributed by LWCF while SWCF stays similar). Studies (Bengtsson et al. 2007b) show that more intense TCs will occur under climate warming using global climate models. Combined with the findings presented here, it may suggest a positive feedback between TC change and global surface temperature change represented in the AGCM simulations. The relationship between TC intensity and precipitation rate is interesting (Fig. 3.11c). For TC intensity below 50 $m \cdot s^{-1}$, the TC precipitation rate is independent on TC intensity. For TC intensity larger than 50 $m \cdot s^{-1}$, it shows a linear relationship between TC intensity: larger precipitation rate occurs with larger TC intensity.

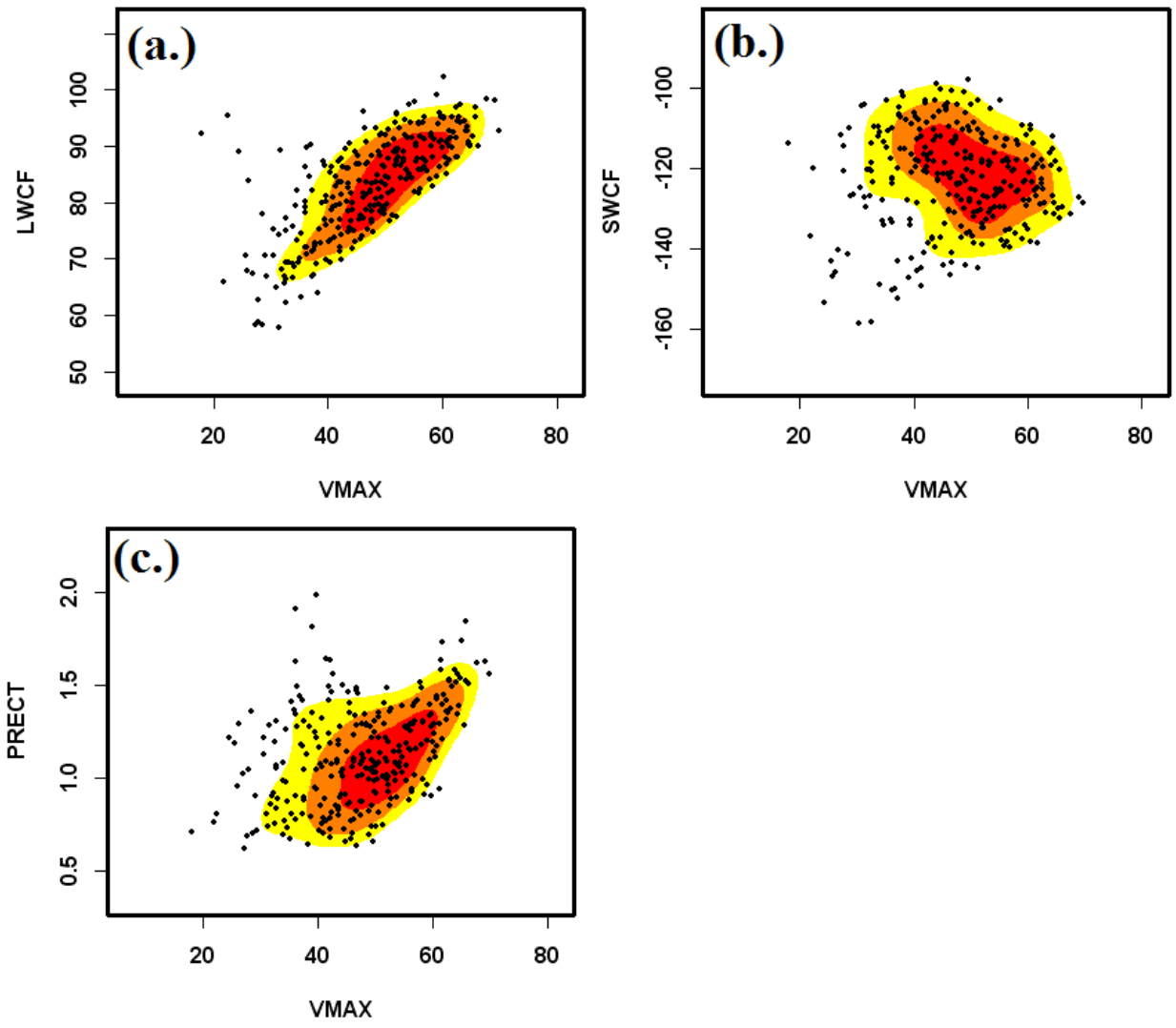

Figure 3.11: Univariate probability density function (PDF) of TC intensity and (a) LWCF, $W \cdot m^{-2}$ (b) SWCF, $W \cdot m^{-2}$ (c) PRECT, $mm \cdot hr^{-1}$. The colored contours contains the probability mass: red = 25%, orange + red = 50%, yellow + orange + red = 75%. The TC intensity, LWCF, SWCF and PRECT are final simulated output over days 9-10.

3.4.3.2 Relationships on TC precipitation rate

The relationship between TC precipitation rate and intensity is quantified in previous section (Fig. 3.11c). The precipitation rate is independent with IWP and LWCF (not shown). The precipitation rate is strongly correlated with LWP. Fig. 3.12b shows a linear relationship between the two. TC precipitation rate increases with TC LWP. This indicates that the initiation

mechanism of rain from droplet growth by collision and coalescence works efficiently in AGCMs. The magnitude of SWCF linearly increases with increasing precipitation rate (Fig. 3.12b). This may be due to the fact that high precipitation rates are associated with deep clouds, which have a larger cloud albedo.

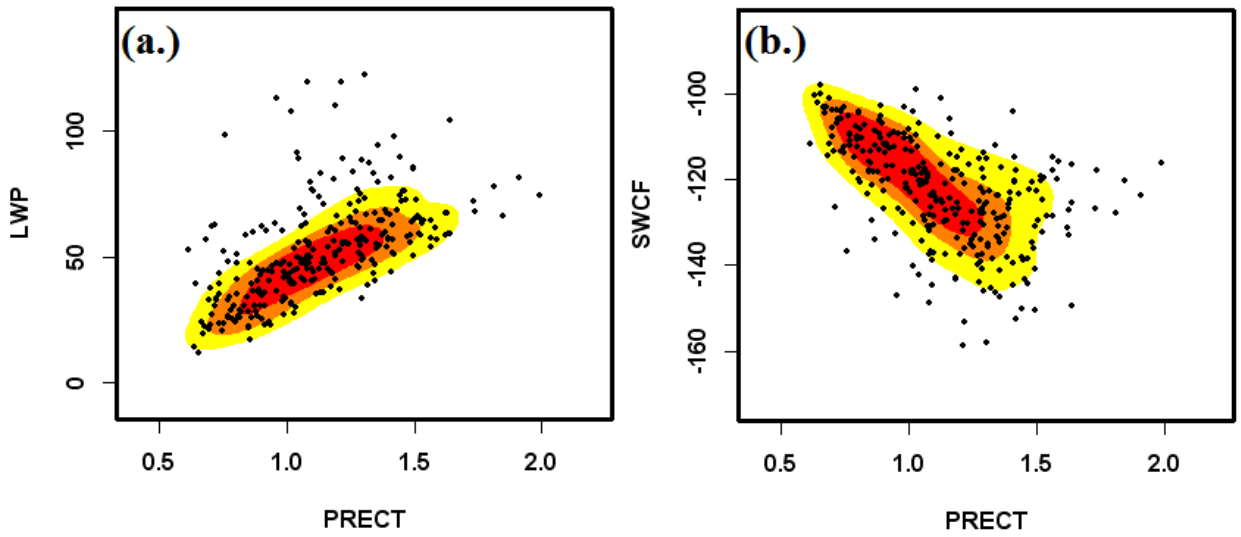

Figure 3.12: Univariate probability density function (PDF) of PRECT ($mm \cdot hr^{-1}$) and (a) LWP ($g \cdot m^{-2}$) (b) SWCF ($W \cdot m^{-2}$). The colored contours contains the probability mass: red = 25%, orange + red = 50%, yellow + orange + red = 75%. The PRECT, LWP and SWCF are final simulated output over days 9-10.

3.4.3.3 Relationships on SWCF, LWCF, LWP and IWP

TC SWCF and LWCF are nearly independent of each other (not shown). SWCF is linearly correlated with LWP (Fig. 3.13a). Larger magnitude SWCF follows from larger LWP. SWCF is also positively correlated with IWP (Fig. 3.13b). Larger IWP is associated with larger magnitudes of SWCF. LWCF is independent with LWP (not shown), but it maintains a positive linear relationship with IWP (Fig. 3.13c). Larger IWP is associated with larger LWCF, while LWP is independent of IWP (Fig. 3.13d).

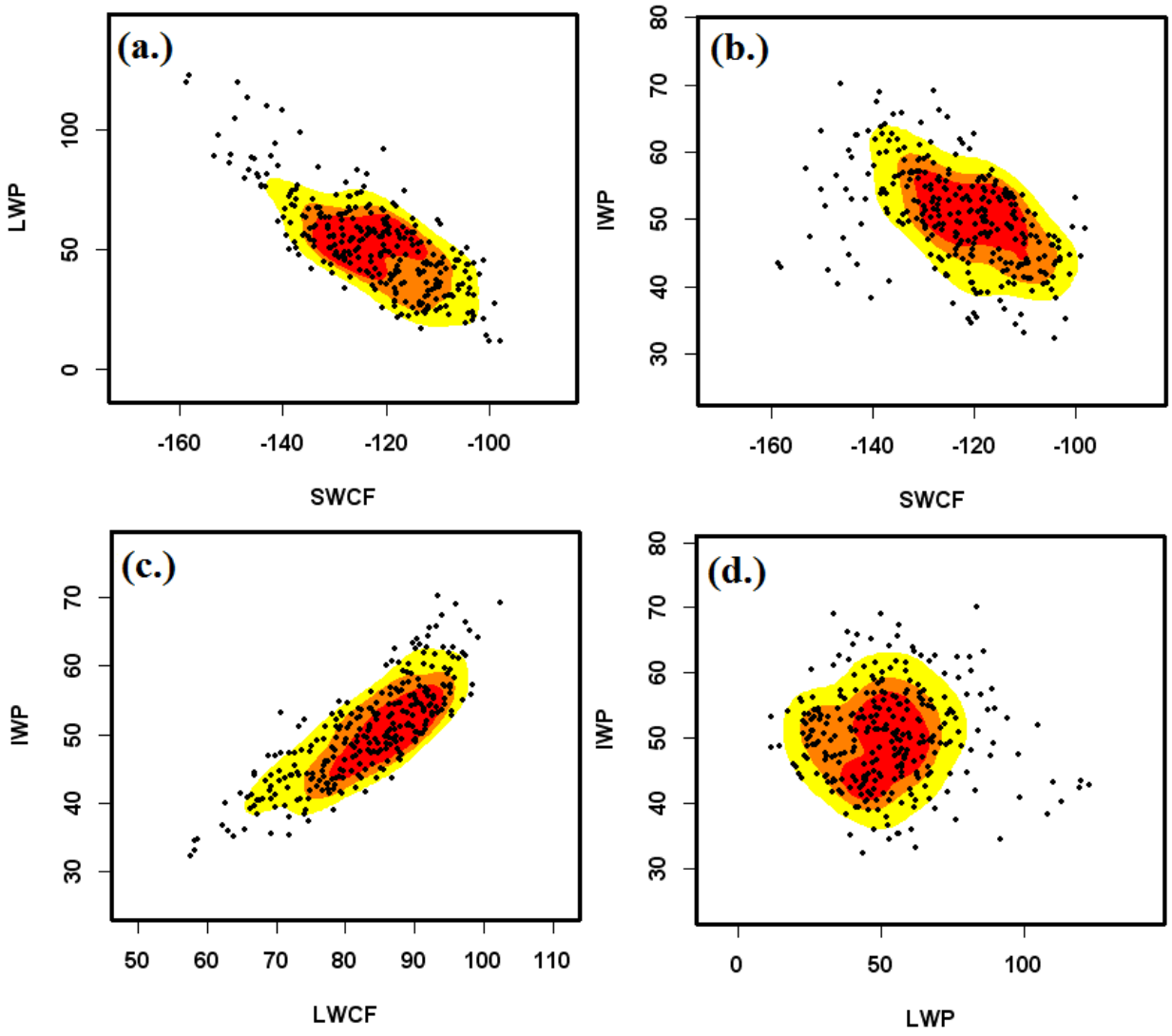

Figure 3.13: Univariate probability density function (PDF) of (a) SWCF ($W \cdot m^{-2}$) and LWP ($g \cdot m^{-2}$) (b) SWCF ($W \cdot m^{-2}$) and IWP ($g \cdot m^{-2}$) (c) LWCF ($W \cdot m^{-2}$) and IWP ($g \cdot m^{-2}$) (d) LWP ($g \cdot m^{-2}$) and IWP ($g \cdot m^{-2}$). The colored contours contains the probability mass: red = 25%, orange + red = 50%, yellow + orange + red = 75%. The SWCF, LWP, IWP and LWP are final simulated output over days 9-10.

3.5. Marginal sensitivity of intensity to five initial conditions in three horizontal resolutions

The sensitivity of simulated TC characteristics to changes in atmospheric environmental factors in the Community Atmosphere Model enables us to see how well the design of global climate models captures dynamical mechanisms in tropical cyclones. In the previous section, we have

shown how to use a UQF to characterize relationships between simulated TC characteristics and atmospheric control factors, which allowed us to interpret the representation of TC dynamical mechanisms in CAM when run at a resolution $0.5^\circ \times 0.5^\circ$. Here, we will compare the sensitivity of simulated TC intensity to the specified five initial conditions for different model resolutions: $1.0^\circ \times 1.0^\circ$, $0.5^\circ \times 0.5^\circ$, and $0.25^\circ \times 0.25^\circ$, which are the three horizontal resolutions most commonly used in full AGCMs for TC simulations.

Figure 3.14 shows that the simulated TC intensity to the five initial conditions are different in the three model resolutions. In simulations run on a $1.0^\circ \times 1.0^\circ$ grid, the simulated TC intensity shows considerable sensitivity to the initial size of the vortex seed; however, this sensitivity is very weak for model resolutions of $0.5^\circ \times 0.5^\circ$ and $0.25^\circ \times 0.25^\circ$ (Fig. 3.14a). The initial intensity of the vortex seed also tends to have a larger influence on the final TC intensity in coarser resolution runs (Fig. 3.14b). At $1.0^\circ \times 1.0^\circ$ resolution, the final TC intensity shows a much weaker dependence on SST and Gamma than in resolution of $0.5^\circ \times 0.5^\circ$ and $0.25^\circ \times 0.25^\circ$. Note that the sensitivities in the two finer resolutions are quite similar. This indicates that the ability of $0.5^\circ \times 0.5^\circ$ and $0.25^\circ \times 0.25^\circ$ to capture the basic dynamics for the development of TCs in CAM is similar. The improved performance of CAM with model resolution $0.25^\circ \times 0.25^\circ$ to simulate TC statistics is mainly coming from the improved performance of physical processes in finer resolution. In all the three resolutions, the simulated TC intensity shows little sensitivity to mid-level relative humidity (Fig. 3.14e). Fig. 3.14 clearly shows that model resolution of $1.0^\circ \times 1.0^\circ$ tends to have strong dependence on the initial size and intensity of the vortex seed, and it is far less sensitive to changes in SST and Gamma. The NCAR CAM 5.0 model with resolution of $1.0^\circ \times 1.0^\circ$ was only able to capture 9 tropical cyclones globally (Walsh et al. 2015) and could not capture strong tropical cyclones like Cat 4 or 5 on the Saffir-Simpson hurricane scale. But

Wehner et al. (2014) shown the high-resolution ($0.25^\circ \times 0.25^\circ$) configuration of NCAR CAM version 5.1 simulates much more realistic global number of tropical cyclones and can produce tropical cyclones up to Cat-5. Bacmeister et al. (2014) also showed that the high resolution ($0.23^\circ \times 0.31^\circ$) of CAM 5 could simulate realistic tropical cyclone distributions and reproduce the interannual variability in TC statistics. Our results suggest that, when run with relatively coarse resolution of $1.0^\circ \times 1.0^\circ$, the NCAR CAM cannot simulate TCs well, and that this may be due to the fact that it could not simulate the response to the SST and Gamma in a reasonable way.

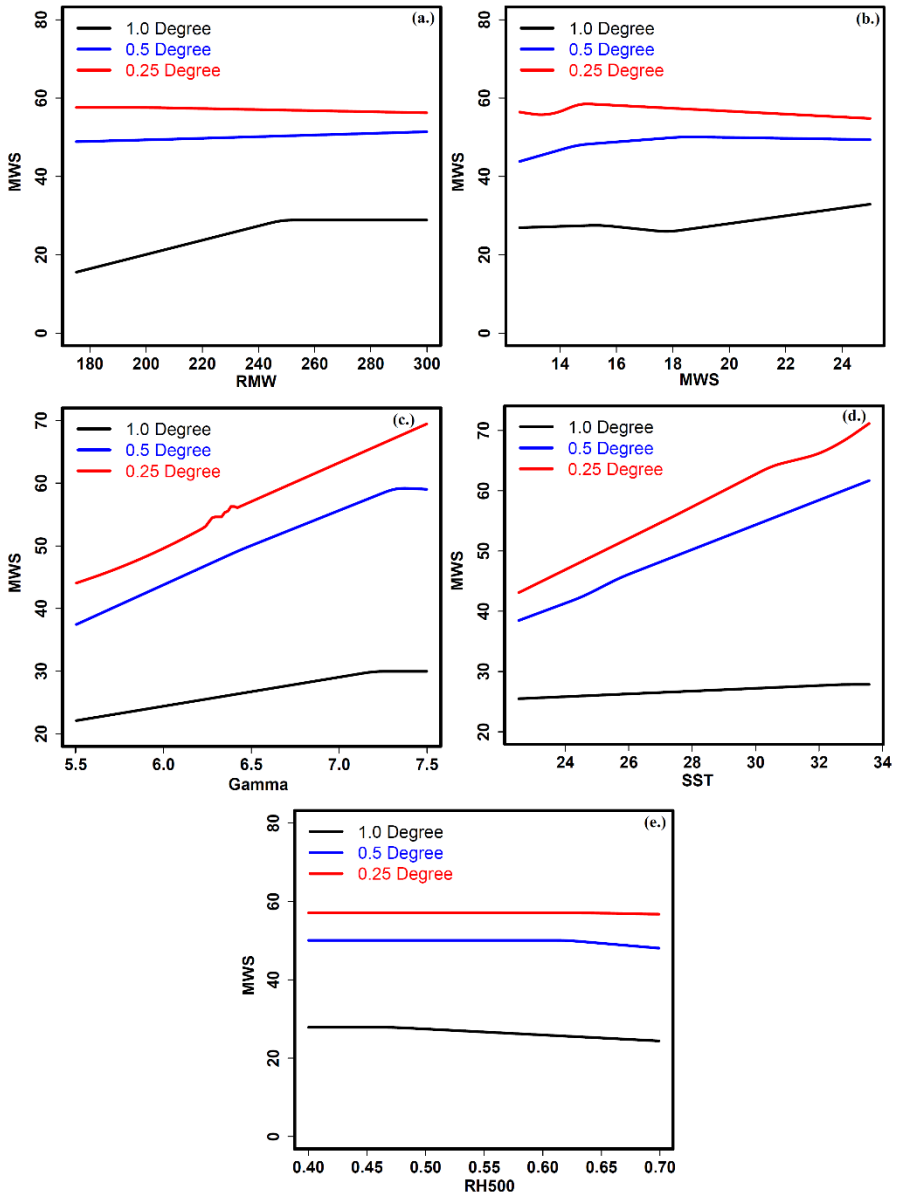

Figure 3.14: Marginal relationship between final simulated TC intensity (MWS; $m \cdot s^{-1}$) and the five input parameters for the three model resolutions. (a.) RMW (km): initial size of vortex seed, (b). MWS ($m \cdot s^{-1}$): initial intensity of vortex seed, (c.) Gamma ($K \cdot km^{-1}$): vertical lapse rate, (d.) SST ($^{\circ}C$) : sea surface temperature, and (e.) RH-500: mid-level relative humidity. Black line denotes the results computed from ensemble run with model resolution of $1.0^{\circ} \times 1.0^{\circ}$. Blue line denotes the results computed from ensemble run with model resolution of $0.5^{\circ} \times 0.5^{\circ}$. Red line denotes the results computed from ensemble run with model resolution of $0.25^{\circ} \times 0.25^{\circ}$.

3.6. Discussion and limitation

This work proposes a UQF designed to study the response of individual dynamical systems to changes in multivariate parameters. It provides a specific example of the use of LHS and an EMARS emulator for sensitivity assessment in AGCM-simulated TCs. The UQF could easily be extended to other dynamical systems, such as extratropical cyclones, non-TC tropical convective systems and so on. It also has the potential to quantify uncertainties associated with variability in model internal parameters in physical parameterization schemes, such as cloud, precipitation, and turbulence, which are key components in climate model representation of small scale processes.

It is worthwhile to note that the examined sensitivities of AGCM-simulated TC characteristics to the five chosen initial conditions are not intended to map to reality. While our results provide a realistic depiction of the known sensitivity of TCs to changes in SST and lapse rate, our goal is not primarily to understand how TCs function. Such a study requires a simulation framework that accounts for additional known factors that influence the development of TCs (e.g., vertical wind shear, characteristics of individual convective updrafts, ocean mixing, etc). Rather, we use the idealized model setup to obtain insight into sensitivities of TCs simulated in AGCMs, which include a multitude of interrelated and complex factors. Indeed, the lack of vertical wind shear in our idealized configuration enables us to focus on the response of the dynamical system to environmental factors like SST, Gamma and so on. Incorporation of vertical wind shear into the framework will require the adjustment of vertical temperature and thus lapse rate based on thermal wind balance. This is not an insurmountable challenge, but is one that we leave for future work.

3.7. Summary

In the case study based sensitivity analysis, we find that: (1) environmental lapse rate and sea surface temperature linearly affect the growth of TCs. (2) The TC total precipitation rate, cloud radiative forcing and cloud water content are all sensitive to the size and intensity of the initial vortex seed, the environmental lapse rate, and sea surface temperature, but have weak or no sensitivity to the initial 500-hPa relative humidity. (3) Changes in TC initial conditions interact nonlinearly to affect the final simulated characteristics of the TCs, in addition to from the linear relationships mentioned in (1). (4) Inter-relationships among TC relevant characteristics exist; specifically stronger TCs tend to be associated with larger LWCF and larger total precipitation rate tends to be associated with larger values of SWCF and larger cloud LWP. (5) The sensitivities of simulated TC intensity to the five initial conditions will change for different model resolutions.

We have shown that the UQF can be applied to the study of a particular dynamical system and yields tremendous information on the sensitivity of the system and its interaction with environmental factors. It allows the model input to vary simultaneously and thus can be used to examine the interactive effect among different parameters on simulated model output. Latin Hypercube Sampling is used to generate an ensemble of model simulations, and allows for simultaneous perturbation of the input parameters. Surrogate models could be used for approximating the numerical simulations and much more computationally efficient.

CHAPTER 4

Impact of Parameterized Physical Processes on Simulated Tropical Cyclone Characteristics in the Community Atmosphere Model

4.1. Introduction

Since Manabe et al. (1970) first identified a tropical cyclone like vortex in a global climate model, Atmospheric General Circulation Models (AGCMs) have been increasingly used to simulate tropical cyclones (TCs) in the current climate state, and predict their changes under future climate scenarios (Bengtsson et al. 1982; Krishnamurti et al. 1989; Broccoli and Manabe 1990; Wu and Lau 1992; Haarsma et al. 1992; Bengtsson 1995; Bengtsson et al. 2007b; Zhao et al. 2009; Zhao and Held 2010, 2012; Murakami et al. 2013; Zarzycki et al. 2014; Walsh et al. 2015). While most previous studies focus on the statistics of simulated TCs such as global (or basin wide) genesis density, track distribution, frequency, interannual variability and so on, attention in recent decades has been placed on simulating and forecasting the properties (e.g., track, life cycle, intensity) of specific tropical cyclones in global climate models. For example, Shen et al. (2006) used a global mesoscale-resolving model to study simulations of Hurricane Katrina (2005). Zarzycki and Jablonowski (2015) successfully forecast the recurvature of Hurricane Sandy into the northeastern United States 60 hours earlier than the Global Forecast System (GFS) model. Xiang et al. (2015) also studied the prediction of Hurricane Sandy and Super Typhoon Haiyan in the Geophysical Fluid Dynamics Laboratory (GFDL) coupled model,

and they indicated the potential for extended-range predictions of TCs. These results, and the rapid advancement of computational resources and numerical algorithms, suggest a possible growing trend in the use of global climate models for simulating and forecasting specific hurricanes in the next few decades, like what extratropical cyclone is today (Jung et al. 2006; Zheng et al. 2013).

A detailed understanding of how the choice of model components (e.g. grid resolution, physical parameterization, dynamical core, etc.) of AGCMs affect simulated tropical cyclone characteristics would foster the advancement of such realistic TC simulation and prediction. However, systematic examination of model sensitivity to changes in model components would require thousands of simulations. Due to the inherent complexity of model construction and the coexistence of various climate and weather systems in model output, using a full model to compute sensitivity is not feasible. Moreover, the compensating and interactive effect among various components in global climate models makes it difficult to study the effect of an isolated factor on targeted objects. The Reed-Jablonowski TC test case (Reed and Jablonowski 2011a) is specifically designed for this purpose and has the advantage of quickly identifying the key factors from the model constructions and ruling out those factors that exert little influence on simulated TCs. Moreover, use of a system in which there exists only a single TC allows us to isolate storm sensitivity to parameters from changes in the environment or the influence of the surface or other dynamical systems. Reed and Jablonowski (2011a, 2011b, 2011c and 2012) have successfully used this case to reveal the impact of grid resolution, dynamical cores and physical parameterization packages on the development of tropical cyclones. However, the impact of detailed parameterized physical processes within the physical schemes on simulated TC characteristics remains unclear.

The inherently multi-scale nature of TCs, and the necessity to parameterize most key TC processes (e.g. convection, cloud formation and precipitation), indicate that the development of TCs in AGCMs is likely sensitive to the details of the physical parameterizations that govern clouds, convection, turbulence, etc. TCs are inherently multiscale systems, with key processes that range from microscale to synoptic, including individual convective updrafts, cloud microphysics, precipitation, turbulent mixing, surface momentum transfer, etc. (Emanuel 1986; Rotunno and Emanuel 1987; Houze 2014). The representation of these processes in numerical models plays an important role in accurately simulating the various aspects of tropical cyclones including cyclogenesis, intensification, track, structure, intensity, rainfall, cloud distribution, etc. (Chan 1984; Lord et al. 1984; McFarqauhar and Black 2004; Fovell et al. 2009; Torn and Davis 2012; Bassill 2014; Goswami and Mohapatra 2014; Sanger et al. 2014; Sun et al. 2014; Wang 2014). Computational considerations (e.g., global domain and long integration times) require AGCMs to be run on grids that are too coarse to explicitly represent moist convective processes that govern TC evolution. The effects of subgrid-scale processes on the grid box-mean state are represented via *parameterization* (Jakob and Miller 2003; Stensrud 2007), which relates the aggregate effects of small scale processes to grid-scale model state variables. It means that that only simplified physical processes are retained in AGCMs.

Furthermore, recent studies that mainly focus on the simulated or predicted statistics of TCs (Murakami et al. 2012; Zhao et al. 2012; Kim et al. 2012; Zadra et al. 2014; Lim et al. 2015) in a global climate model confirm the importance of the individual parameterized physical process on TC simulation in global climate models. For example, Zhao et al. (2012) shows that the simulated global number of TCs exhibits nonintuitive response to incremental changes of the horizontal cumulus mixing rate. The inherent nature of TCs, the parameterization technique and

previous literatures all suggest the necessity to study the impact of numerous parameterized physical process on the development of a single tropical cyclone-like vortex in global climate models, which is the goal of this study.

In addition to the TC intensity, we are also interested in the impact of numerous parameterized physical processes on simulated TC precipitation rate, longwave cloud radiative forcing (LWCF), shortwave cloud radiative forcing (SWCF), cloud liquid water path (LWP) and ice water path (IWP). The additional five physical characteristics are selected for two reasons: (1) they directly govern the properties of clouds and precipitation that are not explicitly resolved and rely on parameterization techniques; (2) cloud and precipitation are essential components in a single TC system. The full set of Community Atmosphere Model (CAM) physical parameterizations are used so that the results are applicable to the Community Earth System Model (CESM) model. We will examine the impact of various parameterized processes across the majority of physical parameterization schemes in an AGCM, including representations of shallow convection, deep convection, moist turbulence, cloud microphysics, cloud macrophysics and aerosol effect on TC simulations.

In summary, our goal is to examine the impact of various parameterized physical processes on the simulated TC characteristics during the evolution from an initial vortex seed to a mature tropical cyclone like vortex in AGCMs. Specifically, we would like to (1) identify the key physical parameters to the six different TC characteristics and rule out the minor parameters; (2) assess the functional form of the parameter-state dependence; (3) investigate the interactive effect among the key physical parameters on simulated tropical cyclones; and (4) compare the parameter uncertainty with other sources of model uncertainty, such as model initial conditions and changes in model structure. This study contributes to a better understanding of how the

design of the physical parameterization affects a specific dynamical system. It could help to instruct the simulation and short term prediction of a particular TC in AGCMs. Beyond that, our results will have implications for the study of TC statistics in global climate models. Recent studies have confirmed the importance of physical parameters on the simulation and prediction of TC statistics in AGCMs, however, they only examined one or two parameters. They do not extend similar examination to other parameters. Thus, our study could serve as a reference to such future studies. This chapter is organized as follows. Section 4.2 describes the TC test case. Section 4.3 introduces the simulation design. Section 4.4 presents the results. Section 4.5 summarizes the conclusions and discusses future work.

4.2. Reed-Jablonowski Tropical Cyclone Test Case

The Reed-Jablonowski tropical cyclone test case (Reed and Jablonowski 2011a) is illustrated in the National Center for Atmospheric Research (NCAR)/ Department of Energy (DOE) CAM version 5.1.1 in our study. It is a well-tested tool that has been used to evaluate how the choice of model configuration (e.g., model resolution, dynamical core, physical parameterizations) affects the simulation and representation of tropical cyclones in AGCMs. Figure 4.1 gives a depiction of how it works. It is a special type of idealized initial condition defined in analytic form and consists of a warm-core vortex seed embedded in a quiescent global environment. Fig. 4.1a and Fig. 4.1d show the structure of the vortex seed. Both the vortex seed and environment are 3-dimensional with the former constructed to adhere to gradient wind balance and hydrostatic balance. The setup utilizes an aqua-planet with a sea surface temperature set to a constant $29\,^{\circ}C$ everywhere. When initialized with this balanced state and integrated for 10 days, the model produces a tropical cyclone-like vortex. Fig. 4.1b and Fig. 4.1e show the intensification stage after 5 days integration of the initial vortex seed in CAM 5.1.1. Fig. 4.1c and Fig. 4.1f show the

vortex at day 10. It mimics the process of developing a preexisting vortex seed into a storm-like vortex in an AGCM over a short time period. The TC test case, and others like it, can reveal how realistically a particular model configuration simulates a single type of weather system. In practice, this is typically done by varying a part of the model (e.g., vertical resolution) and comparing the output with a control run. Our control run utilizes the configuration defined in Reed and Jablonowski (2011a).

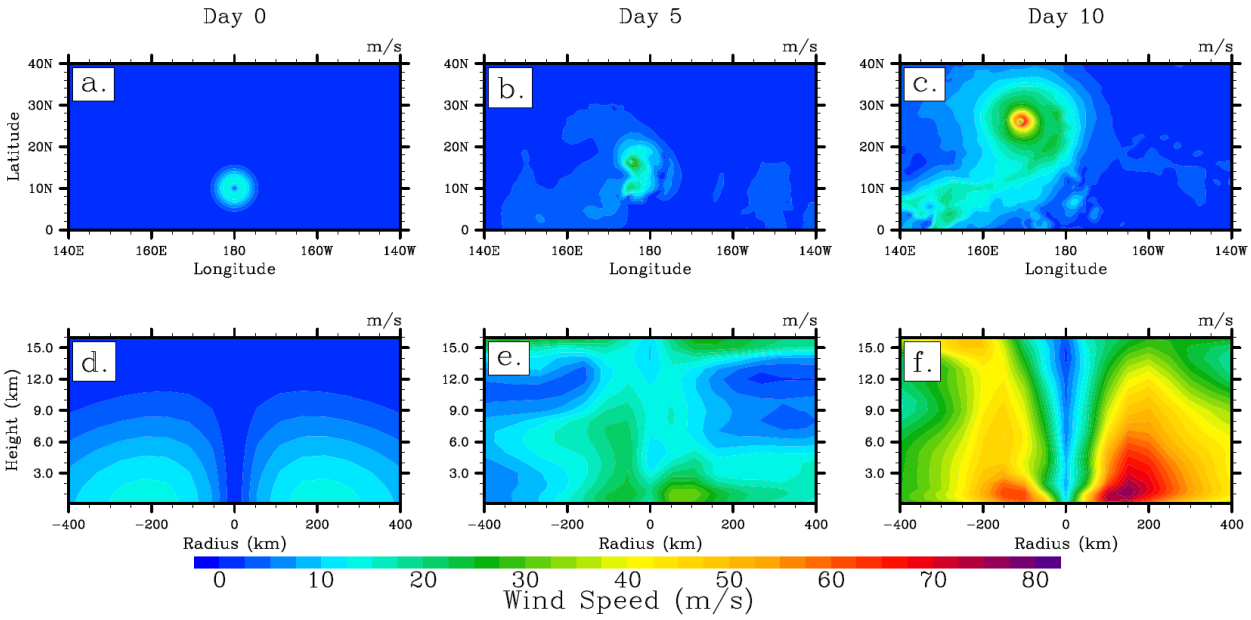

Figure 4.1: Schematic plots of the Reed-Jablonowski TC tese case illustrated with CAM 5.1.1. at days (left) 0, (middle) 5, and (right) 10 at the resolution 0.5° L30. (a) – (c) Latitude-longitude cross section of the wind speed at 100 m above surface. (d) – (f) Longitude-height cross section of the wind speed through the center latitude of the vortex. Radius denotes the distance from the vortex center. Similar plots has been produced in Figure 7 (Reed and Jablonowski 2011a).

The test case concept has been demonstrated to be successful in evaluating TC simulations (Reed and Jablonowski 2011a, b, c) and has also been applied in tests of other dynamical systems (e.g., baroclinic waves; Polvani et al. 2004; Jablonowski and Williamson 2006a). The use of test cases for model evaluation and intercomparison has the advantage of being computationally efficient. In this study, we use the TC test case to evaluate the effect of

parameterized processes on TC development in NCAR/DOE Community Atmosphere Model version 5.1.1 (CAM5) (Neale et al. 2010). The model physical parameterization suite is paired with the default finite volume (FV) dynamical core. The horizontal model resolution is 0.5° and there are 30 vertical levels. The dynamical and physical time steps are 90s and 900s, respectively.

4.3. Simulation Design

While *parameterized physical processes* often refer to a specific suite of schemes such as deep convection and cloud formation, here we use this term to represent processes inside of a parameterization scheme. For example, the process of mass exchange between the convective plume and environmental air occurring in the convection scheme is referred to as an individual physical process here. Each of the parameterized physical processes discussed in this paper is associated with a single physical parameter. Each parameter is set to a particular default value based on observations or the experience of model developers, but most times lies within a range of realistic values. The specific parameter values control the relative strength of the parameterized processes and the process of adjusting parameters to produce a realistic simulation is referred to as *tuning*.

The set of physical processes selected for analysis are chosen from the default parameterizations in CAM 5.1.1, including the Zhang-McFarlane (ZM) deep convection scheme (Zhang and McFarlane 1995; Ritcher and Rasch 2008), the University of Washington (UW) shallow convection scheme (Bretherton et al. 2004; Park and Bretherton 2009), the UW moist turbulence scheme (Bretherton and Park 2009), the Morrison-Gettelman (MG) two moment cloud microphysics (Morrison and Gettelman 2008; Gettelman et al. 2010) and the cloud macrophysics (Park et al. 2014). Table 4.1 lists the chosen parameters, which characterize the

parameterized processes. A more detailed description is provided in Appendix C. Parameters are selected based on two considerations: (1) they have potential influence on TC development based on observations and high resolution regional climate models (Chan 1984; Lord et al. 1984; McFarqauhar and Black 2004; Bassill 2014; Goswami and Mohapatra 2014; Sanger et al. 2014; Sun et al. 2014; Wang 2014), and (2) they constitute a list of candidate parameters as defined by model developers (A. Gettelman and J. Bacmeister, 2014; pers. comm).

Scheme	Parameter	Physical Meaning	Range (units)	Default Value	Test Value
ZM Deep Convection	C0_ocn	Precipitation coefficient over ocean	[0.001 0.045] (m^{-1})	0.045	{0.015, 0.030}
	ke	Tunable evaporation efficiency in ZM deep convection scheme	[0.5E-06 10E-06] ($(kg \cdot m^{-2} \cdot s^{-1})^{-1/2} \cdot s^{-1}$)	1.0E-06	5.0E-06
	alfa	Initial cloud downdraft mass flux	[0.05 0.6] (unitless)	0.1	0.3
	dmpdz	Parcel fractional mass entrainment rate	[-2.0E-03 0] (m^{-1})	-1.0E-03	-0.2E-03
	tau	Time scale for consumption rate of CAPE for deep convection	[1800 28,800] (s^{-1})	3600	10000
	capelmt	Threshold value for CAPE for deep convection	[20.0 200.0] ($m^2 \cdot s^{-2}$)	70.0	120
	Cu	Controls the updraft convective momentum transport	[0.0 1.0] (unitless)	0.4	0.7
	Cd	Controls the downdraft convective momentum transport	[0.0 1.0] (unitless)	0.4	0.7
Shallow convection	rpen	Penetrative entrainment efficiency	[1.0 10.0] (unitless)	5.0	7.0
	criqc	Maximum updraft condensate	[0.5E-03 1.5E-03] ($kg \cdot kg^{-1}$)	0.7E-03	1.2E-03
	kevp	Evaporative efficiency	[1.0E-06 20.0E-06] ($(kg \cdot m^{-2} \cdot s^{-1})^{-1/2} \cdot s^{-1}$)	2.0E-06	10.0E-06
UW	rkm	Updraft lateral mixing	[4.0 8.0]	7.0	5.0

		efficiency	(unitless)		
	aumax	Maximum core updraft fractional area	[0.05 0.15] (unitless)	0.1	0.08
	Dcs	The threshold size separating cloud ice from snow	[100.0 500.0] (μm)	400.0	300.0
MG Two Moment Cloud Microphysics	ai	Fall-speed parameter for cloud ice	[350.0 1400.0] (s^{-1})	700.0	1000.0
	as	Fall-speed parameter for snow	[5.86 23.44] ($m^{0.59} \cdot s^{-1}$)	11.72	15.0
	cdnl	Cloud droplet number limiter	[0 1.0E07] ($\#\cdot m^{-3}$)	0.5E06	0.5E07
	eii	Collection efficiency aggregation ice	[0.001 1.0] (unitless)	0.1	0.5
	qcvar	Inverse relative variance of sub-grid cloud water	[0.5 5.0] (unitless)	2.0	4.0
	wsubimax	Maximum subgrid vertical velocity for ice nucleation	[0.1 1.0] ($m \cdot s^{-1}$)	0.2	0.5
	wsublmin	Minimum subgrid vertical velocity for liquid nucleation	[0.0 1.0] ($m \cdot s^{-1}$)	0.2	0.5
UW Moist Turbulence Scheme	a2l	Moist entrainment enhancement parameter	[10.0 30.0] (unitless)	30.0	20.0
Cloud Macrophysics	cldfrc_rhminh	Minimum relative humidity for high stable clouds	[0.65 0.85] (unitless)	0.8	0.7
	cldfrc_rhminl	Minimum relative humidity for low stable clouds	[0.80 0.99] (unitless)	0.90	0.86

Table 4.1: Lists of the tunable physical parameters, their physical meaning, uncertain range, units, default value and test value. Those parameters are selected from Zhang-McFarlane (ZM) deep convection, University of Washington (UW) shallow convection, UW moist turbulence, Morrison-Gettelman (MG) two moment cloud microphysics and Cloud macrophysics schemes. Each parameter has four sampling points: minimum value, maximum value, default value and a different fourth test value randomly selected from its range. The first parameter is chosen to have two test values as its default value is equivalent to maximum value. CAPE: convective available potential energy.

4.3.1. One-at-a-time sensitivity analysis

Each parameterized process and its corresponding physical parameter, is evaluated at four values: default, minimum value, maximum value, and a fourth value randomly selected from the parameter range (Table 4.1). In the case of C0_ocn, the default value matches the maximum value and therefore an additional test value is used. Minimum and maximum values were obtained from model developers based on either experience or observation, while the default values are those used in version 5.1 of the CAM. C0_ocn is the precipitation conversion efficiency in ZM deep convection scheme. It determines the conversion from cloud liquid water to rainwater. Larger C0_ocn means more cloud liquid water converted into rainwater and subsequent precipitation. Each simulation examines (perturbs) one physical parameter, with all other parameters set to their default values. The control run is defined by setting all 24 physical parameters to their default values. The initial condition that defines the tropical cyclone test case is the same in all simulations, and is consistent with the case represented by Reed and Jablonowski (2011a). One-at-a-time parameter perturbation design results in $24\times3+1=73$ simulations in total. An additional 19 simulations were carried out to better sample the model response functions to key physical parameters. To evaluate the effect of internal model variability, additional four member perturbations runs are added to each case with slightly different initial conditions. Specifically, the location of initial vortex center is moved to the following four positions: $(9.5^{\circ},179.5^{\circ})$, $(9.5^{\circ},180.5^{\circ})$, $(10.5^{\circ},179.5^{\circ})$, and $(10.5^{\circ},180.5^{\circ})$.

4.3.2. Latin Hypercube Sampling

Following the results from one-at-a-time analysis, we then used a Latin Hypercube Sampling (LHS) method to perturb eight key physical parameters across different physical schemes and

investigate the interactive effect among them. The eight selected physical parameters are the parcel fractional mass entrainment rate in the ZM deep convection scheme (dmpdz), the time scale for consumption rate of CAPE for ZM deep convection (tau), the precipitation coefficient over ocean in the ZM deep convection scheme (C0_ocn), the updraft lateral mixing efficiency (rkm) in the shallow convection scheme, the threshold size separating cloud ice from snow in cloud microphysics (Dcs), the fall-speed parameter for cloud ice in the cloud microphysics scheme (ai), the moist entrainment enhancement parameter (a2l) in the turbulence scheme, and the minimum relative humidity for low stable clouds (c._rhminl) in the cloud macrophysics scheme.

4.3.3. Six tropical cyclone characteristics

The impact of parameterized physical processes is examined for six tropical cyclone characteristics at the mature stage of TC development. These are the day 9-10 time mean: storm intensity (m s^{-1}), precipitation rate (mm hr^{-1}), shortwave cloud radiative forcing (SWCF; W m^{-2}), longwave cloud radiative forcing (LWCF; W m^{-2}), cloud liquid water path (LWP; g m^{-2}) and cloud ice water path (IWP; W m^{-2}). The TC intensity is defined as the maximum wind speed at 100 m height above the surface (Reed and Jablonowski 2011a). The other five TC characteristics are directly output by the model and spatially distributed. To facilitate the comparison of the impact of parameterized processes, we measured them by computing area-weighted means over the tropical cyclone region. Detection of the tropical cyclone in the global field is straightforward in our case, as the output only contains one storm-like vortex. This is an additional advantage of an idealized test case framework.

We detect the tropical cyclone-like vortex via three simple steps: (1) find the minimum surface pressure, which is defined to be the storm center; (2) search the output field (e.g.

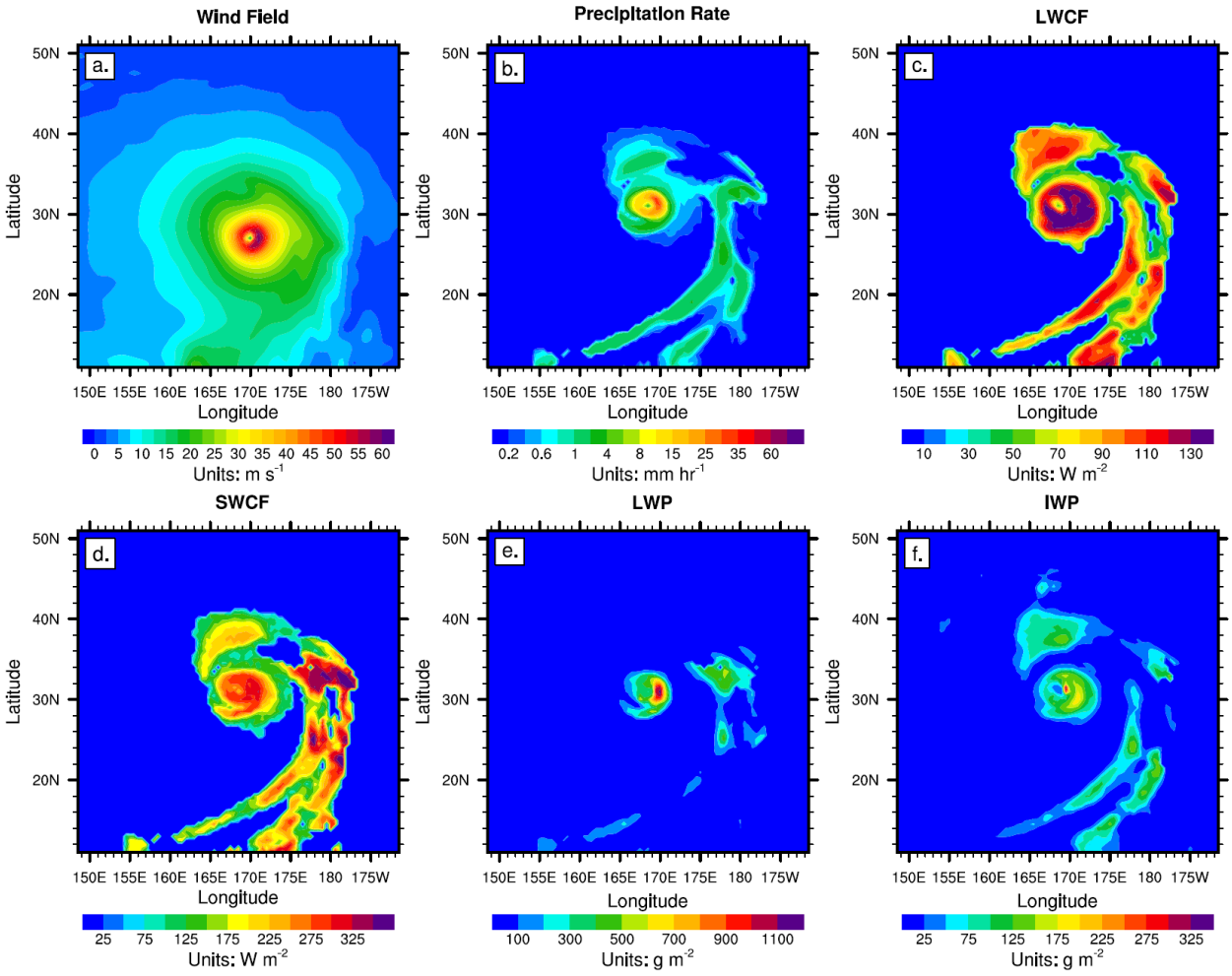

Figure 4.2: Example plots of the six selected characteristics of the control tropical cyclone simulation: (a) wind field, (b) total precipitation rate, (c) longwave cloud radiative forcing (LWCF), (d) shortwave cloud radiative forcing (SWCF), (e) cloud liquid water path (LWP), and (f) cloud ice water path (IWP). Note, Fig. 1d shows the magnitude of SWCF.

precipitation rate) in a square latitude/longitude region that spans +/- 20 degrees from the storm center; (3) select those points that satisfy both of the two following criteria: (a) wind speed at 100-m height above surface greater than 6 m s^{-1} , and (b) outgoing longwave radiation (OLR) less than 230 W m^{-2}. Application of steps (1) – (3) result in a well-defined tropical cyclone, as

illustrated in Figure 4.2, which shows the simulated tropical cyclone characteristics in the control case. The wind, precipitation, LWCF, SWCF and IWP fields all show the calm eye and spiral band features. The area-weighted mean value of each quantity is computed from the +/- 20 degree region around the cyclone center.

4.4. Results

4.4.1. Linear perturbation (One-at-a-time) analysis

4.4.1.1 Impact of parameterized physical processes on simulated tropical cyclone

Parameterized physical processes, especially those associated with deep convection, contribute significantly to the simulation of TC characteristics in CAM 5.1.1 (Figure 4.3). The specific parameterized process that has the greatest effect differs for the output metric of interest.

Perturbation of one parameter at a time reveals the simulation of TC intensity (Fig. 4.3a) is most sensitive to the parcel fractional mass entrainment rate (dmpdz), which denotes the strength of mass exchange between convective plume and environmental air. The range of TC intensities caused by the modification of this single process can be as large as 47.2 $m \cdot s^{-1}$, producing a change from tropical depression to category-4 tropical cyclone on the Saffir-Simpson scale. In contrast, perturbation of all other parameterized processes leads to a change of simulated TC intensity within 10.0 $m \cdot s^{-1}$, which is quantified as the absolute difference between maximum and minimum simulated TC intensity while perturbing the selected physical parameter throughout its range. The two parameters (Cu and Cd) that control the upward and downward convective momentum transport have a small effect on the TC intensity. Reed and Jablonowski (2011b) show that the inclusion of the convective momentum transport process in CAM does not affect TC intensity much. Hogan and Pauley (2007) find that it can influence TC track.

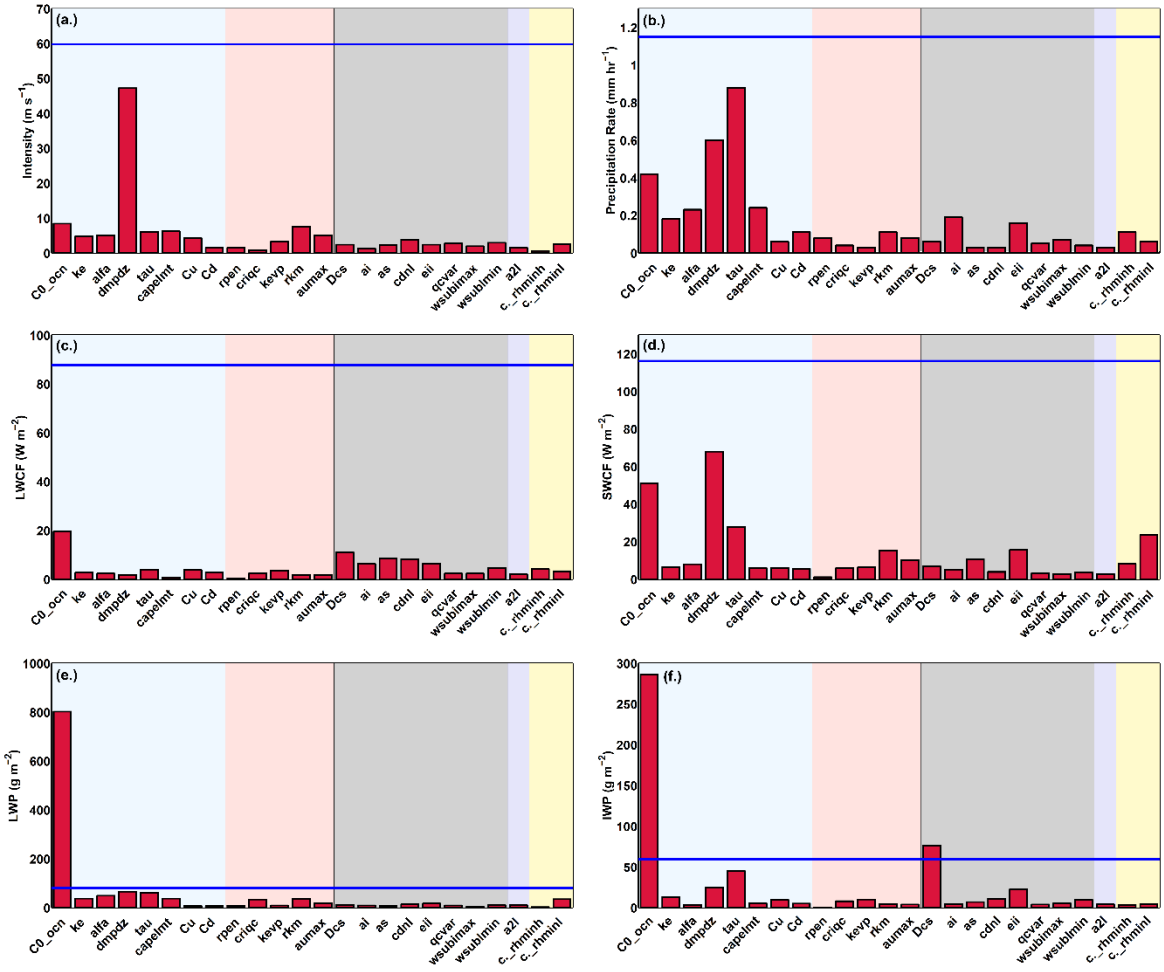

Figure 4.3: Changes in simulated tropical cyclone (a) intensity, (b) precipitation rate, (c) longwave cloud radiative forcing (LWCF), (d) shortwave cloud radiative forcing (SWCF), (e) liquid water path (LWP), and (f) ice water path (IWP) caused by perturbation of each of the 24 physical parameters spanning its range. The solid blue line shows the value of the control run to allow the reader to assess the relative change. Background color is applied to distinguish the physical schemes. Light blue denotes ZM deep convection scheme; light pink denotes UW shallow convection scheme; light gray denotes MG two moment cloud microphysical schemes; light purple denotes the UW moist turbulent scheme and light yellow denotes the cloud macrophysics scheme.

The TC precipitation rate (Fig. 4.3b) is most sensitive to the time scale for consumption of the convective available potential energy (tau), second most sensitive to parcel fractional mass entrainment rate (dmpdz) and third most sensitive to precipitation conversion efficiency (C0_ocn). Yang et al. (2013) examined the tropical precipitation to several physical parameters

in ZM deep convection scheme using CAM 5, they found that the simulated convective precipitation is most sensitive to tau, dmpdz and alfa (initial cloud downdraft mass flux). Alfa plays a relatively less important role in TC precipitation, instead, C0_ocn plays a relatively more important role in TC precipitation compared to tropical convective precipitation. Interestingly, the TC intensity is weakly influenced by changes in tau and C0_ocn. This shows that one can change the tau and C0_ocn to tune the TC precipitation while leaving TC intensity unperturbed.

Generally, LWCF is not strongly affected by changes in the selected physical parameters (Fig. 4.3c). It is most sensitive to the precipitation conversion efficiency (C0_ocn). The parameterized processes in cloud microphysics also play a considerable role in affecting TC LWCF simulation. For example, the threshold size separating cloud ice from snow (Dcs). This parameter controls the fraction of cloud ice that remains suspended vs. falling to the surface. A larger threshold leaves more ice particles in upper tropospheric clouds, which leads to larger LWCF. The empirical fall speed parameter for ice (ai) and snow (as) also determines the value of simulated TC LWCF. Larger parameters indicate larger fall speeds and hence greater ice and snow particles settling and lower value of LWCF. The remaining physical parameters have minimal impact on LWCF. Yang et al. (2013) shows that tropical mean ($0-360^{\circ}E, 30^{\circ}S-30^{\circ}N$) LWCF is most sensitive to tau, dmpdz and has very minor sensitive to C0_ocn.

The TC SWCF (Fig. 4.3d) is most sensitive to the parcel fractional mass entrainment rate (dmpdz), which is also the parameter that most influences TC intensity. In addition to dmpdz, the simulated TC SWCF is sensitive to changes in C0_ocn and tau, and to lesser extent cldfrac_rhminl in the cloud macrophysics scheme. Changes in all other parameters cause minor changes in simulated TC SWCF. Yang et al. (2013) shows the tropical mean SWCF is most sensitive to C0_ocn and tau while it has minor sensitive to dmpdz among the parameters in ZM

scheme. In addition, Zhao (2014) revealed that both cumulus entrainment rate and convective microphysics can strongly affect SWCF, and through this impact cloud feedback and climate sensitivity.

While changes in deep convective precipitation efficiency (C0_ocn) have a minor influence on TC intensity, they cause significant uncertainty in TC LWP (Fig. 3e). The change can be as much as 10 times the control value. Perturbation of most parameters causes TC LWP to change considerably great. Only 6 physical parameters produce a weak impact on simulated TC LWP: Cu, Cd, rpen, as, wsubimax and cldfrc_rhminh. Yang et al. (2013) shows that tropical mean LWP is most sensitive to C0_ocn and dmpdz.

The TC IWP (Fig. 4.3f) is also most sensitive to changes in the precipitation conversion efficiency over ocean (C0_ocn). The three most important physical parameters to IWP is C0_ocn, Dcs and tau. In total, 12 physical parameters show considerable impact: C0_ocn, ke, dmpdz, tau, Cu, criqc, kevp, Dcs, as, cdnl, eii, and wsublmin. The remaining 12 physical parameters show little impact on simulated TC IWP: alfa, capelmt, Cd, rpen, rkm, aumax, ai, qcvar, wsubimax, a2l, and cldfrc_rhminh, and cldfrc_rhminl. Yang et al. (2013) shows that tropical mean IWP is most sensitive to C0_ocn and tau. While we see cldfrc_rhminl plays minor role in cloud properties (LWCF, SWCF, LWP and IWP) of tropical cyclone, Zhang et al. (2012) shows that smaller cldfrc_rhminl can lead to better simulation of both low clouds and high clouds in CAM 4. Their study also shows that smaller alfa result in a better simulation of high clouds.

4.4.2 Response function analysis

The above section has shown the relative influence of changes to a set of pre-defined physical parameters on TC simulation. We now quantify the response function of six simulated TC characteristics to changes in their most sensitive parameters by adding more sampling points. The resulting relationships are shown in Figure 4.4. The five-member ensemble simulations are conducted to quantify the internal noise of models. Solid blue lines show the mean values, and the dotted lines show the response function from each member. Overall, we see that internal variability is small for the cases of intensity (Fig. 4.4a), SWCF (Fig. 4.4d), LWP (Fig. 4.4e) and IWP (Fig. 4.4f). It is relatively large for the cases of precipitation rate (Fig. 4.4b) and LWCF (Fig. 4.4c). However, we can see the response function is consistent among different dotted lines in both cases. This shows that the relationship revealed by the ensemble mean values are robust. The control value is marked with a red star. The extreme value that has the largest difference from the control value is marked with a green star. Example spatial patterns of all the fields in the extreme parameter value cases are shown in Figure 4.5.

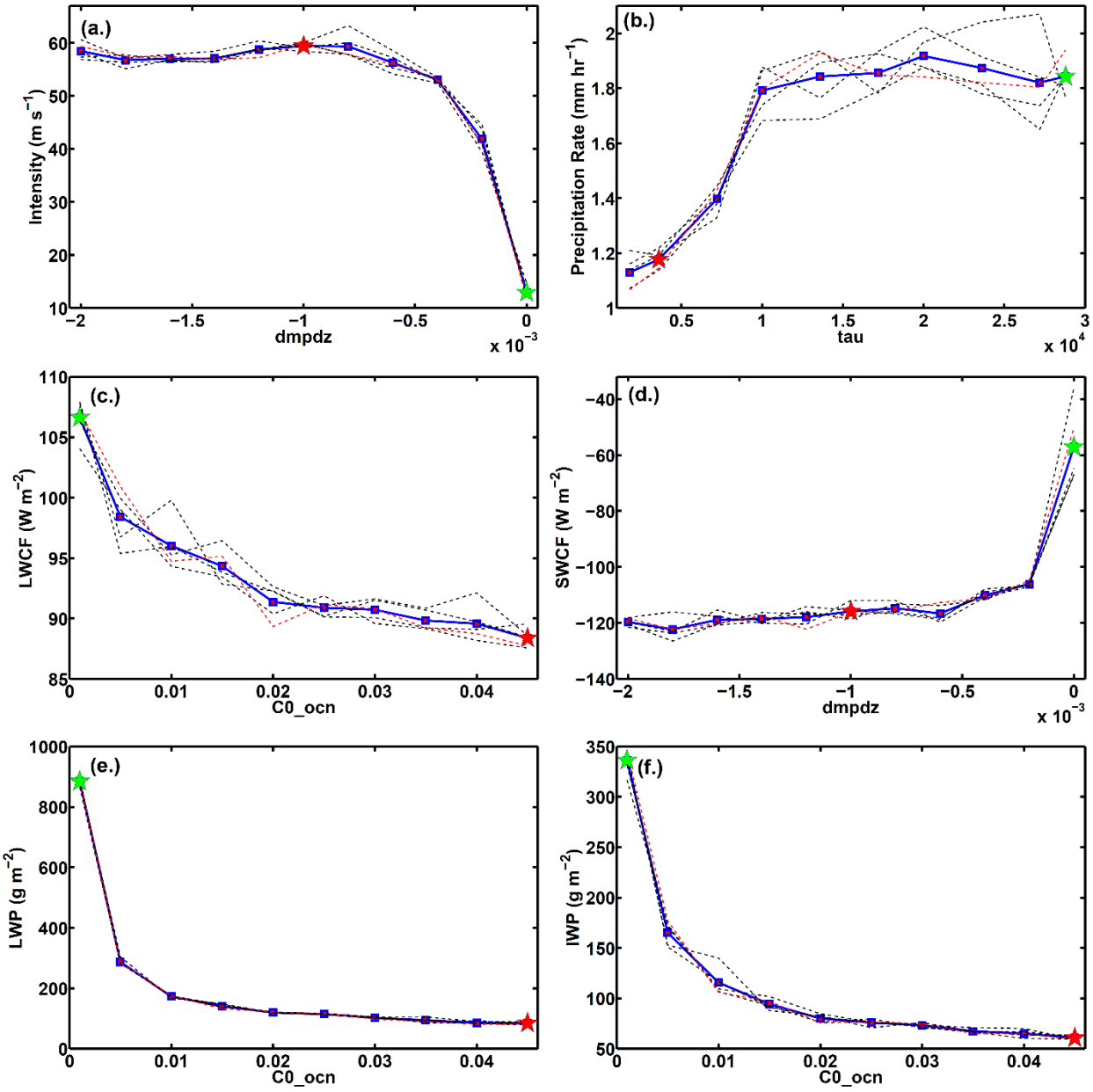

Figure 4.4: Response of TC characteristics: (a) Intensity, (b) Precipitation rate, (c) LWCF, (d) SWCF, (e) LWP, and (f) IWP to changes in each variable's most sensitive physical parameter. The red dotted line represents the response function computed from the control run. The black dotted lines represent the results from the four member perturbation runs, which are produced by slightly change the location of vortex center in the initial condition. The blue solid line represents the mean from the five-member ensemble runs. Red star marks the control value. Green star marks the extreme value that has larger contrast with the control value.

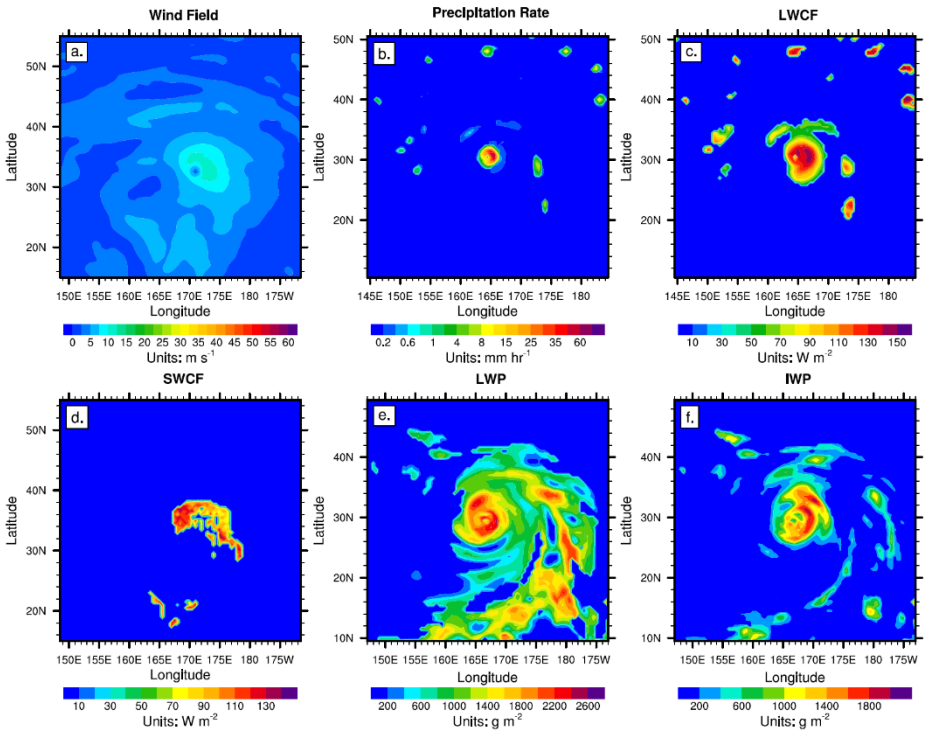

Figure 4.5: The output fields of extreme runs that are marked out by green star in Figure 4.4. (a) wind field, (b) precipitation rate field, (c) LWCF, (d) SWCF, (e) LWP, and (f) IWP.

Fig. 4.4a depicts changes in TC intensity resulting from changes in parcel fractional mass entrainment rate as it is varied between its minimum and maximum value. As the magnitude of dmpdz decreases, the TC intensity decreases from a Cat-4 tropical cyclone to a tropical depression. The parcel fractional mass entrainment rate (dmpdz) controls the exchange of mass between the convective plume and environmental air. Smaller dmpdz magnitudes indicate smaller rates of mixing of relatively cool and dry air parcel into convective plumes. This leads to stronger upward convective mass flux, which in turn stabilizes the atmosphere. Increased atmospheric stability leads to a weaker storm. The mechanism is demonstrated by Lim et al. (2015). Note that the response function is non-linear: changes in dmpdz have little effect until dmpdz increases to -0.5x10^{-3} m^{-1}, at which point the sensitivity changes significantly. A value of 0 represents no entrainment and leads to the tropical depression. Equivalent to that, shutting off

the dilute plume calculation coincides with a significant weakening of the TC (Reed and Jablonowski 2011b). Also, Zhao et al. (2012) found a non-monotonic behavior in TC frequency response to cumulus entrainment rate. Our result provides further evidence of the importance of entrainment on modeled TC intensity. The response function shows that the uncertainty in simulated TC intensity from the internal model configuration can be large, and that tuning the physical parameters by perturbing them in small increments may yield misleading results.

Fig. 4.4b quantifies the relationship between simulated TC precipitation rate and time scale of the consumption rate of CAPE (tau). As tau increases, the precipitation rate increases as well; however, the response function is non-monotonic, exhibiting minor change beyond tau of ~ $1.4\text{x}10^4\ s^{-1}$ and a subsequent increase above approximately $2.8\text{x}10^4\ s^{-1}$. Qian et al. (2015) shows that global mean precipitation does not respond linearly and monotonically to parameter change. Tau is the prescribed time scale that determines the rate of CAPE consumption, once moist convection has been initiated. Larger values of tau lead to longer prescribed time scales for CAPE consumption. This leads to weaker upward mass flux from the subcloud layer into the cloud (eq. 4 in Appendix C). This indicates smaller entrainment from the environment and thus less dry air mix into the convective plume, which implies less moisture loss inside the cloud. Less moisture loss allows for a larger precipitation rate.

Fig. 4.4c shows that the simulated TC LWCF decreases with larger precipitation conversion efficiency (C0_ocn), consistent with the fact that increased precipitation should result in less water arriving in the upper troposphere and consequently less cirrus cloud. Fig. 4.4d shows that the magnitude of SWCF decreases with increasing parcel fractional mass entrainment rate (dmpdz). This is consistent with the change of TC intensity. Increasing dmpdz leads to a more stable atmosphere, limiting the growth of deep convective clouds, and leading to smaller

magnitude SWCF. The LWP (Fig. 4.4e) and IWP (Fig. 4.4f) decrease with increasing precipitation conversion efficiency (C0_ocn). When C0_ocn is in the range from 0.001 m^{-1} to 0.01 m^{-1}, the LWP and IWP drop exponentially. C0_ocn determines the conversion from cloud liquid water to rainwater in the updraft. Larger C0_ocn means more cloud liquid water converted into rainwater and subsequent precipitation. This leads to smaller cloud LWP and IWP. Yamada and Satoh (2013) examined the response of TC associated LWP and LWP to global warming and show that tropical averaged LWP (IWP) is reduced by approximately 0.86% (2.76%). The significant sensitivity of TC LWP and IWP to C0_ocn suggests that parameterized physical process would exert great uncertainty on such problems.

4.4.2.1 Further exploration

Figure 4.3 clearly identifies the important physical parameters to the six different TC characteristics and rules out the minor ones. Figure 4.4 characterizes the response function between the six TC characteristics and their most sensitive parameters. Building upon these results, it is worthwhile to highlight two additional points.

First, one single physical parameter can have a different impact on the six TC characteristics. Figure 4.6 shows the uncertainty ratio, which is defined as the uncertainty range (the range of model output values) produced by changes in the same physical parameter divided by the control value for each of the six TC characteristics. For example, Fig. 4.6(a) shows that while C0_ocn causes large uncertainty on LWP (~1000%), and IWP (~400%), it causes much smaller uncertainty on TC intensity, precipitation rate and SWCF. This implies that it may be useful in modifying the LWP and IWP fields, while it is not as important to other fields, especially to TC intensity. The difference in sensitivity from one parameter can be further supported by parcel

fractional mass entrainment rate (dmpdz) (Fig. 4.6b). It completely controls the TC intensity, but has negligible effect on TC LWCF. Fig. 4.6c also demonstrates that an individual physical parameter can have different impacts on different characteristics of simulated TCs.

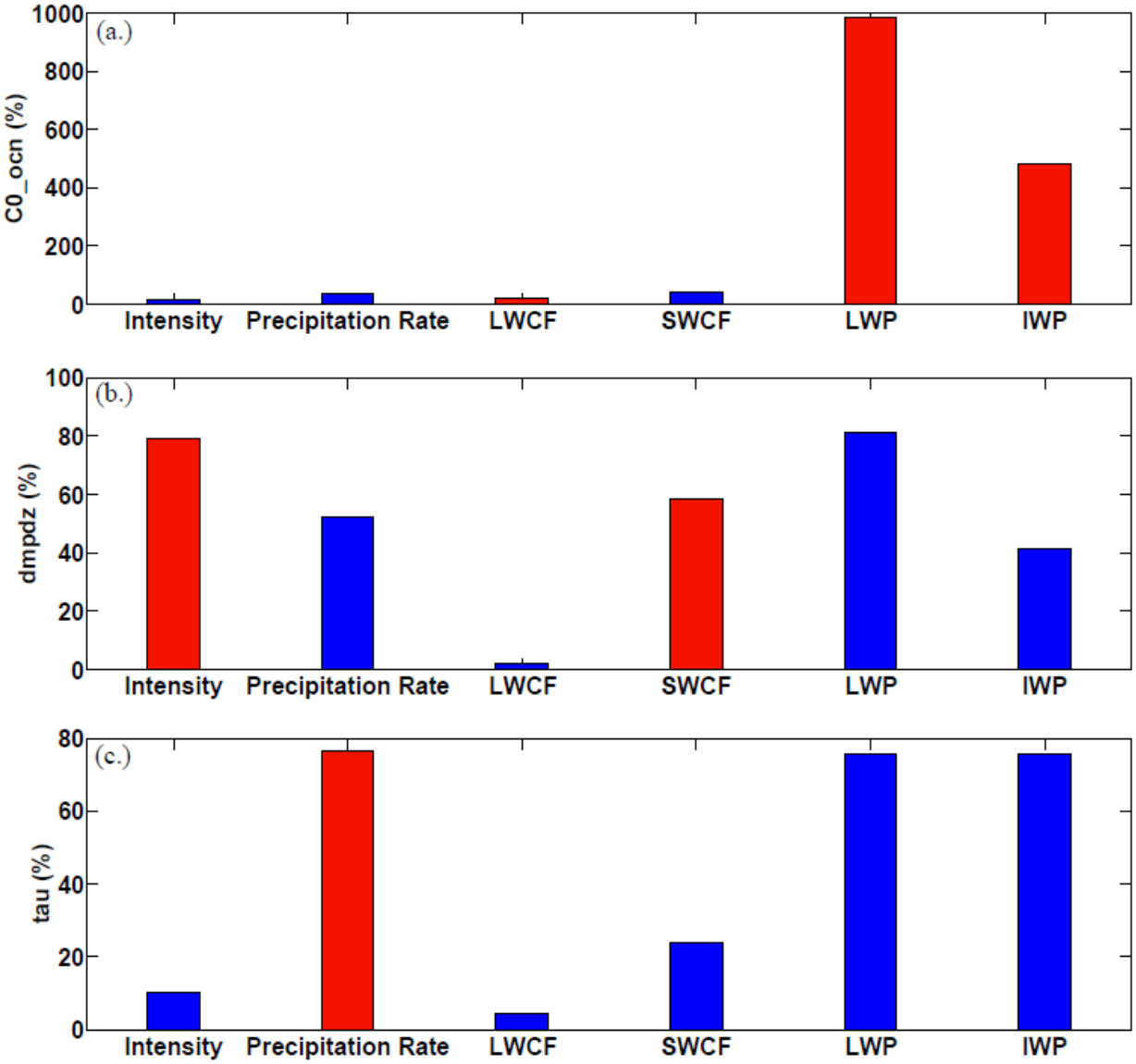

Figure 4.6: The comparison of the uncertainty ratio among simulated TC intensity, precipitation rate, LWCF, SWCF, LWP and IWP for three parameter cases (a) C0_ocn, (b) dmpdz, and (c) tau. The uncertainty ratio is defined as the uncertainty range (Figure 3) divided by the control value. The control value is calculated from the simulation with all the physical parameters set to default value. The red bars are marked out for the cases when the TC characteristics have the largest uncertainty range, of which the response functions are shown in Figure 4. Note the scale in Y-axis is different in (a), (b) and (c).

Second, the maximum uncertainty ratio of the six TC characteristics is significantly different. The red bar in Figure 4.6 marks out the largest uncertainty ratio for each characteristic. This ratio for LWCF is as small as 20% (Fig. 4.6a). The uncertainty ratio is significantly larger for TC LWP and IWP. It is 40% ~ 100% for TC intensity, precipitation rate, LWCF and SWCF, and can be as large as 1000% for TC LWP and 500% for TC IWP (Fig. 4.6a). This shows that TC LWP and IWP are most affected by changes in the physical parameters while LWCF is relatively less sensitive. The results also suggest that parameterizing the conversion from cloud liquid water to rainwater in the updraft of deep convection may be a cause of the well-known uncertainty in cloud liquid and ice content in AGCMs.

4.4.2. Linear versus nonlinear

The one-at-a-time experiments enable us to quantity the relative importance of each physical parameter on the six simulated characteristics, however, whether the interactive effect among physical parameters across different schemes will exert an additional influence on the simulated fields remains unknown. This part of the work uses LHS to simultaneously perturb eight key physical parameters from the five physical schemes and generate 480 samples, which leads to 480 numerical simulations in total. It aims to reveal whether an interactive effect among the various physical parameters exists, and whether it may have an important influence on simulated TC features. Figure 4.7 shows the comparison of uncertainty range caused by an individual physical parameter (OAT) and eight simultaneously perturbed physical parameters (LHS). The uncertainty range is defined as the maximum value minus the minimum value of the simulated output variable, while the input physical parameters are perturbed in an OAT or LHS way. The difference between OAT and LHS is that LHS changes the selected eight physical parameters simultaneously and allows the existence of an interactive effect among them, while OAT only

perturbs one physical parameter with all other parameters fixed to their default value. Similar uncertainty range between OAT and LHS experiments indicates that the interactive effect among physical parameters does not play additional role in affecting the simulated output. Greatly enlarged uncertainty range between OAT and LHS experiments indicates that the interactive effect amplifies the sensitivity and contributes to a broader uncertainty range. From Fig. 4.7, we see that the interactive effect among physical parameters play a significant role in simulated precipitation rate and LWCF. It affects the SWCF and IWP moderately. It does not contribute any extra uncertainty for intensity and LWP. This indicates that the uncertainty caused by changes in dmpdz and C0_ocn could represent the uncertainty associated with all parameterized physical process for intensity and LWP, respectively. In other words, the uncertainty in the parameterized physical processes affecting TC intensity is mainly caused by changes in dmpdz. It is the same case for LWP.

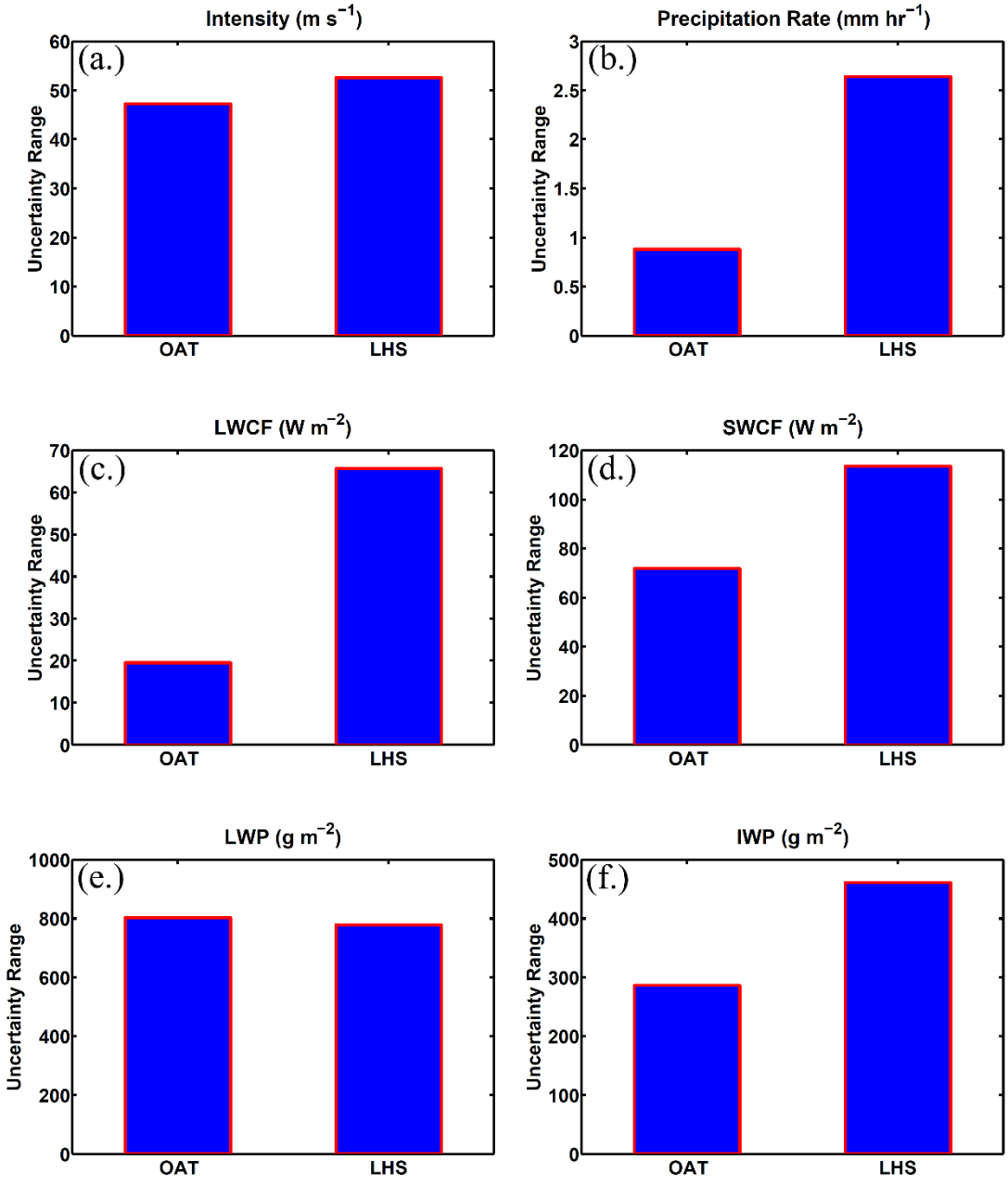

Figure 4.7: Comparison of the caused uncertainty range by linear (OAT) and nonlinear (LHS) perturbation of physical parameters on simulated TC characteristics: (a) intensity, (b) precipitation rate, (c) LWCF, (d) SWCF, (e) LWP, and (f) IWP. OAT: one-at-a-time, LHS: latin hypercube sampling. The uncertainty range are quantified by the difference between maximum and minimum values. 8 key physical parameters are perturbed for LHS: dmpdz, tau, C0_ocn, rkm, Dcs, ai, a2l, c._rhminl. 480 simulations are run for LHS.

While the interactive effect among physical parameters can be seen to greatly enlarge the uncertainty range for precipitation rate, LWCF, SWCF and IWP, it is also informative to consider the effects on the shape of the probability distribution of the simulated outputs. Figure 4.8 shows the distribution of simulated output for the 480 samples generated by LHS. It is the kernel density estimate, a non-parametric way to estimate the probability density function of a random variable. With the exception of precipitation rate, distributions of MWS, LWCF, SWCF, LWP and IWP all have long tails, indicating that there are a range of values that occur with very low probability density. The distribution of LWCF (Fig. 4.8c) shows that ranges of [60 75] $W \cdot m^{-2}$ and [105 130] $W \cdot m^{-2}$ do occur, however, they are relatively rare. Most of the values of LWCF occur between 75 $W \cdot m^{-2}$ and 100 $W \cdot m^{-2}$. Values of TC intensity, SWCF, LWP and IWP are similarly concentrated near the mid-point of their ranges. TCs with maximum wind speeds between 10 $m \cdot s^{-1}$ and 50 $m \cdot s^{-1}$ are rare cases. Most TCs have an intensity between 50 $m \cdot s^{-1}$ and 65 $m \cdot s^{-1}$. SWCF mainly lies from -140 $W \cdot m^{-2}$ to -80 $W \cdot m^{-2}$. LWP mainly lies between 50 $g \cdot m^{-2}$ to 250 $g \cdot m^{-2}$ and IWP ranges from 0 $g \cdot m^{-2}$ to 150 $g \cdot m^{-2}$. In contrast to these variables, the distribution of mean precipitation rate does not have long tails. It generally ranges between [0.5 3.0] $mm \cdot hr^{-1}$ with a band of relatively high density between 1.0 $mm \cdot hr^{-1}$ and 2.2 $mm \cdot hr^{-1}$. These results show that the interactive effect among physical parameters contributes to broadening the entire shape of precipitation distribution and it greatly enlarges the uncertainty of LWCF, SWCF, and IWP by producing more extreme cases.

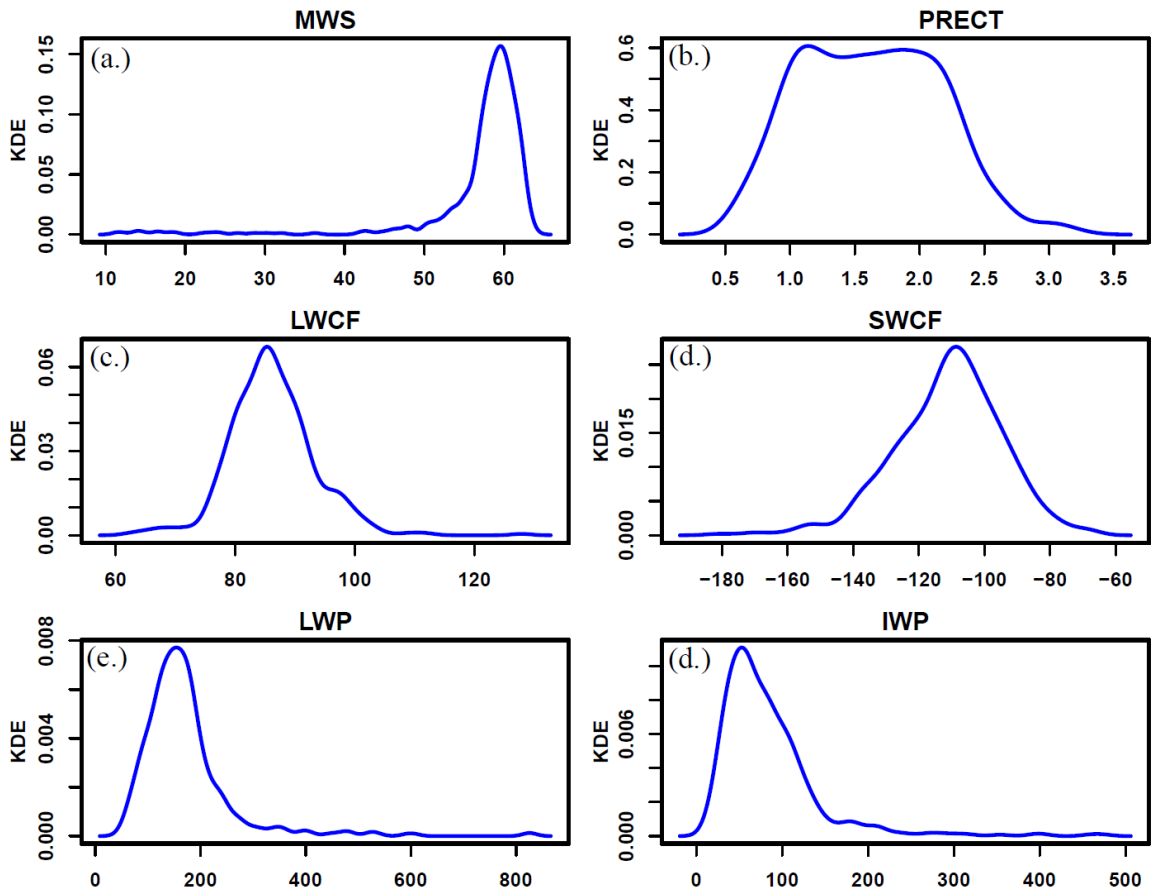

Figure 4.8: Kernel Density Estimate (KDE) of (a). Intensity, (b). Total precipitation rate, (c). LWCF, (d). SWCF, (e). LWP, and (f). IWP from the 480 simulated samplings.

4.4.3. Intrinsic uncertainty versus extrinsic uncertainty

Numerical simulations of weather and climate are inherently uncertain, and quantifying the various types of uncertainties is a key aspect to measuring the ability of AGCMs to simulate tropical cyclones. Intensity is an important feature for tropical cyclones; hence, we compare the parameter uncertainty, model initial condition uncertainty, and model structural uncertainty for simulated tropical cyclone intensity (Figure 4.9). Examples of structural uncertainty include simulated model change due to different spatial resoltuions, different dynamical cores or physical parameterizations. Here, model structural uncertainty is represented by the uncertainty

caused by horizontal resolution change. Fig. 4.9a shows the histogram of simulated tropical cyclone intensity from the 480-member ensemble run generated by perturbing the eight key physical parameters simultaneously with the LHS method. Fig. 4.9b shows the histogram of simulated tropical cyclone intensity from 300 samples generated by perturbing the five initial conditions. This histogram is constructed using the EMARS emulator, which is described in Chapter 3. The five initial conditions are perturbed in a small range around their control values. The perturbed range for initial size (RMW) is [175 225] km and [18.0 22.0] $m \cdot s^{-1}$ for initial intensity (MWS). Temperature lapse rate (GAMMA) ranges from [6.75 7.25] $K \cdot km^{-1}$, sea surface temperature (SST) spans [28 30] $^{\circ}C$, and the 500 hPa relative humidity is set to values between [0.4 0.6]. Note that the range of model initial conditions tested here is a subset of the IC ranges used in Chapter 3, as we are concerned primarily with examining the model initial condition uncertainty around the control case. Fig. 4.9c shows the histogram of intensity difference rather than intensity itself, when the model resolution is changed from $1.0^{\circ} \times 1.0^{\circ}$ to $0.5^{\circ} \times 0.5^{\circ}$ for each of the 300 samples. The data used to generate these samples are described in Chapter 3. Recall that three groups of ensemble simulations are conducted. Each group has 300-members and the five initial conditions are perturbed with a LHS method, while all model parameters are set to their default value. The only difference among these three groups is the horizontal resolution. One is run with $1.0^{\circ} \times 1.0^{\circ}$, the second is $0.5^{\circ} \times 0.5^{\circ}$, and the third is $0.25^{\circ} \times 0.25^{\circ}$. Alternatively, each set of 300-member LHS initial conditions is run with three different model resolutions: $1.0^{\circ} \times 1.0^{\circ}$, $0.5^{\circ} \times 0.5^{\circ}$ and $0.25^{\circ} \times 0.25^{\circ}$. Thus, the intensity difference is calculated for each case with different model resolution, but identical model initial conditions and physical parameters. Use of the 300 ensemble members ensures the TC intensity spread across the full range from tropical depression to Cat-5 TC in Saffir-Sampson Hurricane scale. In

this way, Fig. 4.9c provides information about the model structural effect on simulated TC intensity in a more robust way. Fig. 4.9d shows a similar result to Fig. 4.9c, but for the case in which the model resolution is changed from $0.5^{\circ} \times 0.5^{\circ}$ to $0.25^{\circ} \times 0.25^{\circ}$.

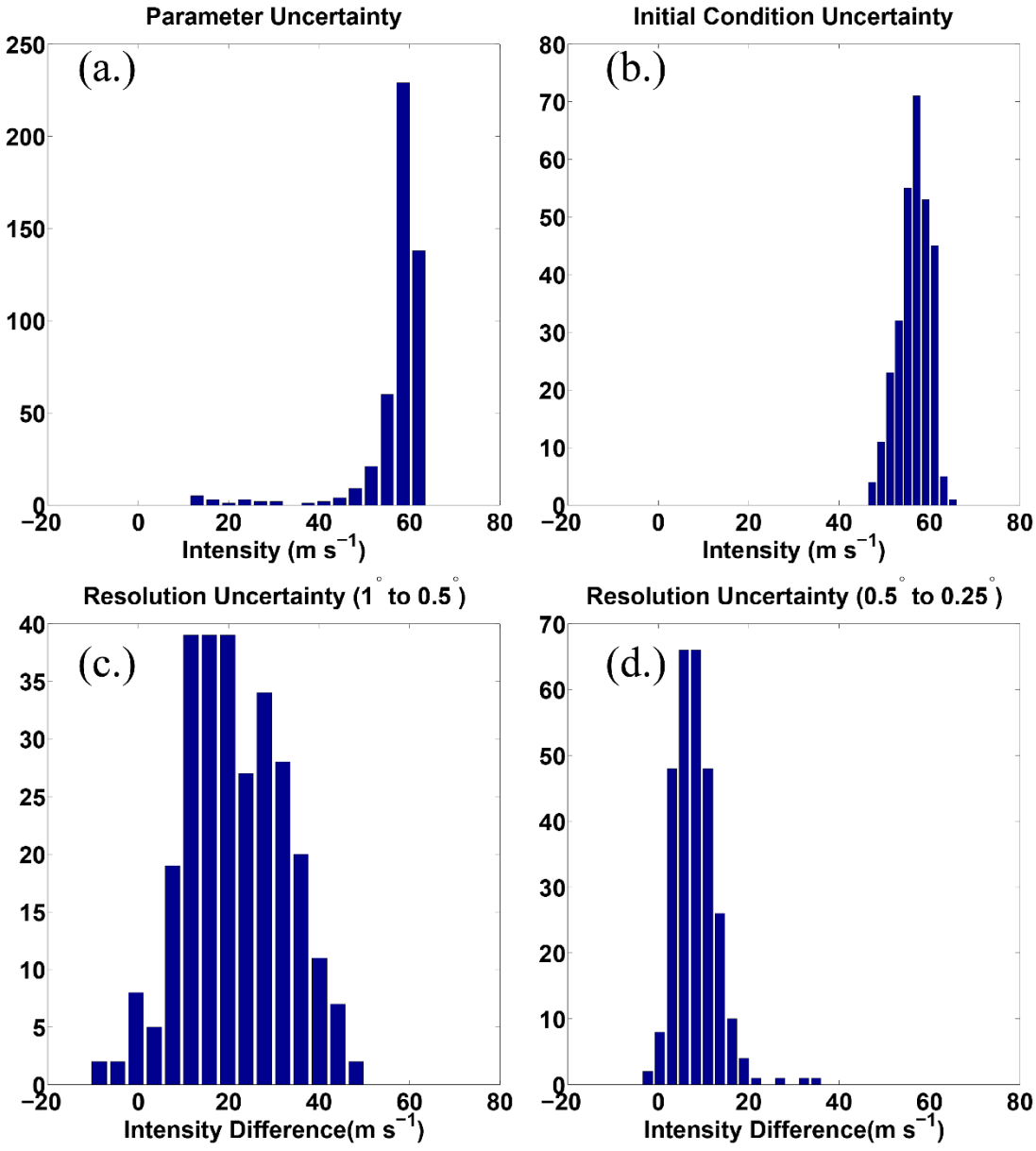

Figure 4.9: (a.) The histogram of the simulated TC intensity from 480 simulation runs that perturb the physical parameters simultaneously using LHS method. (b.) The histogram of the simulated TC intensity from 300 simulation runs that perturb five initial conditions simultaneously using LHS method. The horizontal resolution for (a) and (b) is 0.5 degree. (c.) The histogram of simulated TC intensity difference while horizontal resolution is changed from 1

degree to 0.5 degree. (d.) The histogram of simulated TC intensity difference while horizontal resolution is changed from 0.5 degree to 0.25 degree.

Fig. 4.9a shows that changes in model parameters causes a spread from about 15 $m \cdot s^{-1}$ to about 62 $m \cdot s^{-1}$. Fig. 4.9b shows that changes in model initial conditions cause uncertainty of about 20 $m \cdot s^{-1}$ in simulated TC intensity, (spread from about 45 $m \cdot s^{-1}$ to 65 $m \cdot s^{-1}$). Figs. 4.9c and 4.9d show that the peak uncertainty caused by model resolution lies about 20 $m \cdot s^{-1}$ and 6 $m \cdot s^{-1}$, respectively. These results indicate that parameter uncertainty is comparable to initial condition uncertainty and structural uncertainty (due to change of model resolution) in its effects on simulated TC intensity.

4.4.4. Exploration of GaSP

A surrogate model is a type of statistical model built to mimic the behaviors of numerical simulations and replace them for computational efficiency purpose. While they have been broadly applied in many fields, the question is whether a surrogate model enables one to capture the behavior of complicated atmospheric weather or climate models for simulations of individual dynamical systems. In Chapter 3, we have seen that the three surrogate models are generally quite capable of approximating the relationships between simulated TC output and the five chosen initial conditions. In examining the effects of parameter variability, the number of perturbed parameters is increased from 5 to 8, implying a higher dimension, and greater complexity. In addition, the physical processes that control the relationships between physical parameters and simulated TC characteristics is more complicated. In this part, we would like to explore whether the commonly used surrogate model, GaSP, is capable of mimicking the behaviors of complicated physical processes in AGCMs. The set of 480 ensemble runs generated

from perturbation of eight physical parameters provides an effective resource with which to answer this question.

In Appendix B, we introduce three methods to evaluate fitted results from surrogate model in detail. Here, we use the "cross validation method" to justify the performance of surrogate model in fitting the model output and input relationships. The model output remains the six TC characteristics: Intensity (MWS), precipitation (PRECT), LWCF, SWCF, LWP and IWP. The model input refers to the eight perturbed physical parameters: dmpdz, tau, C0_ocn, rkm, Dcs, ai, a2l, and c._rhminl.

Variables	Intensity	Precipitation	LWCF	SWCF	LWP	IWP
GaSP	0.05	0.11	0.04	0.06	0.13	0.31

Table 4.2: NRMSE calculated from the GaSP for (a). Intensity, (b). Total precipitation rate, (c).LWCF, (d). SWCF, (e) LWP and (f) IWP. The NRMSE is calculated from the cross validation method. GaSP: Gaussian Process Model, MARS:

Table 4.2 justifies how well GaSP fit these six characteristics. GaSP fit TC intensity, LWCF, and SWCF well. It can not fit TC precipitation, LWP and IWP reliably well, especially for IWP. This results suggest that the surrogate model has more difficulty in fitting hydrological variables in CAM.

4.5. Discussion and Conclusions

This study shows how the parameterized physical processes in cloud formation, convective development and moist turbulence impact the simulation of TC intensity, precipitation rate, LWCF, SWCF, LWP and IWP during the evolution from an initial vortex seed to an established tropical cyclone-like vortex in the Community Atmosphere Model 5.1.1 using the Reed-Jablonowski TC test case. Different aspects of simulated TCs are most sensitive to different

physical processes. The TC intensity and SWCF are most sensitive to the parcel fractional mass entrainment rate in deep convection. The TC precipitation rate is most sensitive to the time scale of consumption rate of CAPE. The LWCF, LWP and IWP are most sensitive to the precipitation efficiency. The response of simulated TC variables to changes in the most sensitive parameters are quantified, and it is notable that none of the model output variables exhibits a linear response to changes in parameter values. Many appear to be exponential, and one (the CAPE consumption rate vs. precipitation rate) is non-monotonic. Interactive effect among physical parameters plays a significant role in simulated TC precipitation and could enlarge the entire shape of distribution. It is also important to LWCF, SWCF and IWP, but mainly to contribute more extreme values. It does not affect the simulated TC intensity and LWP, which indicates that TC intensity is mainly controlled by dmpdz and LWP by C0_ocn. It further shows the parameter uncertainty on simulated TC intensity is comparable to the model initial condition uncertainty and model structural uncertainty. It is also showed that GaSP could not well fit the PRECT, LWP and IWP.

As the test case mimics the process of developing a pre-existing vortex seed into a tropical-cyclone like vortex in AGCMs, it is not possible to compare the simulated output with observations and thus we cannot directly determine which set of parameters leads to an improved simulation. For this reason, we do not conduct parameter optimization in this study. The 10 day integration time is long enough for parameterized physical processes to exert an influence on the evolution of the TC, however, it is not long enough for the climate state to respond to the change of physical parameters, which may alter the simulation of TCs. Nevertheless, the results presented here can help to instruct the configuration of full AGCMs when they are used to study either the statistics of global TCs or the properties of a single TC as in recent studies. It improves our understanding of how the model design of physical parameterizations affects the TC

evolution. Note that all of the results presented here were produced using grid spacing of $0.5^{\circ} \times 0.5^{\circ}$. We have tested the sensitivity of simulated output to changes in the most sensitive parameters using simulations with a grid spacing of $0.25^{\circ} \times 0.25^{\circ}$ and confirmed that the large uncertainty of simulated TCs due to parameter uncertainty is retained at finer resolution.

While we only explore the importance of parameterized processes on a TC simulation using a one-at-a-time sensitivity analysis method, our results show that improving TC simulation and prediction via parameter adjustment in AGCMs is promising. Even so, a given physical parameter that affects a particular aspect of a simulated TC may also exert a strong effect on another aspect. For example, the change of C0_ocn has a considerable effect on TC precipitation, SWCF, LWP and IWP, but to varying degree. This indicates that if a change of C0_ocn improves the representation of TC precipitation, it may worsen the representation of LWP. Changes in some parameterized processes have little impact on all characteristics of simulated TC such as a2l (moist entrainment enhancement parameter). Whether this should naturally be the case, or whether it is simply a result of parameterization design, is not clear due to insufficient understanding of the impact of physical processes on TC evolution from observations or high resolution modeling. Nevertheless, the current study sheds light on the following: (1) uncertainties in the set of sensitive parameters may be an important source of uncertainty in current simulation and future projections of simulated TCs in AGCMs, (2) it may be possible to improve the representation and forecasting of an individual TC in AGCMs using parameter estimation, and (3) nonlinear relationships between parameters and model output indicate that parameter estimation that employs linear perturbation methodologies may yield results that are incomplete and/or misleading.

CHAPTER 5

Conclusions

Numerical models built upon geophysical fluid equations are crucial tools in operational weather forecasting, climate research, and theory development of weather and climate systems. Sensitivity analysis/uncertainty quantification, which aims to assess various relationships between model input and output, is an important step for improving model performance, developing physical theory, simulating weather hazards, predicting climate extremes, etc. Atmospheric General Circulation Models (AGCMs) are one of the most complicated numerical tools. They include components with high levels of complexity such as a dynamical core that solves a set of geophysical fluid equations and thermodynamic equations, physical parameterization packages that approximate a wide variety of intricate physical processes (e.g. cloud, precipitation, turbulence, etc.), and radiative models that solve radiation transfer for hundreds of frequency spectra. AGCMs recently have played a paramount role in simulating tropical cyclones, and in predicting their future changes. Sensitivity analysis of simulated tropical cyclone characteristics to various model components in AGCMs can be very challenging, as both sensitivity analysis and AGCMs place a significant demand on computational resources. Isolating sources of model sensitivity impact for a particular dynamical system (e.g., tropical cyclone) in AGCMs is not straightforward either.

5.1 Summary

This dissertation explores the use of an idealized test case and surrogate models for a systematic sensitivity assessment of simulated tropical cyclone characteristics to changes in various model components in an AGCM. An idealized test case framework allows a focus on one particular dynamical system, and eliminates possible interactive effects or compensating error from other components of the model. It is computationally efficient, and detection of tropical cyclone feature is straightforward. Surrogate models are statistical models designed to approximate the numerical models with a much reduced computational burden. They are designed to replace the computationally expensive numerical model in assessing the relationships between model input and output. As such, the surrogate model enables a much more thorough exploration of model input-output relationships.

Chapter II presents a balanced tropical cyclone (TC) test case designed to improve current understanding of how Atmospheric General Circulation Model (AGCM) configurations affect simulated TC development and behavior. It consists of an analytic initial condition comprised of two independently balanced components. The first provides a vortical TC seed, while the second adds a planetary-scale zonal flow with height-dependent velocity and imposes background vertical wind shear (VWS) on the TC seed. The environmental flow satisfies the steady-state hydrostatic primitive equations in spherical coordinates and is in balance with other background field variables (e.g. temperature, surface geopotential). The evolution of idealized TCs in the test case framework is illustrated in 10-day simulations performed with the Community Atmosphere Model version 5.1.1 (CAM 5.1.1). Environmental wind profiles with different magnitudes, directions, and vertical inflection points are applied to ensure that the technique is robust to changes in the VWS characteristics. The well-known shear-induced intensity change and structural asymmetry in tropical cyclones are well captured. Sensitivity of TC evolution to small

perturbations in the initial vortex is also quantitatively addressed to validate the numerical robustness of the technique. It is concluded that the enhanced TC test case can be used to evaluate the impact of model choice (e.g. resolution, physical parameterizations) on the simulation and representation of TC-like vortices in AGCMs.

Chapter III This work proposes a strategy to use an uncertainty quantification framework to examine the multivariate sensitivities of an individual dynamical system to various atmospheric factors. It has the advantage of exploring multiple directions in the input space, and allowing nonlinear interactive effects among multiple parameters in a computationally affordable way. The idea is illustrated via exploration of the sensitivities of Atmospheric General Circulation Model (AGCM)-simulated tropical cyclones to model initial conditions. Specifically, a Latin Hypercube Sampling (LHS) method and an Extended Multivariate Adaptive Regression Splines (EMARS) algorithm are used to examine the response of cloud radiative forcing, cloud content, and precipitation rate in idealized AGCM-simulated tropical cyclones (TCs) to changes in TC initial conditions, including: initial vortex size, intensity, sea surface temperature, vertical lapse rate and mid-level relative humidity. Consistent with previous studies of TCs, the EMARS algorithm yields increases in TC intensity with increasing sea surface temperature and atmospheric temperature lapse rates. Nonlinearities and multi-variate relationships are further quantified and implications are discussed. The combined effect of RMW and MWS can play an extra role in affecting the TC intensity. Stronger TCs tend to be associated with larger LWCF and larger total precipitation rate tends to be associated with larger values of SWCF and larger cloud IWP.

Chapter IV advances the understanding of how parameterized physical processes affect the development of tropical cyclones (TCs) in the Community Atmosphere Model (CAM) using the

Reed-Jablonowski TC test case. It examines the impact of changes in 24 parameters across multiple physical parameterization schemes that represent convection, turbulence, precipitation and cloud processes. The one-at-a-time (OAT) sensitivity analysis method quantifies the relative influence of each parameter on TC simulations and identifies which parameters affect six different TC characteristics: intensity, precipitation, longwave cloud radiative forcing (LWCF), shortwave cloud radiative forcing (SWCF), cloud liquid water path (LWP) and ice water path (IWP). It is shown that TC intensity is mainly sensitive to the parcel fractional mass entrainment rate (dmpdz) in deep convection. A decrease in this parameter can lead to a change in simulated intensity from a tropical depression to a Category-4 storm. Precipitation and SWCF are strongly affected by three parameters in deep convection: tau (time scale for consumption rate of convective available potential energy), dmpdz and C0_ocn (precipitation coefficient). Changes in physical parameters generally do not affect LWCF much. In contrast, LWP and IWP are very sensitive to changes in C0_ocn. The changes can be as large as 10 (5) times the control mean value for LWP (IWP). Further examination of the response functions for the subset of most sensitive parameters reveals nonlinear relationships between parameters and most output variables, which suggest linear perturbation analysis may produce misleading results when applied to strongly nonlinear systems. Interactive effects among physical parameters plays a significant role in simulated TC precipitation and could enlarge the entire shape of the distribution. It is also important to LWCF, SWCF and IWP, but mainly contributes to the production of more extreme values. It does not affect the simulated TC intensity and LWP, which indicates that TC intensity is mainly controlled by dmpdz and LWP by C0_ocn. It further shows the parameter uncertainty on simulated TC intensity is comparable to the model initial condition uncertainty and model structural uncertainty due to change of horizontal resolution. It

is also showed that the popularly used surrogate model, GaSP, could not well fit the PRECT, LWP and IWP.

5.2 Accomplishments

5.2.1 Originality

The thesis works on a new field that will potentially shape the direction of future research and forecast of tropical cyclones. It proposed an innovative strategy to instruct the improvement of TC simulations in comprehensive AGCMs with specially designed idealized simulations and a robust statistical framework. It resulted in the first study of its kind, examining the sensitivities of an atmospheric dynamical system to environmental factors with an uncertainty quantification framework. In the process, the idealized tool was improved, resulting in a tropical cyclone test case that allows the existence of background vertical wind shear and simulation of its impact on tropical cyclone development in AGCMs. The implementation of the UQ strategy resulted in the first study that comprehensively examines the effect of changes in numerous parameterized physical processes on various characteristics of simulated TCs, including intensity, precipitation, and cloud content.

5.2.2 Significance and Contributions

The work provides a systematic evaluation of how model construction affects the simulation of TCs, including the initial conditions, large scale flow, physical parameterizations, and horizontal resolution. It contributes information to guide the development of next generation models. These results will shed light on the possibility of trending operational TC forecasting towards high resolution AGCMs.

The work also provides a successful example of a methodology that may be used to assess and improve the simulations of other dynamical systems (e.g. extratropical cyclones, jets, fronts, etc) in AGCMs, which will ultimately feedback to improvements in the overall performance of AGCMs. Finally, the statistical framework used in this study can be applied to general sensitivity problems not limited to AGCMs.

5.2.3 Interdisciplinary research

The techniques and ideas presented in this project were developed from the fields of atmospheric science, statistics and computer sciences. It combines the study of atmospheric modeling with high performance computing architecture and statistical learning techniques. The author joined several conferences and workshops from Statistical Methods for Atmospheric and Oceanic Sciences (STATMOS).

5.3 Future Work

We have assessed the sensitivity of simulated tropical cyclone characteristics to model initial conditions and physical parameters respectively. A natural extension of this work is exploration of whether interactive effects between changes in model initial conditions and changes in physical parameters play an important role in modifying simulated TC characteristics, and assessment of how surrogate models perform in figuring out such model input-output relationships. Whether an interaction between external uncertainty and internal uncertainty exists is an important question for real-world simulations, but has yet to be explored in any study that we are aware of. The results that either eliminate this possibility or confirm their interactive effect would bear scientific interest to the community. Using an idealized TC test case and LHS methods, we could investigate this problem. In the model design, we could select five parameters

in total, two from the model initial conditions: sea surface temperature and vertical lapse rate; the other three from the model physical parameters: for example dmpdz, tau, rkm. Using the LHS, these five parameters could be simultaneously perturbed to generate 300 or more numerical simulations. The output could then be compared with the distribution of output presented in Chapters 3 and 4. In the process, we could also evaluate the performance of GaSP, MARS and EMARS in fitting such relationships.

In addition, it would be interesting to explore the questions of when and which surrogate models could perform well in fitting the relationships from our ensemble simulations. In Chapter 3 and 4, we have evaluated the performance of GaSP for fitting TC intensity, PRECT, LWCF, SWCF, LWP and IWP from the LHS ensemble run that perturbs the five initial condition or eight physical parameters. We found it fails to reliably predict the response of PRECT, LWP and IWP in both cases. It would be interesting to explore the reasons behind this: why GaSP is not capable of fitting these three particular TC characteristics. There are also other surrogate models like Multiple Additive Regression Trees (MART; Friedman, 1999; Friedman and Meulman, 2003), and it would be interesting to test alternate surrogate models and assess whether any are able to successfully fit these three output variables. Such work will be beneficial for the development of statistical surrogate model, and their applications in model evaluation and development.

We have conducted all of our experiments paired with the Finite Volume (FV) dynamical core, which was the default dynamical core in the CAM when we started our project. Since that time, the developers of the NCAR CAM have chosen the Spectral Element (SE) as the model's default dynamical core. One benefit of the SE dynamical core is that it allows the use of adaptive mesh refinement and variable resolution in CAM, leading to very fine resolution in a portion of the full model grid. This is especially beneficial for hurricane simulations (Zarzycki et al. 2014a,b;

Zarzycki and Jablonowski 2014; Zarzycki and Jablonowski 2015). Thus, it would be interesting to examine the impact of parameterized physical processes on simulated TC characteristics paired with the SE dynamical core. The experiment design could be similar to what we have done in Chapter 4.

As all of our work is done in an idealized setup, these type of research bears its own scientific significance. Still, the final goal is to produce improved simulations of tropical cyclones in fully realistic coupled models. These idealized results can be used to instruct the tuning or setting of the full model simulations. Thus, another important future research activity will be to optimize a full model simulation that captures TC characteristics in concert with the full range of dynamical systems and Earth system interactions, and which could be compared with real observations. In this way, the results can be more effectively transferred from theory to real-world application.

APPENDICIES

Appendix A

Derivation of the analytic initial conditions

Implementation of the vertical wind shear in the current TC test case consists of adding an extra zonal wind term, as shown in Eq. (2.1), and then modifying the temperature field to maintain a gradient thermal wind balance. In essence, we impose an additional wind field in thermal wind balance on top of the initial conditions derived by Reed and Jablonowski (2011a), who assumed a zero base state wind field. Given a specified vertical profile, we seek the corresponding temperature distribution associated with the value of the vertical wind shear. In this case, vertical wind shear is essentially induced by the application of a horizontal temperature gradient. The derivation follows the methodology used by Jablonowski and Williamson (2006b) in their development of a baroclinic wave test case. The derivation uses pressure-based hybrid η vertical coordinate (Simmons and Burridge 1981), and starts from the adiabatic and frictionless primitive equations in spherical (λ, φ) coordinates. Note that if the surface pressure is constant and equal to the hybrid reference pressure $p_0 = p_s$, then $\eta = p / p_s$ resembles the $\sigma-$coordinate which is the case here.

The $u-$ and $v-$ momentum equations, as well as the hydrostatic equation in (λ, φ, η) coordinates are given by:

$$\frac{du}{dt} - \frac{uv\tan\varphi}{a} = -\frac{1}{a\cos\varphi}\left(\frac{\partial\Phi}{\partial\lambda} + R_d T\frac{\partial \ln p}{\partial\lambda}\right) + fv \qquad \text{(A.1)}$$

$$\frac{dv}{dt} + \frac{u^2\tan\varphi}{a} = -\frac{1}{a}\left(\frac{\partial\Phi}{\partial\varphi} + R_d T\frac{\partial \ln p}{\partial\varphi}\right) - fu \qquad \text{(A.2)}$$

$$\frac{\partial\Phi}{\partial\eta} = -\frac{R_d T}{p}\frac{\partial p}{\partial\eta} \qquad \text{(A.3)}$$

The Coriolis parameter is defined as $f = 2\Omega\sin\varphi$, and a is the radius of the earth. Note that T denotes the virtual temperature in this section as the air is moist. This is the same for the T in all following equations. The equation of state is:

$$p = \rho R_d T \qquad \text{(A.4)}$$

where ρ denotes the air density. In addition, the substantial derivative d/dt is defined as

$$\begin{aligned}\frac{d}{dt}() &= \frac{\partial}{\partial t}() + (\vec{v}\cdot\nabla)() \\ &= \frac{\partial}{\partial t}() + \frac{u}{a\cos\varphi}\frac{\partial}{\partial\lambda}() + \frac{v}{a}\frac{\partial}{\partial\varphi}() + \dot{\eta}\frac{\partial}{\partial\eta}().\end{aligned}$$

For $p_s = p_0 = 1000$ hPa with $p = \eta p_s$, the associated form of the hydrostatic equation is:

$$\frac{\partial\Phi^*}{\partial\eta} = -\frac{R_d T^*}{\eta}\ , \qquad \text{(A.5)}$$

where Φ^* and T^* indicate the deviations from the horizontal mean geopotential and temperature fields that correspond to the added zonal wind.

The goal is to derive an analytic, steady-state balanced initial background T distribution ($T = \langle T(\eta) \rangle + T^*(\lambda, \varphi, \eta)$). Four steps are needed.

(1) Choose a nondivergent wind field u and v and a constant p_s.

$$u = u_0 \cos\varphi(\tanh \eta_v + 1.0) + u_1 \cos\varphi$$
$$v = 0 \qquad \text{(A.6)}$$
$$p_s = 1000 \text{ hPa}$$

η_v is defined as $\eta_v = 6*(1-\eta) - 3.0$. Thus, $\eta_v' = \dfrac{\partial \eta_v}{\partial \eta} = -6$.

u_0 determines the amplitude and direction of the wind profile.

(2) Choose the horizontally averaged temperature profile $\langle T(\eta) \rangle$. This is done in height (z) coordinates using:

$$\langle T(\eta) \rangle = T_0 - \Gamma z \qquad \text{(A.7)}$$

Thus, the total temperature profile is:

$$T(\lambda, \varphi, \eta) = \langle T(\eta) \rangle + T^*(\lambda, \varphi, \eta) = T_0 - \Gamma z + T^*(\lambda, \varphi, \eta) \quad \text{(A.8)}$$

Where $z = T_0(1 - \eta^{R_d \Gamma / g}) / \Gamma$. T_0 is the sea surface temperature in our case. The task now is to derive $T^*(\lambda, \varphi, \eta)$, which we obtain from $\Phi^*(\lambda, \varphi, \eta)$ based on (A.5).

(3) Derive $\Phi^*(\lambda, \varphi, \eta)$.

The derivation starts from the $v-$momentum equation (A.2). A steady-state solution with $dv/dt = 0$ is sought. In case of a constant p_s field $\partial \ln p / \partial \varphi$ vanishes on constant $\eta-$ surfaces. Simplifying Eq. A.2, we get:

$$\frac{1}{a} \frac{\partial \Phi^*}{\partial \varphi} = -u(2\Omega \sin\varphi + \frac{u}{a} \tan\varphi) \qquad \text{(A.9)}$$

Insert the wind profile $u = u_0 \cos\varphi(\tanh\eta_v + 1.0) + u_1 \cos\varphi$ into (A.9), and then integrate analytically over φ. Let $\mathrm{X} = u_0(1+\tanh\eta_v) + u_1$, then $u = \mathrm{X}\cos\varphi$. The integration leads to:

$$\Phi^*(\lambda,\varphi,\eta) = \frac{1}{4}(2\mathrm{X}a\Omega + \mathrm{X}^2)\cos(2\varphi) + \Phi_0(\eta) \quad \text{(A.10)}$$

Recall that: $\eta_v = 6(1-\eta) - 3.0$ and $\mathrm{X} = u_0(1+\tanh\eta_v) + u_1$.

$\Phi_0(\eta)$ is a level-dependent integration constant.

Use the condition that the area-mean of Φ^* vanishes:

$$\frac{1}{4\pi}\int_0^{2\pi}\int_{-\frac{\pi}{2}}^{\frac{\pi}{2}} \Phi^*(\lambda,\varphi,\eta)\cos\varphi d\varphi d\lambda = 0 \quad \text{(A.11)}$$

This results in the expression

$$\Phi_0(\eta) = -\frac{1}{12}(2\mathrm{X}a\Omega + \mathrm{X}^2) \quad \text{(A.12)}$$

Thus, we obtain:

$$\Phi^*(\lambda,\varphi,\eta) = (\frac{1}{4}\cos(2\varphi) - \frac{1}{12})(2\mathrm{X}a\Omega + \mathrm{X}^2) \quad \text{(A.13)}$$

(4) Finally, the temperature deviations $T^*(\lambda,\varphi,\eta)$ are analytically derived using the hydrostatic equation (Eq.A.5) and the newly derived expression for Φ^*:

$$T^*(\lambda,\varphi,\eta) = -\frac{\eta}{R_d}\frac{\partial \Phi^*(\lambda,\varphi,\eta)}{\partial \eta}$$
$$= -\frac{\eta}{R_d}(\frac{1}{4}\cos(2\varphi) - \frac{1}{12})(2a\Omega\frac{\partial \mathrm{X}}{\partial \eta} + 2\mathrm{X}\frac{\partial \mathrm{X}}{\partial \eta}) \qquad \text{(A.14)}$$

Inserting $\mathrm{X} = u_0(1+\tanh\eta_v) + u_1$ and $\frac{\partial \mathrm{X}}{\partial \eta} = \frac{\partial \mathrm{X}}{\partial \eta_v}\frac{\partial \eta_v}{\partial \eta} = -6u_0(1-\tanh^2\eta_v)$ into A.14 results in $T^*(\lambda,\varphi,\eta)$:

$$T^*(\lambda,\varphi,\eta) = \frac{12\eta}{R_d}u_0(\frac{1}{4}\cos 2\varphi - \frac{1}{12})(1-\tanh^2\eta_v)(a\Omega + u_0(\tanh\eta_v + 1.0) + u_1) \text{ (A.15)}$$

Thus, the temperature is:

$$T(\lambda,\varphi,\eta) = T_0 - \Gamma z + T^*(\lambda,\varphi,\eta), \text{ where } \eta = \frac{p}{p_s}, \text{ and } z = \frac{T_0}{\Gamma}(1-\eta^{\frac{R_d\Gamma}{g}}) \text{ (A.16)}$$

All derived fields describe the background flow in which a vortex seed is embedded. The corresponding u, v, T, p and q of the initial vortex seed remain the same as those in Reed and Jablonowski (2011a). The tangential velocity of the vortex seed is consistent with Eq.(17) in RJ2011a and the way to compute u and v is the same as that shown in Eq.(22) and Eq.(23) of RJ2011a. The temperature field defining the vortex seed is in Eq.(15), the pressure field is in Eq.(7), and the specific humidity q is specified in Eq.(1) of RJ2011a. Consider a unidirectional westerly vertical profile as an example (note: $u_1 = 0$ for this type of wind profile), the background u, v, T, p and q fields are:

(1) $u = u_0\cos\varphi(\tanh\eta_v + 1.0),\ v = 0, \textit{where}\ \eta_v = 6(1-\eta) - 3.0;$

(2) $T(\varphi,\eta) = T_0 - \Gamma z + \frac{12\eta}{R_d}(\frac{1}{4}\cos 2\varphi - \frac{1}{12})(1-\tanh^2\eta_v)(u_0 a\Omega + u_0^2(\tanh\eta_v + 1.0))$;

Where $T_0 = SST$, and the sea surface temperature (SST) is set to a constant 302.15 K everywhere (zero horizontal temperature gradient at surface). The horizontal temperature gradient increases with height, and reaches its maximum in the mid-troposphere where the wind shear is greatest. When the wind shear approaches zero in the upper troposphere, the horizontal temperature gradient diminishes to zero;

(3) $\Phi_s(\lambda,\varphi) = (\frac{1}{4}\cos(2\varphi) - \frac{1}{12})(2u_0(\tanh(-3.0)+1.0)a\Omega + (u_0(\tanh(-3.0)+1.0))^2)$

(4) $p = \eta p_s$, where p_s is surface temperature;

(5) q is the same as (Eq.(1)) in Reed and Jablonowski (2011a);

(6) Tropopause height remains 15 km everywhere.

Appendix B
Validation of EMARS

We used three methods to evaluate EMARS. The root mean square error (RMSE) is used to measure how well EMARS fits the CAM model in simulating the relationships between tropical cyclone characteristics and model initial conditions. Let y denote the output from simulated the CAM model and let $\hat{y}$ be the output calculated from the EMARS model. The RMSE can then be defined as,

$$RMSE = \sqrt{\frac{1}{n}\sum_i (\hat{y}_i - y_i)^2} \,/\, (\frac{1}{n}\sum_i y_i)$$

RMSE in this case is the proportion of mean square error to the mean value over the ensemble of CAM simulations. In the first method, we used all 300 model intergrations to build EMARS repeatedly for each output variable. That is:

$$\widehat{y}_{MWS} = \hat{f}_1(RMW, MWS, GAMMA, SST, 500hPa - RH)$$

$$\widehat{y}_{PRECT} = \hat{f}_2(RMW, MWS, GAMMA, SST, 500hPa - RH)$$

$$\widehat{y}_{LWCF} = \hat{f}_3(RMW, MWS, GAMMA, SST, 500hPa - RH)$$

$$\widehat{y}_{SWCF} = \hat{f}_4(RMW, MWS, GAMMA, SST, 500hPa - RH)$$

$$\widehat{y}_{LWP} = \hat{f}_5(RMW, MWS, GAMMA, SST, 500hPa - RH)$$

$$\widehat{y}_{IWP} = \hat{f}_6(RMW, MWS, GAMMA, SST, 500hPa - RH)$$

After the functions $\hat{f}_{MWS}$, $\hat{f}_{PRECT}$, $\hat{f}_{LWCF}$, $\hat{f}_{SWCF}$, $\hat{f}_{LWP}$ and $\hat{f}_{IWP}$ are built from the 300 CAM simulations, the estimated MWS, PRECT, LWCF, SWCF, LWP and IWP are calculated and compared to the model simulated MWS, PRECT, LWCF, SWCF, LWP and IWP. Figure B1 shows the comparisons between the CAM model and the EMARS emulators. Generally speaking, EMARS provides a close fit to the CAM output. The root mean square error for MWS is 3% of the mean value of the 300 simulated intensity samplings. This variable is also small for

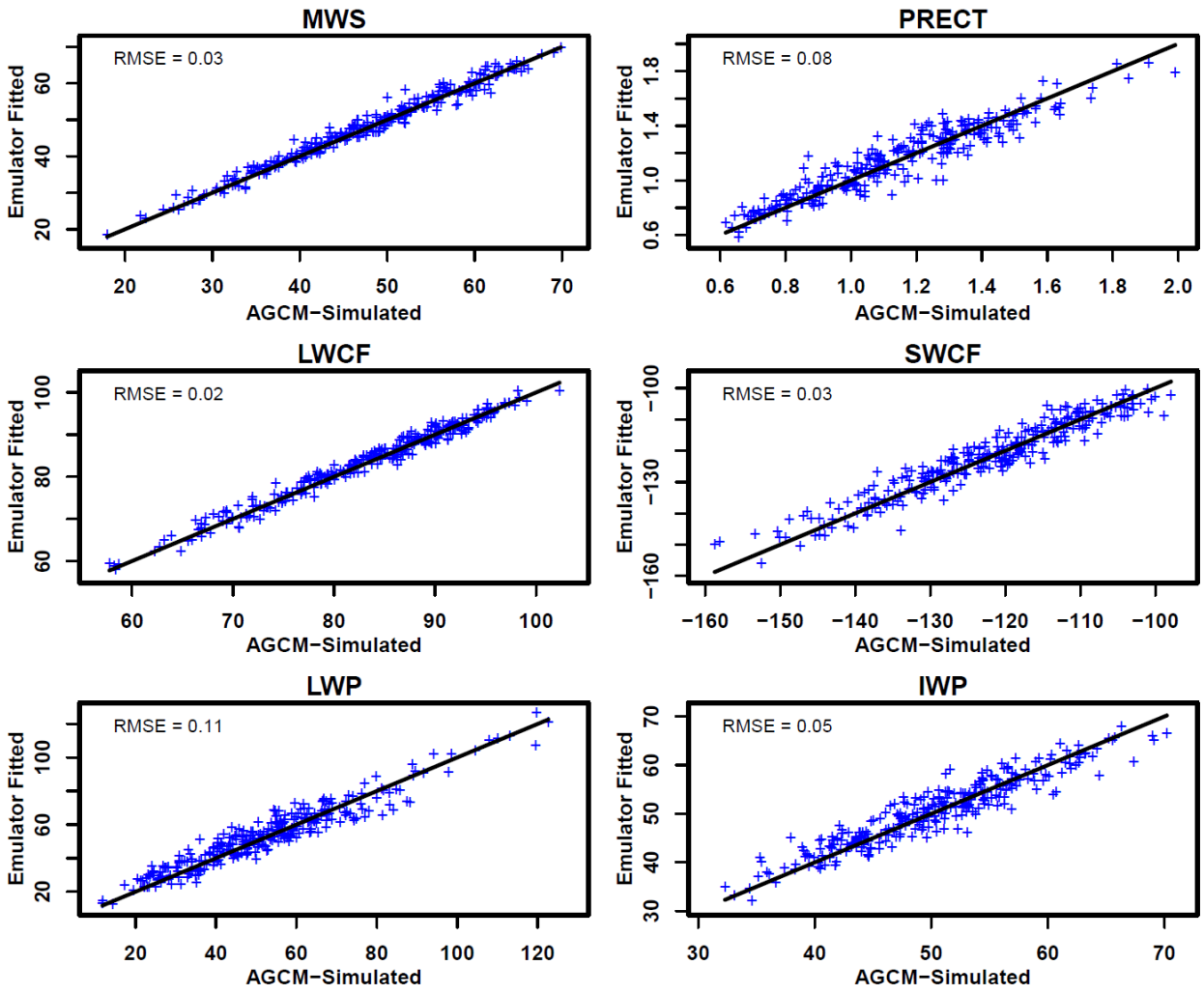

Figure B 1: Fitted output variables using EMARS emulator compared with the simulated physical fields from ensemble runs. The data shown are time averaged over days 9-10, the mature phase of TCs. Each variable is retrieved by weighted area average over the tropical cyclone region.

PRECT, LWCF, SWCF and IWP. The error from EMARS is larger for LWP (which is 11% of the mean value), indicating that EMARS did not capture the relationships between LWP and the five model initial conditions as well as it did for MWS, PRECT, LWCF, SWCF and IWP.

In the second method, we used the first 280 sampling points to build EMARS, then used EMARS to predict the remaining 20 points. The predicted values are compared with CAM simulated values, and the comparison is shown in Figure B2. The results are consistent with what was shown in Figure B1. EMARS does a good job constructing the relationships between MWS, PRECT, LWCF, SWCF, IWP and the five input variables.

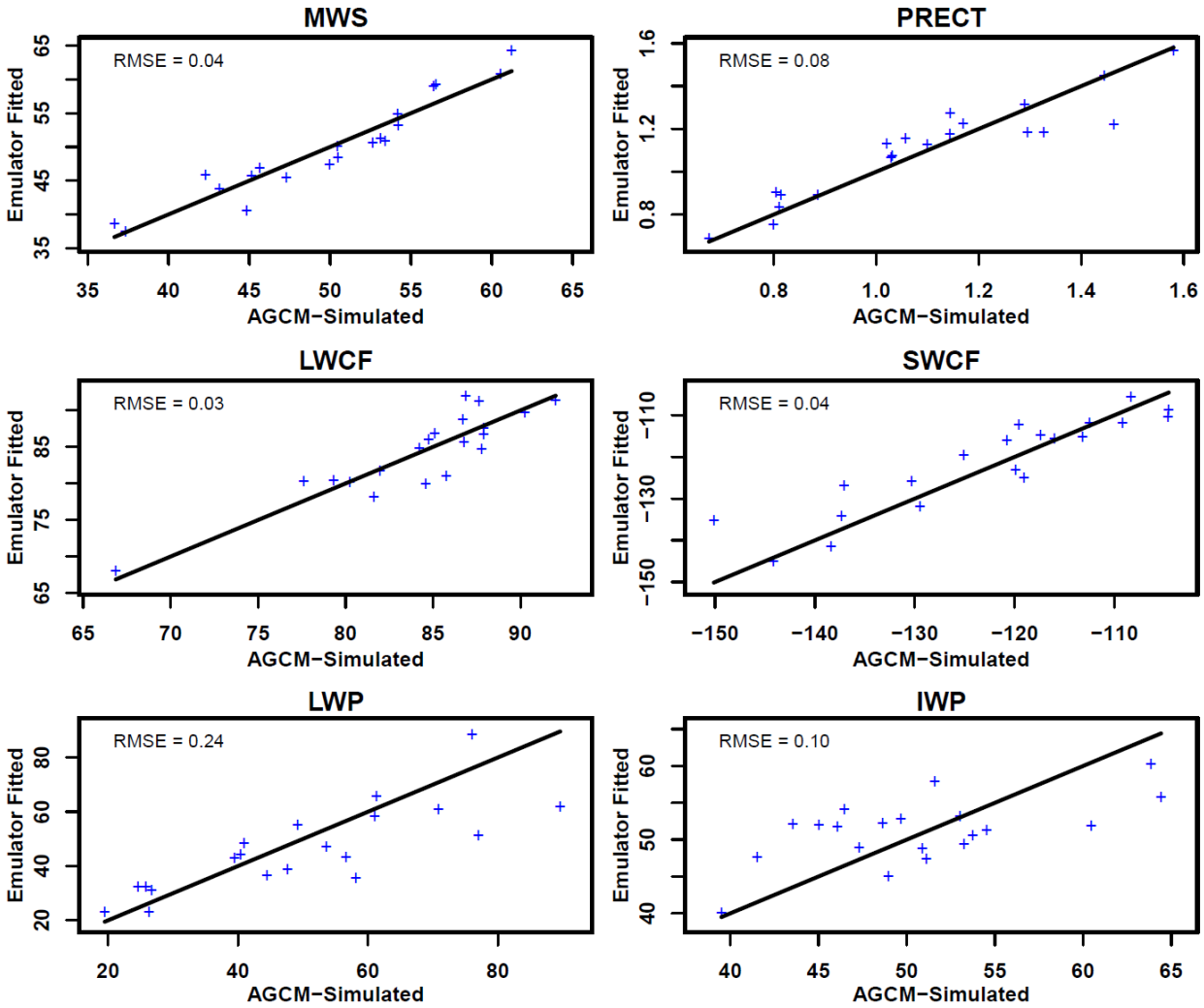

Figure B 2: Predicted 20 subset points from EMARS versus the actual values. 300 samplings are run and 280 samplings are used for building the EMARS models. The model is then used to predict the last 20 points. These predicted values are compared with the 20 actual values as shown.

LWP is again not fit as well as the others. In the third method, we use cross validation analysis. Consider TC intensity (MWS) as an example. In each time of several trials, we used 299 sampling points to construct the EMARS fit, then predicted the remaining one point. We did this routinely 300 times starting from sample (simulation) 1 and proceeding through 300. The 300 predicted values are then compared with the simulated 300 values. The cross validation analysis is conducted for all six variables. Figure B3 shows the results. The conclusions from Figure B3

are consistent with those shown in Figure B1 and Figure B2. EMARS performs well for MWS, PRECT, LWCF, SWCF, IWP but returns a poorer fit for LWP.

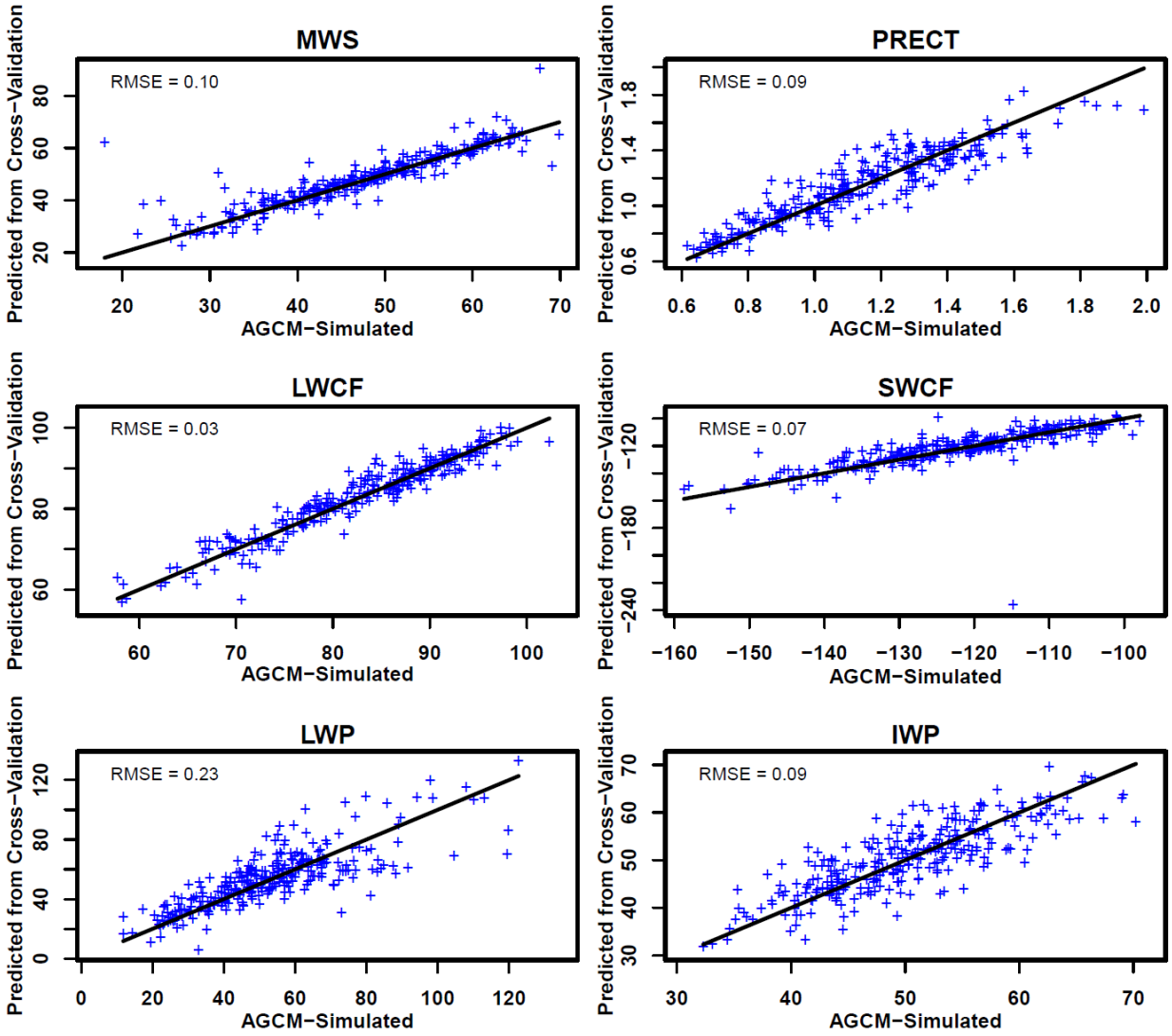

Figure B 3: Predicted values from cross-validation analysis versus the actual values of (a). MWS, (b). total precipitation rate, (c). LWCF, (d). SWCF, (e). LWP and (f). IWP.

The reason that EMARS does not perform well for LWP might be that the relationship between LWP and the five initial conditions is much more complicated. We further compare the performance of EMARS with other two popularly used surrogate model: Gaussian Process Model and MARS, and fit the relationship between TC intensity and SST (Figure B4). The R package for Gaussian Process Model is called "GPfit" from B. MacDonald, H. Chipman, and P.

Ranjan. The comparison shows that EMARS generally does a better job than MARS and GaSP, primarily at large values of SST.

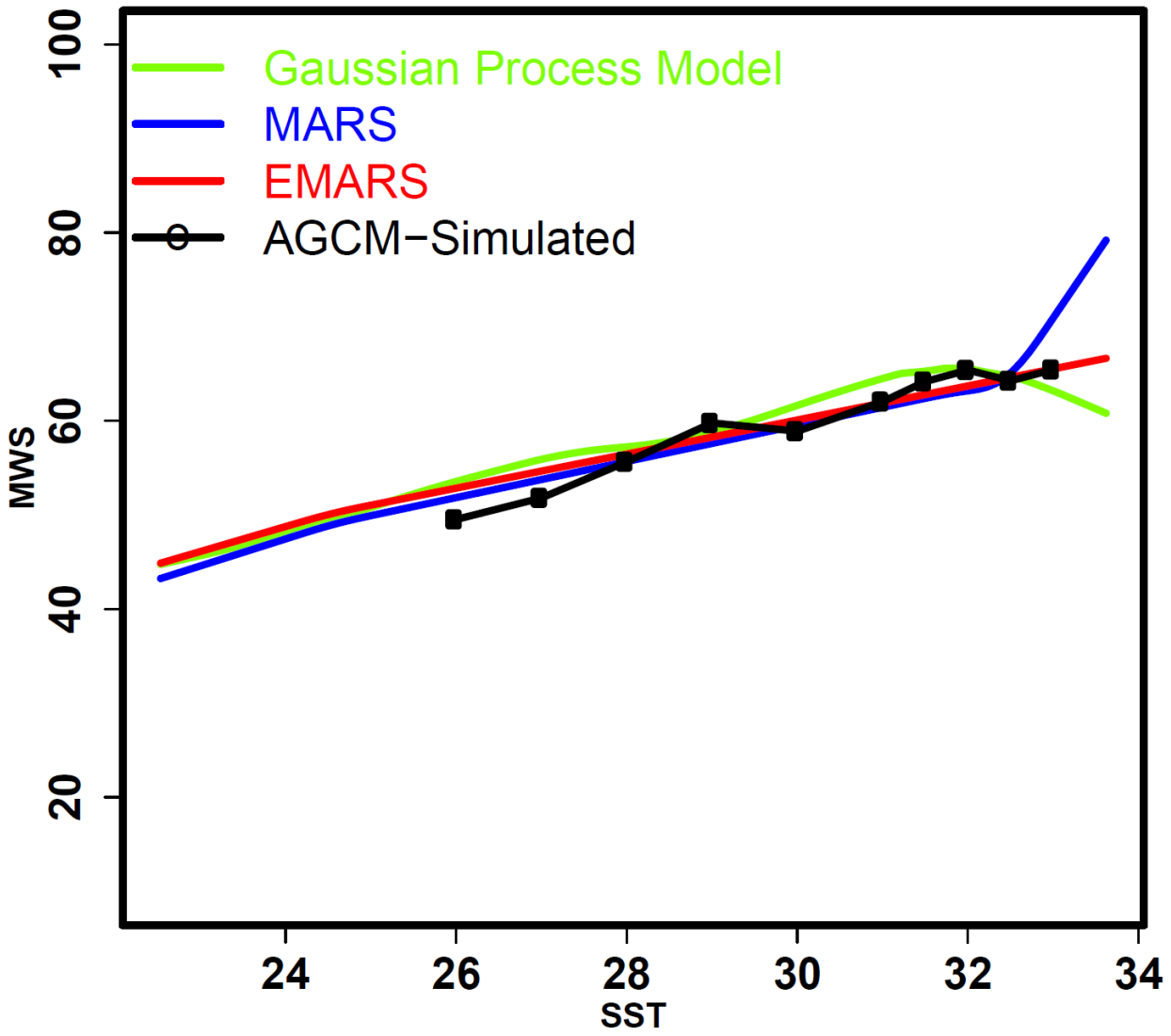

Figure B 4: Comparison among three surrogate model on fitting the relationship between TC intensity and SST. The three surrogate model are Gaussian Process Model (GaSP; B. MacDonald, H. Chipman, and P. Ranjan), MARS, and EMARS.

The conclusions from Figure B1, B2, B3 and B4 provide solid confidence that we can construct relationships between simulated TC characteristics and model initial conditions using EMARS.

Appendix C

Physical explanation of the 24 selected parameters in CAM 5.1.1

We examined 24 parameterized physical processes in 5 schemes: the Zhang-McFarlane (ZM) deep convection scheme (Zhang and McFarlane 1995; Ritcher and Rasch 2008), the University of Washington (UW) shallow convection scheme (Bretherton et al. 2004; Park and Bretherton 2009), the UW moist turbulence scheme (Bretherton and Park 2009), Morrison-Gettelman (MG) the two moment cloud microphysics parameterization (Morrison and Gettelman 2008; Gettelman et al. 2010) and the cloud macrophysics scheme (Neale et al. 2010). Among them, 8 parameters are selected from the deep convection scheme, 5 parameters are from the UW shallow convection scheme, 8 parameters are from the MG cloud microphysics scheme, 1 parameter is from the UW moist turbulent scheme and 2 are from the cloud macrophysics. In this supplemental material, we document each parameter, noting the scheme in which it is contained, and explaining the associated physical process (es).

1. Deep convection scheme

In CAM5, the deep convection parameterization is based on the work of Zhang and McFarlane (1995) and modified with the addition of convective momentum transports by Richter and Rasch (2008) and a modified dilute plume calculation following Raymond and Blyth (1986,1992). 8

tunable parameters are selected from this scheme. They are C0_ocn, ke, alfa, dmpdz, tau, capelmt, momcu and momcd.

C0_ocean (C_0_ocn): Deep convective precipitation efficiency over ocean

This is the autoconversion coefficient over ocean in the CAM deep convection scheme, and determines the conversion from cloud liquid water to rainwater in the updraft. The conversion from cloud liquid water to rain water (Rr) is represented by the empirical formulation of Lord et al. (1982),

$R_r = C_0 M_u l$ (eq.1)

Where *Mu* is the updraft mass flux, C_0 is the conversion coefficient, and *l* is the cloud water content.

ke (K_e): Tunable evaporation efficiency of precipitation.

An evaporation formula following Sundqvist (1988), has been employed to evaporate some precipitation directly to the grid-scale environment as it makes its way to the surface

$E_k = K_e(1-RH_k)R_k$ (eq.2)

where R is the total precipitation flux at model layer k, RH is the relative humidity of the environment, Ke is the evaporation efficiency, and E is the corresponding evaporation in that layer.

alfa (α): Maximum cloud downdraft mass flux fraction (fraction)

Convective scale downdrafts are induced and fueled by the rainwater evaporation when there is precipitation produced in the updrafts. The strength of the downdraft flux is controlled by a proportionality factor α, which is derived based on the precipitation produced in the updrafts (PCP) and the evaporation in downdrafts (EVP), as shown:

$$\alpha = \alpha_0 \frac{PCP}{PCP + EVP} \text{ (eq. 3)}$$

Such a relationship indicates that there is no downdraft if no precipitation is produced. It also ensures that evaporation in the downdraft does not exceed a fraction ($\alpha_0 = 0.1$) of the total precipitation produced within the updrafts.

dmpdz (PE_ocn): Parcel fractional mass entrainment rate over ocean (aqua-planet set up in our simulations). It denotes the entrainment rate from environmental air to the convective plume.

tau (τ): CAPE consumption time scale. In the deep convective scheme, it is assumed that the moist convection occurs only when there is CAPE consumption.

capelmt ($CAPE_0$): Threshold value of CAPE for deep convection.

The closure condition used in the ZM deep convection scheme is based on the concept that cumulus convection consumes the CAPE at a certain time rate. The cloud-base upward mass flux (M_b) is calculated as shown by:

$$M_b = \frac{CAPE - CAPE_0}{\tau F} \text{ (eq. 4)}$$

Where F is the $CAPE$ consumption rate per unit updraft mass flux at the cloud base, $CAPE_0$ is the threshold for deep convection, and τ is a prescribed time scale during which $CAPE$ in excess of $CAPE_0$ is consumed by convection.

momcu(C_u): coefficient controls the updraft convective momentum transport (CMT).

momcd(C_d**):** coefficient controls the downdraft convective momentum transport (CMT).

Richter and Rasch (2008) first incorporate momentum transport in convection scheme and they found that convective momentum transport changes the Coriolis torque and thus affect tropospheric climate. The convective momentum transport is represented following (Gregory et al. 1997) as:

$$P_G^u = -C_u M_u \frac{\partial \bar{v}}{\partial p} \quad \text{(eq. 5)}$$

$$P_G^d = -C_d M_d \frac{\partial \bar{v}}{\partial p} \quad \text{(eq. 6)}$$

Where C_u and C_d are tunable parameters. The value of C_u and C_d control the strength of updraft and downdraft convective momentum transport respectively. As these coefficients increase, so do the pressure gradient terms, and convective momentum transport decreases. The addition of the pressure gradient term reduces the difference between in-cloud and environmental velocities, hence reducing the vertical momentum transport.

2. University of Washington Shallow Convection Scheme

Uwshcu_rpen(r_{pen}**)**: Penetrative entrainment efficiency.

This parameter regulates the ratio of penetrative entrained air mass to the air mass detrained from cumulus updrafts in the overshooting zone above the level of neutral buoyancy (LNB).

The rate of lateral mixing in the overshooting zone is specified as:

$\varepsilon_i = r_{pen}\varepsilon_0$ (eq. 7)

ε_0 is the fractional mixing rate. r_{pen}=10.0 is an empirical penetrative mixing enhancement factor parameter that crudely accounts for differences between penetrative and lateral mixing and is chosen to optimize the model simulation of the stratus to trade-cumulus transition.

criqc($q_{c,\max}$): Maximum cumulus updraft condensate.

A crude precipitation sink for the updraft total water, which removes all updraft cloud water in excess of an arbitrary critical value $q_{c,\max} = 1g\ kg^{-1}$ and increases the updraft liquid water potential temperature accordingly. If the cloud condensate mixing ratio exceeds $q_{c,\max} = 1g\ kg^{-1}$, all the excessive condensate is converted into precipitation.

kevp (K_e): evaporative efficiency.

UWShCu treats evaporation of convective precipitation above cloud base, as in ZM deep convection scheme, which relates the vertical profile of rain evaporation rate E (s^{-1}) to the vertical profiles of grid-mean relative humidity RH and the precipitation flux R ($kg\ m^{-2}\ s^{-1}$):

$E = K_e(1-RH)R^{1/2}$ (eq. 8)

$K_e = 0.2\times10^{-5}[(kg\ m^{-2}\ s^{-1})^{-1/2}s^{-1}]$

Comparison of vertical profiles of precipitation flux with large eddy simulations (LES) based on an ongoing Global Cloud System Study (GCSS) precipitating trade cumulus case suggests that the coefficient K_e used in the deep convection scheme is also adequate for shallow cumulus.

rkm(c): Determine the amount of air that is involved in buoyancy-sorting c =8.0 for which the cumulus layer was only 1.5 km deep.

By decreasing c , one can make UWShCu resemble a deep convection scheme. To avoid competition between UWShCu and a separate deep convection scheme, it is therefore advisable not decrease c below 4.

aumax ($a_{u,\max}$): Maximum core updraft fraction

In UWShCu, the shallow cumulus core updraft fraction is not allowed to exceed $a_{u,\max} = 0.1$ at any level. Since cumulus updraft fractional area is about twice of the core updraft fractional area, cumulus updraft fractional area should not exceed 0.2 by this constraint. Range is 0.05-0.15. If the cumulus core updraft fraction exceeds 0.15, the convection is arguably better represented as a stratocumulus layer and should be handled by the moist turbulence scheme.

3. Morrison-Gettelman two moment cloud microphysics

Dcs(D_{cs}): The threshold size separating cloud ice from snow. This parameter works in conversion of cloud ice to snow. When the size of cloud ice is greater than Dcs, it is then treated as snow.

ai(a_i **)**: Empirical fall-speed parameter for cloud ice. It determines the cloud ice particle terminal fall speed. Larger ai leads to larger ice particle terminal fall speed.

$V_i = a_i D^b$ (eq. 9)

as(a_s **)**: Empirical fall-speed parameter for snow. It determines snow terminal fall speed. Larger ai leads to larger snow terminal fall speed.

$V_s = a_s D^b$ (eq. 10)

cdnl: Cloud droplet number limiter. This is the maximum number of cloud droplets allowed in the model domain. It is a prognosed variable.

eii: Collection efficiency aggregation ice. Snow is accreted from cloud ice particle via continuous collection. This is the collection efficiency for collisions between cloud ice and snow. Larger eii means that cloud ice particle has larger chance to form snow when they are collided.

qcvar (ν): Inverse relative variance of sub-grid cloud water. In the MG two moment cloud microphysics, the probability density function (PDF) of in-cloud cloud water follows a gamma distribution function. This is the parameter in the PDF function. Larger qcvar typically comes with smaller autoconversion rate, immersion freezing and rain accretion.

wsubimax: Maximum subgrid vertical velocity for ice nucleation. It is a critical vertical velocity for ice nucleation.

wsublmin: Minimum subgrid vertical velocity for liquid nucleation. It is a critical vertical velocity for liquid nucleation.

4. University of Washington moist turbulence scheme

Only one parameter is tunable in this scheme.

a2l: moist entrainment enhancement parameter. It is relevant to entrainment efficiency, which is affected by mixtures of cloud-top and above-inversion air. At the convective layer (CL) top, the cooling promotes the sinking of mixtures into the CL, enhancing entrainment. At the base, the cooled mixtures tend to sink away from the CL, so entrainment is not enhanced. In other words, if a2l is larger, the entrainment is better enhanced.

5. Cloud macrophysics

In cloud macrophysics, stratus cloud fraction is parameterized as a sum of *Relative Humidity (RH)-based* and *Stability-based* cloud fractions. The RH-based stratus fraction is a quadratic function of grid-mean RH.

cldfrc_rhminh: Minimum relative humidity for high stable clouds

In CAM5, the liquid stratus fraction is a function of grid-mean RH over water. Only when this RH is larger than the critical RH (cldfrc_rhminh), high stable liquid stratus (above 400 hPa) is formed. The cldfrc_rhminh is externally specificed and used as a tuning parameter.

cldfrc_rhminl: Minimum relative humidity for low stable clouds.

Similar to cldfrc_rhminh, however, it is the critical relative humidity for low stable clouds (below 700 hPa).

BIBLIOGRAPHY

BIBLIOGRAPHY

Abarca, S. F., and K. L. Corbosiero, 2011: Secondary eyewall formation in WRF simulations of hurricanes Rita and Katrina (2005), *Geophys. Res. Lett.,* **38,** L07802.

Aiyyer, A. R., and C. Thorncroft, 2006: Climatology of vertical wind shear over the tropical Atlantic. *J. Climate,* **19,** 2969–2983.

Atlas, R., O. Reale, B.-W. Shen, S.-J.Lin, J.-D. Chen, W. Putman, T. Lee, K.-S.Yeh, M. Bosilovich, and J. Radakovich 2005, Hurricane forecasting with the high-resolution NASA finite volume general circulation model, *Geophys. Res. Lett.,* **32,** L03807.

Bacmeister, J. T., M. F. Wehner, R. B. Neale, A. Gettelman, C. Hannay, P. H. Lauritzen, Julie M. Caron, and John E. Truesdale, 2014: Exploratory high-resolution climate simulations using the Community Atmosphere Model (CAM). *J. Climate*, **27,** 3073–3099.

Bassill, N. P., 2014: Accuracy of early GFS and ECMWF Sandy (2012) track forecasts: Evidence for a dependence on cumulus parameterization, *Geophys. Res. Lett., 41*, 3274–3281.

Bell, M. M., and M. T. Montgomery, 2008: Observed structure, evolution, and potential intensity of category 5 hurricane Isabel (2003) from 12 to 14 September. *Mon. Wea. Rev.,* **136**, 2023-2046.

Bengtsson, L., H. Bottger, and M. Kanamitsu, 1982: Simulation of hurricane-type vortices in a general circulation model. *Tellus,* **34,** 440-457.

Bengtsson, L., M. Botzet, and M. Esch, 1995: Hurricane-type vortices in a general circulation model. *Tellus,* **47A,** 175-196.

Bengtsson, L., K. I. Hodges, and M. Esch, 2007a: Tropical cyclones in a T159 resolution global climate model: Comparison with observations and re-analyses. *Tellus*, **59A**, 396–416.

Bengtsson, L., K. I. Hodges, and M. Esch, 2007b: How tropical cyclones may change in a warmer climate? *Tellus,* **59A**, 539-561.

Bender, M. A., 1997: The effect of relative flow on the asymmetric structure of the interior of hurricanes. *J. Atmos. Sci.*, **54**, 703-724.

Bender, M., T. Knutson, R. Tuleya, J. Sirutis, G. Vecchi, S. T. Garner, and I. Held, 2010: Modeled impact of anthropogenic warming on the frequency of intense Atlantic hurricanes. *Science*, **327**, 454–458.

Berner, J., S.-Y. Ha, J. P. Hacker, A. Fournier, C. Snyder, 2011: Model uncertainty in a mesoscale ensemble prediction system: stochastic versus multiphysics representations. *Mon. Wea. Rev.*, **139**, 1972–1995.

Black, M. L., J. F. Gamache, F. D. Marks Jr., D. E. Samsury, and H. E. Willoughby, 2002: Eastern Pacific hurricanes Jimena of 1991 and Olivia of 1994: The effect of vertical wind shear on structure and intensity. *Mon. Wea. Rev.*, **130,** 2291-2312.

Blackburn, M., and B. J. Hoskins, 2013: Context and aims of the aqua-planet experiment, *J. Meteorol. Soc. Jap.*, **91A**, 1-15, ISSN 2186-9057.

Bretherton, C. S., J. R. McCaa, and H. Grenier, 2004: A new parameterization for shallow cumulus convection and its application to marine subtropical cloud-topped boundary layers. Part I: description and 1D results. *Mon. Wea. Rev.*, **132**, 864–882.

Bretherton, C. S., and S. Park, 2009: A new moist turbulence parameterization in the Community Atmosphere Model. *J. Climate*, **22,** 3422–3448.

Broccoli, A.J., and S. Manabe, 1990: Can existing climate models be used to study anthropogenic changes in tropical cyclone climate? *Geophys. Res. Lett.*, **17,** 1817-1920.

Burpee, R. W., and M. L. Black, 1989: Temporal and spatial variations of rainfall near the centers of two tropical cyclones. *Mon. Wea. Rev.*, **117,** 2204-2218.

Camargo, S. J., and S. E. Zebiak, 2002: Improving the detection and tracking of tropical cyclones in atmospheric general circulation models. *Wea. Forecasting*, **17**, 1152–1162.

Camargo, S. J., 2013: Global and regional aspects of tropical cyclone activity in the CMIP5 models. *J. Climate*, **26**, 9880–9902.

Chauvin, F., J.-F. Royer, and M. Deque, 2006: Response of hurricane-type vortices to global warming as simulated by arpege-climat at high resolution. *Climate Dynamics*, **27 (4),** 377-399.

Chan, J. C.-L., 1984: An observational study of the physical processes responsible for tropical cyclone motion. *J. Atmos. Sci.*, **41**, 1036–1048.

Chen, S. S., J. A. Knaff, and F. D. Marks, 2006: Effects of vertical wind shear and storm motion on tropical cyclone rainfall asymmetries deduced from TRMM. *Mon. Wea. Rev.*, **134,** 3190–3208.

Chen, Q., M. Gunzburger, and T. Ringler, 2011: A scale-invariant formulation of the anticipated potential vorticity method, *Mon. Wea. Rev.*, **139**, 2614–2629.

Cline, I. M., 1926: Tropical Cyclones. MacMillan, 301 pp.

Collins, M., B. Booth, B. Bhaskaran, G. Harris, J. Murphy, D. Sexton, and M. Webb, 2011: Climate model errors, feedbacks and forcings: a comparison of perturbed physics and multi-model ensembles. *Climate Dynamics*, **36**, 1737–1766.

Cordeira, J., 2010: Tropical-extratropical interactions conducive to intraseasonal variability in Northern Hemisphere available potential energy. *29th Conference on Hurricanes and Tropical Meteorology*, Tuscon, AZ, Amer. Meteor. Soc.

Covey, C. D. D. Lucas, J. Tannahill, X. Garaizar and R. Klein, 2013: Efficient screening of climate model sensitivity to a large number of perturbed input parameters. *Journal of Advances in Modeling Earth Systems*, **5(3),** 598-610.

Cukier, R. I., C. M. Fortuin, K. E. Shuler, A. G. Petschek, J. H. Schaibly, 1973: Study of the sensitivity of coupled reaction systems to uncertainties in rate coefficients, I. Theory. *J Chem Phys*, **59(8):**3873–8.

Cukier, R. I., H. B. Levine, K. E. Shuler, 1978: Nonlinear sensitivity analysis of multiparameter model systems. *J Comput Phys*, **26(1)**: 1–42.

Davis, C. A., and D. A. Ahijevych, 2012: Mesoscale structural evolution of three tropical weather systems observed during PREDICT. *J. Atmos. Sci.*, **69**, 1284-1305.

DeMaria, M., 1996: The effect of vertical shear on tropical cyclone intensity change. *J. Atmos. Sci.*, **53,** 2076-2087.

DeMaria, M., J. A. Knaff, and B. H. Connell, 2001: A tropical cyclone genesis parameter for the tropical Atlantic. *Wea. Forecasting*, **16,** 219-233.

Draper, N. R., and Lin DKJ. Response surface designs. Handbook of statistics, vol. 13. New York: Elsevier; 1996. pp. 343–75.

Dunion, J. P., and C. S. Velden, 2004: The impact of the Saharan Air Layer on Atlantic Tropical Cyclone Activity. *Bull. Amer. Meteor. Soc.*, **85**, 353-365.

Eberhard, P., and C. Bischof, 1999: Automatic differentiation of numerical integration algorithms. *Math Comput*, **68(226)**:717–31.

Elsner, J. B., J. C. Trepanier, S. E. Strazzo and T. H. Jagger, 2012: Sensitivity of limiting hurricane intensity to ocean warmth. *Geophys. Res. Lett.,* **39,** L17702.

Emanuel, K. A., 1986: An air-sea interaction theory for tropical cyclones. Part I: steady-state maintenance. *J. Atmos. Sci.*, **43**, 585–605.

Emanuel, K. A., 1987: The dependence of hurricane intensity on climate. *Nature,* **326,** 483-485.

Emanuel, K. A., 1988: The maximum intensity of hurricanes. *J. Atmos. Sci.*, **45,** 1143-1155.

Emanuel, K. A., 2000: A statistical analysis of tropical cyclone intensity. *Mon. Wea. Rev.,* **128,** 1139-1152.

Emanuel, K. A., 2001: Contribution of tropical cyclones to meridional heat transport by the oceans. *J. Geophys. Res.,* **106**, 14,771–14,781.

Emanuel, K.A., 2003: Divine Wind: the History and Science of Hurricanes, Oxford University Press, ISBN: 978-0195149418, pp. 592.

Emanuel, K. A., and D. S. Nolan, 2004: 26th Conference on Hurricanes and Tropical Meteorology, *Am. Meteorol. Soc.*; 2004. Tropical cyclone activity and global climate; pp. 240–241.

Emanuel, K. A., C. DesAutels, C. Holloway and R. Korty, 2004: Environmental control of tropical intensity. *J. Atmos. Sci.* **61**, 843-858.

Emanuel, K. A., 2007: Environmental factors affecting tropical cyclone power dissipation. *J. Climate,* **20**: 5297-5509.

Emanuel, K., R. Sundararajan, and J. Williams, 2008: Hurricanes and global warming: results from downscaling IPCC AR4 simulations. *Bull. Amer. Meteor. Soc.*, **89,** 347–367.

Evans, J. L., 1993: Sensitivity of tropical cyclone intensity to sea surface temperature. *J. Climate*, **6,** 1133-1140.

Flatau, M., W. H. Schubert and D. E. Stevens, 1994: The role of baroclinic processes in tropical cyclone motion. Part I: The influence of vertical tilt. *J. Atmos. Sci.,* **51,** 2589-2601.

Fovell, R. G., K. L. Corbosiero, and H.-C. Kuo, 2009: Cloud microphysics impact on hurricane track as revealed in idealized experiments. *J. Atmos. Sci.,* **66**, 1764–1778.

Frank, W.M., and E.A. Ritchie, 1999: Effects of environmental flow upon tropical cyclone structure. *Mon. Wea. Rev.,* **127,** 2044-2061.

Frank, W.M., and E.A. Ritchie, 2001: Effects of vertical wind shear on the intensity and Structure of numerically simulated hurricanes. *Mon. Wea. Rev.,* **129,** 2249-2269.

Franklin, J. L., S. J. Lord, S. E. Feuer, and F. D. Marks Jr., 1993: The kinematic structure of Hurricane Gloria (1985) determined from nested analyses of dropwindsonde and Doppler Radar data. *Mon. Wea. Rev.,* **121**, 2433-2451.

Friedman, J. H, 1991. Multivariate Adaptive Regression Splines (with discussion). *Annals of Statistics,* **19,** 1.

Ge, X.Y., T. Li, and M. Peng, 2013: Effects of vertical shears and midlevel dry air on tropical cyclone developments. *J. Atmos. Sci.,* **70,** 3859–3875.

Gentry, M. S., and G. M. Lackmann, 2010: Sensitivity of simulated tropical cyclone structure and intensity to horizontal resolution. *Mon. Wea. Rev.,* **138,** 688–704.

Gettelman, A., X. Liu, S. J. Ghan, H. Morrison, S. Park, A. J. Conley, S. A. Klein, J. Boyle, D. L. Mitchell, and J.-L. F. Li, 2010: Global simulations of ice nucleation and ice supersaturation with an improved cloud scheme in the Community Atmosphere Model, *J. Geophys. Res.,* **115**, D18216.

Goldenberg, S. B., and L. J. Shapiro, 1996: Physical mechanisms for the association of El Nino and West African rainfall with Atlantic major hurricanes. *J. Climate,* **9,** 1169–1187.

Goldenberg, S. B., C. Landsea, A. M. Mestas-Nunez, and W. M. Gray, 2001: The recent increase in Atlantic hurricane activity. *Science,* **293,** 474-479.

Gray, W. M., 1968: Global view of the origin of tropical disturbances and storms. *Mon. Wea.*

Rev., **96**, 969-700.

Gray, W. M., 1975: Tropical cyclone genesis. Dept. of Atmospheric Sciences Paper 234, Colorado State University, Ft. Collins, CO.

Gray, W. M. 1979: Hurricanes: Their formation, structure and likely role in the tropical circulation. *Meteorology over the Tropical Oceans*, D. B. Shaw, Ed., Royal Meteorological Society,155–218.

Griewank A., 2000: Evaluating derivatives: principles and techniques of algorithmic differentiation. Philadelphia: Society for Applied and Industrial Mathematics.

Gregory, D., R. Kershaw, and P. M. Inness, 1997: Parametrization of momentum transport by convection. 2. Tests in single-column and general circulation models, *Q. J. R. Meteorol. Soc.*, **123(541),** 1153–1183.

Goswami, P., and G. N. Mohapatra, 2014: A comparative evaluation of impact of domain size and parameterization scheme on simulation of tropical cyclones in the Bay of Bengal, *J. Geophys. Res. Atmos.*, **119**, 10–22.

Gwo, J. P., L. E. Toran, M. D. Morris, G. V. Wilson, 1996: Subsurface stormflow modeling with sensitivity analysis using a Latin-Hypercube sampling technique. Ground Water, 34(5):811–8.

Haarsma, R. J., J. F. B. Mitchell, and C. A. Senior, 1992. Tropical disturbances in a GCM. *Climate Dynamics*, **8,** 247-257.

Haskin, F. E., B. D. Staple, C. Ding, 1996: Efficient uncertainty analyses using fast probability integration. *Nuclear Engng Des*, **166(2)**: 225–48.

He, F., and D. J. Posselt, 2015: Impact of Parameterized Physical Processes on Simulated Tropical Cyclone Characteristics in the Community Atmosphere Model. J. Climate, 24, 9857-9872.

He, F., D. J. Posselt, C. M. Zarzycki, and C. Jablonowski, 2015: A Balanced Tropical Cyclone Test Case for AGCMs with Background Vertical Wind Shear. Mon. Wea. Rev., 143, 1762–1781.

Helton, J. C. and F. J. Davis, 2000: Sampling-based methods for uncertainty and sensitivity analysis. SAND99-2240. Albuquerque, NM: Sandia National Laboratories.

Henderson-Sellers, A., H. Zhang, G. Berz, K. Emanuel, W. Gray, C. Landsea, G. Holland, J. Lighthill, S-L. Shieh, P. Webster, and K. McGuffie, 1998: Tropical cyclones and global climate change: A Post-IPCC assessment. *Bull. Amer. Meteor. Soc.*, **79**, 19–38.

Hill, K.A., and G. M. Lackmann, 2009: Analysis of idealized tropical cyclone simulations using the weather research and forecasting model: Sensitivity to turbulence parameterization and grid spacing. *Mon. Wea. Rev.*, **137**, 745–765.

Holland, G. J., 1983: Tropical cyclone motion: Environmental interaction plus a beta effect. *J. Atmos. Sci.*, **40,** 328-342.

Hodges, K. I., 1995: Feature tracking on a unit sphere. *Mon. Wea. Rev.*, **123**, 3458–3465.

Hossain, F., E. N. Anagnostou, and A. C. Bagtzoglou, 2006: On Latin Hypercube sampling for efficient uncertainty estimation of satellite rainfall observations in flood prediction. *Computers & Geosciences.* **32(6),** 776-792.

Hogan, T. F., and R. L. Pauley, 2007: The impact of convective momentum transport on tropical cyclone track forecasts using the Emanuel cumulus parameterization. *Mon. Wea. Rev.*, **135**, 1195–1207.

Houze, R. A., Jr., 2014: Clouds and precipitation in tropical cyclones, in *Cloud Dynamics*, 2nd edition, 287-327, Academic Press, Waltham, Massachusetts, United States.

Iman, R.L., and W.J. Conover, 1980: Small sample sensitivity analysis techniques for computer models, with application to risk assessment. *Theory and Methods*, **17**, 1749–1842.

Iman, R. L., and M. J. Shortencarrier, 1984: A Fortran 77 program and User's Guide for the Generation of Latin Hypercube Samples for Use with Computer Models. SAND83-2365, Nureg/cr-3624. Albuquerque, NM: Sandia National Laboratories.

IPCC, 2013: *Climate Change 2013: The Physical Science Basis. Contribution of Working Group I to the Fifth Assessment Report of the Intergovernmental Panel on Climate Change* [Stocker, T.F., D. Qin, G.-K. Plattner, M. Tignor, S.K. Allen, J. Boschung, A. Nauels, Y. Xia, V. Bex and P.M. Midgley (eds.)]. Cambridge University Press, Cambridge, United Kingdom and New York, NY, USA, 1535 pp.

Isukapalli, S. S., and P. G. Georgopoulos, 1999: Computational methods for the efficient sensitivity and uncertainty analysis of models for environmental and biological systems. *Technical Report CCL/EDMAS-03,* Rutgers, State University of New Jersey.

Jablonowski, C., and D. L. Williamson, 2006a: A baroclinic instabilitiy test case for atmospheric model dynamical cores. *Q. J. R. Meteorol. Soc.*, **132,** 2943–2975.

Jablonowski, C., and D. L. Williamson, 2006b: A baroclinic wave test case for dynamical cores of general circulation models: model intercomparisons, *NCAR Technical Note NCAR/TN-469+STR, 89 pp.,* Natl. Cent. for Atmos. Res, Boulder, CO.

Jablonowski, C., R. C. Oehmke, and Q. F. Stout (2009), Block-structured adaptive meshes and reduced grids for atmospheric general circulation models, *Phil. Trans. R. Soc. A*, **367**, 4497–4522.

Jackson, C. S., M. K. Sen, G. Huerta, Y. Deng and K. P. Bowman, 2008: Error reduction and convergence in climate prediction, *J. Clim.*, **21**, 6698-6709.

Jakob, C. and M. Miller, 2003: Parameterization of physical processes-clouds, in *Encyclopedia of Atmospheric Sciences*, 1692-1698, Academic Press, Waltham, Massachusetts, United States.

Jones, S. C., 1995: The evolution of vortices in vertical shear. I: Initially barotropic vortices. *Q. J. R. Met. Soc.*, **121,** 821-851.

Jung, T., S. K., Gulev, I. Rudeva, and V. Soloviov, 2006: Sensitivity of extratropical cyclone characteristics to horizontal resolution in the ECMWF model. *Q. J. R. Meteorol. Soc.*, **132:** 1839–1857.

Kennedy, M., and A. O'Hagan, 2001: Bayesian calibration of computer models (with discussion). *Journal of the Royal Statistical Society*, **B63**, 425–464.

Kim, D., A. H. Sobel, A. D. Del Genio, Y. Chen, S. J. Camargo, M.-S. Yao, M. Kelley, and L. Nazarenko, 2012: The tropical subseasonal variability simulated in the NASA GISS general circulation model. *J. Climate,* **25,** 4641-4659.

Kobayashi, C., and M. Sugi, 2004: Impact of horizontal resolution on the simulation of the Asian summer monsoon and tropical cyclones in the JMA global model. *Clim Dyn,* **23**, 165–176.

Krishnamurti, T. N. and D. Oosterhof, 1989: Prediction of the life cycle of a super typhoon with a high-resolution global model, *Bull. Amer. Meteor. Soc.*, **70,** 1218-1230.

Kwon, I.-H., and H.-B. Cheong (2010), Tropical cyclone initialization with a spherical high-order filter and an idealized three-dimensional bogus vortex, *Mon. Wea. Rev.*, **138**, 1344–1367.

LaRow, T. E., Y-K. Lim, D. W. Shin, E. P. Chassignet, and S. Cocke, 2008: Atlantic Basin Seasonal Hurricane Simulations. *J. Climate*, **21**, 3191–3206.

Lim, Y. K., S. D. Schubert, O. Reale, M.-I. Lee, A. M. Molod, and M. J. Suarez, 2015: Sensitivity of tropical cyclones to parameterized convection in the NASA GEOS-5 Model. *J. Climate*, **28**, 551–573.

Loh, W. - L., 1996: On Latin Hypercube sampling. *Annals of Statistics* **24(5)**, 2058–2080.

Lord, S. J., W. C. Chao, and A. Arakawa, 1982: Interaction of a cumulus cloud ensemble with the large-scale environment. Part 4: The discrete model, *J. Atmos. Sci., 39(1),* 104–113.

Lord, S. J., H. E. Willoughby, and J. M. Piotrowicz, 1984: Role of a parameterized ice-phase microphysics in an axisymmetric, nonhydrostatic tropical cyclone model. *J. Atmos. Sci.*, **41**, 2836–2848.

Ma, J. Z., and E. Ackerman, 1993: Parameter sensitivity of a model of viral epidemics simulated with Monte Carlo techniques. II. Durations and peaks. *Int J Biomed Comput*, **32(3–4):**255–68.

Ma, J. Z., E. Ackerman, and J.-J. Yang, 1993: Parameter sensitivity of a model of viral epidemics simulated with Monte Carlo techniques. I. Illness attack rates. *Int J Biomed Comput*, **32(3–4):**237–53.

Manganello, J. V., Kevin I. Hodges, J. L. Kinter III, B. A. Cash, L. Marx, T. Jung, D. Achuthavarier, J. M. Adams, E. L. Altshuler, B.H. Huang, E. K. Jin, C. Stan, P. Towers, and N. Wedi, 2012: Tropical cyclone climatology in a 10-km global atmospheric GCM: toward weather-resolving climate modeling. *J. Climate*, **25,** 3867–3893.

Manabe, S., J. L. Holloway, and H. M. Stone, 1970: Tropical circulation in a time-integration of a global model of the atmosphere. *J. Atmos. Sci.*, **27,** 580-613.

Marks, F. D. Jr., 1985: Evolution of the structure of precipitation in Hurricane Allen (1980). *Mon. Wea. Rev.*, **113,** 909-930.

McFarquhar, G. M. and R. A. Black, 2004: Observations of particle size and phase in tropical cyclones: implications for mesoscale modeling of microphysical processes. *J. Atmos. Sci.*, **61,** 422–439.

McKay, M. D., R. J. Beckman, W. J. Conover, 1979: A comparison of three methods for selecting values of input variables in the analysis of output from a computer code. *Technometrics* **21(2)**, 239–245.

McTaggart-Cowan, R., T. J. Galarneau Jr., L. F. Bosart, R.W.Moore, and O. Martius, 2013: A global climatology of baraclinically influenced tropical cyclogenesis. *Mon. Wea. Rev.,* **141,** 1963-1989.

McTaggart-Cowan, R., E. L. Davies, J. G. Fairman Jr., T. J. Galarneau Jr., and D. M. Schultz, 2015: Revisiting the 26.5°C sea surface temperature threshold for tropical cyclone development. *Bull. Amer. Meteor. Soc.*, **96**, 1929–1943.

McCaul, E. W., 1991: Buoyancy and shear characteristics of hurricane-tornado environments. *Mon. Wea. Rev.* **119**: 1954-1978.

Mei, W., S. Xie, and M. Zhao, 2014: Variability of tropical cyclone track density in the North Atlantic: Observations and high-resolution simulations. *J. Climate,* **27**, 4797–4814.

Mendelsohn, R., K. Emanuel, S. Chonabayashi, and L. Bakkensen, 2012: The impact of climate change on global tropical cyclone damage. *Nature Climate Change,* **2 (3),** 205-209.

Merrill, R. T., 1987: An experiment in the statistical prediction of tropical cyclone intensity change. Proc. 17th Conf. on Hurricanes, Miami, Amer. Meteor. Soc., 302-307.

Miller, B. I., 1958: On the maximum intensity of hurricanes. *J.Meteor.,* **15,** 184-195.

Murphy, J. M., D. M. H. Sexton, D. N. Barnett, G. S. Jones, M. J. Webb, M. Collins, and D. A.

Murakami, H., M. Sugi, and A. Kitoh, 2013: Future changes in tropical cyclone activity in the North Indian Ocean projected by high resolution MRI-AGCMs, *Climate Dynamics,* **40**, 1949-1968.

Morrison, H. and A. Gettelman, 2008: A new two-moment bulk stratiform cloud microphysics scheme in the Community Atmosphere Model, Version 3 (CAM3). Part I: Description and Numerical Tests. *J. Climate,* **21**, 3642–3659.

Murakami, H., P.-C. Hsu, O. Arakawa, and T. Li, 2014: Influence of model biases on projected future changes in tropical cyclone frequency of occurrence. *J. Climate*, **27**, 2159-2181.

Murakami, H., and B. Wang, 2010: Future change of north Atlantic tropical cyclone tracks: projection by a 20-km-mesh global atmospheric model. *J. Climate*, **23**, 2699–2721.

Murakami, H., B. Wang, and A. Kitoh, 2011: Future change of western North Pacific typhoons: Projections by a 20-km-mesh global atmospheric model. *J. Climate*, **24**, 1154–1169.

Murakami, H., R. Mizuta, and E. Shindo, 2012: Future changes in tropical cyclone activity project by multi-physics and multi-SST ensemble experiments using 60-km-mesh MRI-AGCM. *Clim. Dyn.*, **39,** 2569-2584.

Murakami, H., Y. Wang, H. Yoshimura, R. Mizuta, M. Sugi, E. Shindo, Y. Adachi, S. Yukimoto, M. Hosaka, S. Kusunoki, T. Ose, and A. Kitoh, 2012: Future changes in tropical cyclone activity projected by the new high-resolution MRI-AGCM. *J. Climate*, **25**, 3237-3260.

Neale, R. B., et al., 2010: Description of the NCAR Community Atmosphere Model (CAM 5.0), *NCAR Technical Note, NCAR/TN-486+ STR*, NCAR, Boulder, CO.

Nolan, D. S., 2007: What is the trigger for tropical cyclogenesis? *Aust. Meteor. Mag.*, **56**, 241-266

Nolan, D. S., E. D. Rappin, and K. A. Emanuel 2007: Tropical cyclogenesis sensitivity to environmental parameters in radiative-convective equilibrium, *Q. J. R. Meteorol.Soc.*,**133,** 2085-2107.

Nolan, D. S., and E. D. Rappin 2008: Increased sensitivity of tropical cyclogenesis to wind shear in higher SST environments. *Geophys. Res. Lett.*, 35, L14805.

Nolan, D. S., J. A. Zhang, and D. P. Stern 2009: Evaluation of planetary boundary layer parameterizations in tropical cyclones by comparison of in situ observations and high-resolution simulations of Hurricane Isabel (2003). Part I: Initialization, maximum winds, and the outer-core boundary layer, *Mon. Wea. Rev.*, **137**, 3651–3674.

Nolan, D. S., and M. G. McGauley, 2012: Tropical cyclogenesis in wind shear: Climatological relationships and physical process. *Cyclones: Formation, Triggers, and Control*, K. Oouchi and H. Fudeyasu, Eds., Nova Science Publishers.

Oouchi, K., J. Yoshimura, H. Yoshimura, R. Mizuta, S. Kusunoki, and A. Noda, 2006: Tropical cyclone climatology in a global-warming climate as simulated in a 20-km-mesh global atmospheric model: frequency and intensity analysis, *J. Meteor. Soc. Japan*, **84**, 259–276.

Posselt, D. J., and T. Vukicevic, 2010: Robust characterization of model physics uncertainty for simulations of deep moist convection. *Mon. Wea. Rev.*, **138**, 1513–1535.

Posselt, D. J., and C. H. Bishop, 2012: Nonlinear parameter estimation: Comparison of an Ensemble Kalman Smoother with a Markov chain Monte Carlo algorithm. *Mon. Wea. Rev.*, **140**, 1957-1974.

Posselt, D. J., 2016: A bayesian examination of deep convective squall line sensitivity to changes in cloud microphysical parameters. *J. Atmos. Sci.*, **73**, 637-665.

Posselt, D. J., B. Fryxell, A. Molod, and B. Williams, 2016: Quantitative sensitivity analysis of physical parameterizations for cases of deep convection in the NASA GEOS-5 model. *J. Climate*, **29**, 455-479.

Park, S., and C. S. Bretherton, 2009: The University of Washington shallow convection and moist turbulence schemes and their impact on climate simulations with the Community Atmosphere Model, *J. Climate*, **22,** 3449–3469.

Park, S., C. S. Bretherton, and P. J. Rasch, 2014: Integrating cloud processes in the Community Atmosphere Model, Version 5. *J. Climate*, **27,** 6821–6856.

Putman, W. M., and S.-J. Lin, 2007: Finite-volume transport on various cubedsphere grids, *J. Comput. Phys.*, **227**, 55–78.

Putman, W. M., and S.-J. Lin, 2009: A finite-volume dynamical core on the cubedsphere grid, in *Numerical Modeling of Space Plasma Flows: Astronum-2008*, vol. 406, pp. 268–276, Astronomical Society of the Pacific Conference Series.

Pielke, R., Jr., J. Gratz, C. Landsea, D. Collins, M. Saunders, and R. Musulin, 2008: Normalized hurricane damage in the United States: 1900-2005, *Nat. Hazards Rev.*, **9,** 29–42.

Polvani, L. M., R. K. Scott, and S. J. Thomas, 2004: Numerically converged solutions of the global primitive equations for testing the dynamical core of atmospheric GCMs. *Mon. Wea. Rev.*, **132,** 2539–2552.

Paterson, L. A, B. N. Hanstrum, N. E. Davidson and H. C. Weber, 2005: Influence of environmental vertical wind shear on the intensity of hurricane-strength tropical cyclones in the Australian region. *Mon. Wea. Rev.,* **133,** 3644-3660.

Qian, Y., et al. 2015: Parametric sensitivity analysis of precipitation at global and local scales in the Community Atmosphere Model CAM5, *J. Adv. Model. Earth Syst.,* **7,** 382–411.

Randall, D. A., et al., 2007: Climate models and their evaluation. *Climate Change 2007: The Physical Science Basis. Contribution of Working Group I to the Fourth Assessment Report of the Intergovernmental Panel on Climate Change*. S. Solomon, et al., Eds., Cambridge University Press, 589-662.

Rappaport, E. N., 2000: Loss of life in the United States associated with recent Atlantic Tropical Cyclones. *Bull.Amer.Meteor.Soc.,***81,** 2065-2073.

Raymond, D. J., and A. M. Blyth, 1986: A stochastic mixing model for non-precipitating cumulus clouds, *J. Atmos. Sci., 43*, 2708–2718.

Raymond, D. J., and A. M. Blyth, 1992: Extension of the stochastic mixing model to cumulonimbus clouds, *J. Atmos. Sci., 49*, 1968–1983.

Reasor, P. D., M. T. Montgomery, and L. D. Grasso, 2004: A new look at the problem of tropical cyclones in vertical wind shear: vortex resiliency. *J. Atmos. Sci.,* **61,** 3-22.

Reasor, P. D., R. Rogers, and S. Lorsolo, 2013: Environmental flow impacts on tropical cyclone structure diagnosed from airborne Doppler radar composites. *Mon. Wea. Rev.*, **141**, 2949–2969.

Reed, K. A., and C. Jablonowski, 2011a: An analytic vortex initialization technique for idealized tropical cyclone studies in AGCMs. *Mon. Wea. Rev.,* **139,** 689–710.

Reed, K.A., and C. Jablonowski, 2011b: Impact of physical parameterizations on idealized tropical cyclones in the Community Atmosphere Model. *Geophys. Res. Lett.,* **38,** L04805, L04805.

Reed, K. A., and C. Jablonowski, 2011c: Assessing the uncertainty of tropical cyclone simulations in NCAR's Community Atmosphere Model. *J. Adv. Model. Earth Syst.,* **3,** M08002.

Reed, K. A., and C. Jablonowski, 2012: Idealized tropical cyclone simulations of intermediate complexity: A test case for AGCMs. *J. Adv. Model. Earth Syst.,* **4,** M04001.

Riehl, H., and R. J. Shafter 1994: The recurvature of tropical storms. *J. Meteor.*, **1,** 42-54.

Riemer, M., S. Jones, and C. Davis, 2008: The impact of extratropical transition on the downstream flow: An idealized modelling study with a straight jet. *Quart. J. Roy. Meteor. Soc.*, **134**, 69–91.

Riemer, M., M. T. Montgomery, and M. E. Nicholls, 2010: A new paradigm for intensity modification of tropical cyclones: thermodynamic impact of vertical wind shear on the inflow layer. *Atmos. Chem. Phys.*, **10,** 3163–3188.

Riemer, M., and M. T. Montgomery, 2011: Simple kinematic models for the environmental interaction of tropical cyclones in vertical wind shear. *Atmos. Chem. Phys.*, **11,** 9395–9414.

Riemer, M., M. T. Montgomery, and M. E. Nicholls, 2013: Further examination of the thermodynamic modification of the inflow layer of tropical cyclones by vertical wind shear. *Atmos. Chem. Phys.*, **13,** 327–346.

Ritchie, E. A., and W. M. Frank, 2007: Interactions between simulated tropical cyclones and an environment with a variable Coriolis parameter. *Mon. Wea. Rev.*, **135,** 1889-1905.

Richter, J. H. and P. J. Rasch, 2008: Effects of convective momentum transport on the atmospheric circulation in the Community Atmosphere Model, Version 3. *J. Climate,* **21,** 1487–1499.

Rotunno, R., Y. Chen, W. Wang, C. Davis, J. Dudhia, and G. J. Holland, 2009: Large-eddy simulation of an idealized tropical cyclone. *Bull. Amer. Meteor. Soc.*, **90**, 1783-1788.

Rogers, R., P. Reasor, and S. Lorsolo, 2013: Airborne Doppler observations of the inner-core structural differences between intensifying and steady-state tropical cyclones. *J. Atm. Sci.*, **141**, 2949-2969.

Rotunno, R. and K. A. Emanuel, 1987: An air–sea interaction theory for tropical cyclones. Part II: evolutionary study using a nonhydrostatic axisymmetric numerical model. *J. Atmos. Sci.*, **44,** 542–561.

Sadourny, R., 1972: Conservative finite-difference approximations of the primitive equations on quasi-uniform spherical grids. *Monthly Weather Review*, **100,** 136-144.

Sanger, N. T., M. T. Montgomery, R. K. Smith, and M. M. Bell, 2014: An observational study of tropical cyclone spinup in supertyphoon Jangmi (2008) from 24 to 27 September. *Mon. Wea. Rev.*, **142,** 3–28.

Schecter, D., M. Montgomery, and P. Reasor, 2002: A theory for the vertical alignment of a quasigeostrophic vortex. *J. Atmos. Sci.*, **59,** 150–168.

Schenkel, B. and R. Hart, 2011: Potential implications of tropical cyclone passage. *Bull. Amer. Meteor. Soc.*, **91**, 1282–1283.

Shaevitz, D. A., S. J. Camargo, A. H. Sobel, Jeffrey A. Jonas, D. Kim, A. Kumar, T. E. LaRow, Y.-K. Lim, H. Murakami, K. A. Reed, M. J. Roberts, E. Scoccimarro, P. L. Vidale, H. Wang, M. F. Wehner, M. Zhao, and N. Henderson, 2014: Characteristics of tropical cyclones in high-resolution models in the present climate. *J. Adv. Model. Earth Syst.*, **6**, 1154–1172.

Shen, B.-W., R. Atlas, O.Reale, S.-J. Lin, J.-D. Chen, J.Chang, C. Henze, and J.-L. Li, 2006: Hurricane forecast with a global mesoscale-resolving model: Preliminary results with Hurricane Katrina (2005), *Geophys. Res. Lett.*, **33,** L13813.

Skamarock, W. C., et al., 2008: A description of the advanced research WRF Version 3. NCAR Tech. Note NCAR/TN-475+STR, National Center for Atmospheric Research, Boulder, Colorado. 113 pp., available from http://www.ucar.edu/library/collections/technotes/technotes.jsp.

Smith, R., W. Ulrich, and G. Sneddon, 2000: On the dynamics of hurricane-like vortices in vertical-shear flows. *Q. J. R. Met. Soc.*, **126,** 2653-2670.

Simarro, J., V. Homar, and G. Simarro, 2013: A non-hydrostatic global spectral dynamical core using a height-based vertical coordinate. *Tellus*, **65A**, 20270.

Simmons, A. J., and D. M. Burridge, 1981: An energy and angular-momentum conserving vertical finite difference scheme and hybrid vertical coordinates. *Mon. Wea. Rev.*, **109,** 758–766.

Simpson, R., and R. Riehl, 1958: Mid-tropospheric ventilation as a constraint on hurricane development and maintenance. Prepreints, *Tech. Conf. on Hurricanes,* Miami Beach, FL, Amer. Meteor. Soc., D4-1-D4-10.

Sobol' IM, 1993: Sensitivity estimates for nonlinear mathematical models. *Math Model Comput Exp*, **1(4):**407–14.

Sobel, A. and S. Camargo, 2005: Influence of western north pacific tropical cyclones on their large-scale environment. *J. Atmos. Sci.*, **62**, 3396–3407.

Stowasser M, Wang Y, and Hamilton K, 2007: Tropical cyclone changes in the western North Pacific in a global warming scenario. *J. Climate*, **20,** 2378–2396.

Stainforth, 2004: Quantification of modeling uncertainties in a large ensemble of climate change simulations. *Nature*, **430**, 768–772.

Strachan, J., P. L. Vidale, K. Hodges, M. Roberts, and M.-E. Demory, 2013: Investigating global tropical cyclone activity with a hierarchy of AGCMs: The role of model resolution. *J. Climate*, **26**, 133–152.

Stocker, T., D. Qin, and G. Platner, 2013: Climate Change 2013: the physical science basis, *Working Group I Contribution to the Fifth Assessment Report of the Intergovernmental Panel on Climate Change, Summary for Policymakers (IPCC, 2013).*

Stensrud, D. J., J.-W. Bao, and T. T. Warner, 2000: Using initial condition and model physics perturbations in short-range ensemble simulations of mesoscale convective systems. *Mon. Wea. Rev.*, **128,** 2077-2107.

Stensrud, D. J., 2007: Parameterization Schemes*: Keys to Understanding Numerical Weather Prediction Models.* Cambridge University Press, 488 pp, Cambridge, UK.

Storlie, C. B. and J. C. Helton, 2008: Multiple predictor smoothing methods for sensitivity analysis: descriptions of techniques. *Reliab. Eng. Syst. Saf.*, **93(1),** 28-54.

Sun, Y., Z. Zhong, W. Lu, and Y. Hu, 2014: Why are tropical cyclone tracks over the Western North Pacific sensitive to the cumulus parameterization scheme in regional climate modeling? A case study for Megi (2010). *Mon. Wea. Rev.*, **142,** 1240–1249.

Sundqvist, H., 1988: Parameterization of condensation and associated clouds in models for weather prediction and general circulation simulation, in *Physically-based Modeling and Simulation of Climate and Climate Change*, Vol. 1, edited by M. E. Schlesinger, pp. 433–461, Kluwer Academic, Norwell, Massachusetts, USA.

Sugi, M., H. Murakami, and J. Yoshimura, 2009: A reduction in global tropical cyclone frequency due to global warming. *SOLA*, **5,** 164–167.

Tang, B., and K. A. Emanuel, 2010: Midlevel ventilation's constraint on tropical cyclone intensity, *J. Atmos. Sci.,* **67**, 1817 – 1830.

Taylor, K. E., R. J. Stouffer, and G. A. Meehl, 2012: An overview of CMIP5 and the experiment design. *Bull. Amer. Meteor. Soc.*, **93**, 485-498.

Tomita, H., and M. Satoh (2004), A new dynamical framework of nonhydrostatic global model using the icosahedral grid, *Fluid Dyn. Res.*, **34**, 357–400.

Torn, R. D. and C. A. Davis, 2012: The influence of shallow convection on tropical cyclone track forecasts. *Mon. Wea. Rev.*, **140,** 2188–2197.

Tory, K., S. S. Chand, R. A. Dare, and J. L. McBride, 2013: An assessment of a model-, grid-, and basin-independent tropical cyclone detection scheme in selected CMIP3 global climate models. *J. Climate*, **26**, 5508–5522.

Trenberth, K.E., and J. Fasullo, 2007: Water and energy budgets of hurricanes and implications for climate change. *J. Geophys. Res.,* **112,** D23107.

Tuleya, R. E., and Y. Kurihara, 1981: A numerical study on the effects of environmental flow on tropical cyclone genesis. *Mon. Wea. Rev.*, **109,** 2487-2506.

Ueno, M., 2007: Observational analysis and numerical evaluation of the effects of vertical wind shear on the rainfall asymmetry in the typhoon inner-core region. *J. Meteor. Soc. Japan*, **85,** 115–136.

Ullrich, P. A., and C. Jablonowski, 2012: MCore: A nonhydrostatic atmospheric dynamical core utilizing high-order finite-volume methods. *J. Comput. Phys.*, **231**, 5078–5108.

van den Heever, S. C., and W. R. Cotton, 2004: The impact of hail size on simulated supercell storms. *J. Atmos. Sci.,* **61,** 1596-1609.

Walsh, K., M. Fiorino, C. Landsea, and K. McInnes, 2007: Objectively determined resolution-dependent threshold criteria for the detection of tropical cyclones in climate models and reanalyses. *J. Climate*, **20**, 2307–2314.

Walsh, K., S. Lavender, H. Murakami, E. Scoccimarro, L.-P. Caron, and M. Ghantous, 2010: The tropical intercomparison project. In: Elsner JB, Hodges RE, Malmstadt JC, Scheitlin KN (eds), Hurricanes and climate change. Springer, Berlin, pp 1–24.

Walsh, K. J. E., S. J. Camargo, G. A. Vecchi, A. S. Daloz, J. Elsner, K. Emanuel, M. Horn, Y. K. Lim, M. Roberts, C. Patricola, E. Scoccimarro, A. H. Sobel, S. Strazzo, G. Villarini, M. Wehner, Zhao, M., J. P. Kossin, T. LaRow, K. Oouchi, S. Schubert, H. Wang, J. Bacmeister, P. Chang, F. Chauvin, C. Jablonowski, A. Kumar, H. Murakami, T. Ose, K. A. Reed, R. Saravanan, Y. Yamada, C. M. Zarzycki, P. L. Vidale, J. A. Jonas and N. Henderson, 2015: Hurricanes and climate: the U.S. CLIVAR working group on hurricanes. *Bull. Amer. Meteor. Soc*.

Wang, Y., and J. Xu, 2010: Energy production, frictional dissipation, and maximum intensity of a numerically simulated tropical cyclone, *J. Atmos. Sci.,* **67**, 97-116.

Wang, Z., 2014: Role of cumulus congestus in tropical cyclone formation in a high-resolution numerical model simulation. *J. Atmos. Sci.,* **71,** 1681–1700.

Wehner, M., K. A. Reed, F.Y. Li, Prabhat, J. Bacmeister, C.-T. Chen, C. Paciorek, P. J. Gleckler, K. R. Sperber, W. D. Collins, A. Gettelman, and C. Jablonowski, 2014: The effect of horizontal resolution on simulation quality in the Community Atmospheric Model, CAM5.1. *J. Adv. Model. Earth Syst.*, **6,** 980–997.

Wingo, M. T., and D. J. Cecil, 2010: Effects of vertical wind shear on tropical cyclone precipitation. *Mon. Wea. Rev.,* **138,** 645-662.

Williamson, D. L., 1968: Integration of the barotropic vorticity equation on a spherical geodesic grid, *Tellus*, **20**, 642–653.

Wong, M. L. M., and J. C. L. Chan, 2004: Tropical cyclone intensity in vertical wind shear. *J. Atmos. Sci.,* **61,** 1859-1876.

Wu, G-X., and N-C. Lau, 1992: A GCM simulation of the relationship between tropical-storm formation and ENSO. *Mon. Wea. Rev.,* **120,** 958-977.

Wu, Y-T, 1987: Demonstration of a new, fast probability integration method for reliability analysis. *J Engng Ind, Trans ASME, Ser B,* **109(1)**:24–8.

Wu, C.-C., and K. A. Emanuel, 1993: Interaction of a baroclinic vortex with background shear: application to hurricane movement. *J. Atmos. Sci.,* **50,** 62-76.

Wu, L., and S. Braun, 2004: Effects of environmentally induced asymmetries on hurricane intensity: A numerical study. *J. Atmos. Sci.,* **61,** 3065 – 3081.

Xiang, B. Q., S.-J. Lin, M. Zhao, S. Q. Zhang, G. Vecchi, T. Li, X. N. Jiang, L. Harris, and J.-H. Chen, 2015: Beyond weather time-scale prediction for hurricane Sandy and super typhoon Haiyan in a global climate model. *Mon. Wea. Rev.*, **143**, 524–535.

Yamada, Y. and M. Satoh, 2013: Response of ice and liquid water paths of tropical cyclones to global warming simulated by a global nonhydrostatic model with explicit cloud microphysics. *J. Climate*, **26**, 9931–9945.

Yang, B. et al. (2013), Uncertainty quantification and parameter tuning in the CAM5 Zhang-McFarlane convection scheme and impact of improved convection on the global circulation and climate, *J. Geophys. Res. Atmos.*, **118,** 395–415.

Yokoi, S., Y. N. Takayabu, 2009: Multi-model projection of global warming impact on tropical cyclone genesis frequency over the western North Pacific. *J Meteor Soc Jpn,* **87**:525–538.

Yokoi, S., Y. N. Takayabu, and Chan JCL, 2009: Tropical cyclone genesis frequency over the western North Pacific simulated in medium resolution coupled general circulation models. *Clim Dyn,* **33**, 665–683.

Zadra, A., R. McTaggart-Cowan, P. A. Vaillancourt, M. Roch, S. Bélair, and A.-M. Leduc, 2014: Evaluation of tropical cyclones in the Canadian Global Modeling System: sensitivity to moist process parameterization. *Mon. Wea. Rev.*, **142,** 1197–1220.

Zarzycki, C. M., and C. Jablonowski, 2014: A multidecadal simulation of Atlantic tropical cyclones using a variable-resolution global atmospheric general circulation model. *J. Adv. Model. Earth Syst.*, **6(3),** 805–828.

Zarzycki, C. M., C. Jablonowski, and M. A. Taylor, 2014a: Using variable-resolution meshes to model tropical cyclones in the Community Atmosphere Model. *Mon. Wea. Rev.*, **142**, 1221–1239.

Zarzycki, C. M., M. N. Levy, C. Jablonowski, J. R. Overfelt, M. A.Taylor, and P. A. Ullrich, 2014b: Aquaplanet experiments using CAM's variable-resolution dynamical core. *J. Climate*, **27**, 5481–5503.

Zarzycki, C. M., and C. Jablonowski, 2015: Experimental tropical cyclone forecasts using a variable-resolution global model. *Mon. Wea. Rev*.

Zehr, R. M., 1992: Tropical cyclogenesis in the western Pacific. NOAA Tech. Rep. NESDIS 61,

181 pp.

Zehr, R. M., 2003: Environmental vertical wind shear with Hurricane Bertha (1996). *Wea. Forecasting*, **18,** 345-356.

Zeng, Z., Y. Wang, and C. C. Wu, 2007: Environmental dynamical control of tropical cyclone intensity—an observational study. *Mon Weather Rev.* **135,** 38–59.

Zeng, Z., L. Chen and Y. Wang, 2008: An observational study of environmental dynamical control of tropical cyclone intensity in the Atlantic. *Mon. Wea. Rev.*, **136,** 3307-3322.

Zeng, Z., Y. Q. Wang and L. S. Chen, 2010: A statistical analysis of vertical wind shear effect on tropical cyclone intensity change in the North Atlantic. *Geophys. Res. Lett.*, **37,** L02802.

Zhang, G. J., and N. A. McFarlane, 1995: Sensitivity of climate simulations to the parameterization of cumulus convection in the Canadian Climate Center General Circulation Model, *Atmos. Ocean*, **33(3),** 407–446.

Zhang, Y., S. Xie, C. Covey, D. D. Lucas, P. Gleckler, S. A. Klein, J. Tannahill, C. Doutriaux, and R. Klein, 2012: Regional assessment of the parameter-dependent performance of CAM4 in simulating tropical clouds, *Geophys. Res. Lett.*, **39,** L14708.

Zhang, G. J., and N. A. McFarlane, 1995: Sensitivity of climate simulations to the parameterization of cumulus convection in the Canadian Climate Centre General Circulation Model. *Atmos. Ocean*, **33,** 407–446.

Zhang, F., and D. Tao, 2013: Effects of vertical wind shear on the predictability of tropical cyclones. *J. Atmos. Sci.*, **70**, 975–983.

Zhao, M., I. M. Held, S.-J. Lin, and G. A. Vecchi, 2009: Simulations of global hurricane climatology, interannual variability, and response to global warming using a 50-km resolution GCM. *J. Climate*, **22**, 6653-6678.

Zhao, M., I. M. Held, 2010: An analysis of the effect of global warming on the intensity of Atlantic hurricanes using a GCM with statistical refinement. *J. Climate*, **23,** 6382-6393.

Zhao, M., and I. M. Held, 2012: TC-permitting GCM simulations of hurricane frequency response to sea surface temperature anomalies projected for the late-twenty-first century. *J. Climate*, **25**, 2995-3009.

Zhao, M., I. M. Held, and S.-J. Lin, 2012: Some counter-intuitive dependencies of tropical cyclone frequency on parameters in a GCM. *J. Atmos. Sci.*, **69,** 2272–2283.

Zheng, M. H., E. K. M. Chang, and B. A. Colle, 2013: Ensemble sensitivity tools for assessing extratropical cyclone intensity and track predictability. *Wea. Forecasting*, **28,** 1133–1156.